Technische Universität München
TUM School of Computation, Information and Technology

Nanoimprint Lithography: Advances and Applications

Matthias Golibrzuch

Vollständiger Abdruck der von der TUM School of Computation, Information and Technology der Technischen Universität München zur Erlangung eines

Doktors der Naturwissenschaften (Dr. rer. nat.)

genehmigten Dissertation.

Vorsitz: Prof. Dr.-Ing. Christian Jirauschek

Prüfer*innen der Dissertation:

1. Priv.-Doz. Dr.-Ing. habil. Markus Becherer
2. Priv.-Doz. Dr. techn. Gregor Koblmüller

Die Dissertation wurde am 19.04.2023 bei der Technischen Universität München eingereicht und durch die TUM School of Computation, Information and Technology am 19.09.2023 angenommen.

Abstract

Today, applications in various research fields, such as nanoelectronics, nanomagnetics, light harvesting, and water splitting, call for well-defined nanostructures. Nanoimprint lithography (NIL) enables fast, cost-efficient, and large-area fabrication of such nanostructures with high precision and resolution. However, NIL has limitations; the processes are highly dependent on the design of the used imprinting stamps and are usually limited to certain materials and geometries. These limitations make it difficult to quickly adapt the NIL process to specific requirements of applications in different research fields. In this work, we developed several new imprinting processes based on our core lift-off NIL process to increase the versatility of NIL and to serve tailored nanostructures for application in several research fields. The advances presented in this work improve the flexibility and applicability of NIL processes, and the customized samples contribute to the successful research of our partners.

We introduced the possibility of embedding imprinted metal nanostructures into an insulating passivation layer for electrochemical applications. The embedment facilitates enhanced catalytic activity at the metal-insulator interface. In addition, we developed a direct etching NIL process, which allows the direct nanopatterning of the sample surface instead of the deposition of nanostructures on top of a substrate. In this way, we can structure semiconductor materials that are not evaporable for application in nanophotonic devices. Furthermore, we developed an imprinting stamp tuning method to adjust the feature sizes of individual nanoislands without the need to purchase an expensive new imprinting stamp. The ability to stepless tune the feature sizes of our imprinting stamps allows us rapid prototyping and tailoring of the sample properties according to our experimental requirements. Finally, integrating NIL into the fabrication of on-chip devices calls for incorporating micro- and nanostructures. So, we developed a process to microstructure our nanoimprinting stamps to create nanostructure-free spaces in the relief of the stamp to provide space to integrate microstructures.

Kurzfassung

Heutzutage werden Nanostrukturen für Anwendungen in verschiedenen Forschungsbereichen wie Nanoelektronik, Nanomagnetik, Photonik und Wasserspaltung benötigt. Die Nanoimprint-Lithografie (NIL) ermöglicht die schnelle, kosteneffiziente und großflächige Herstellung solcher Nanostrukturen mit hoher Präzision und Auflösung. Der NIL sind jedoch Grenzen gesetzt: NIL Prozesse sind in hohem Maße von der Gestaltung der verwendeten Prägestempel abhängig und in der Regel auf bestimmte Materialien und Geometrien beschränkt. Diese Einschränkungen erschweren eine schnelle Anpassung des NIL-Prozesses an die spezifischen Anforderungen in verschiedenen Forschungsbereichen. In dieser Arbeit haben wir mehrere neue Prägeprozesse entwickelt, die auf unserem zentralen Lift-Off-NIL-Prozess basieren, um die Vielseitigkeit der NIL zu erhöhen. Die in dieser Arbeit vorgestellten Fortschritte verbessern die Flexibilität und Anwendbarkeit von NIL-Prozessen, und die maßgeschneiderten Proben tragen zur erfolgreichen Forschung unserer Partner bei.

Wir haben Metall-Nanostrukturen in eine Passivierungsschicht für elektrochemische Anwendungen eingebetten. Dies führt zu einer verbesserten katalytischen Aktivität an der Metall-Isolator-Grenzfläche. Darüber hinaus haben wir ein NIL-Verfahren entwickelt, das durch direktes Ätzen direkte Nanostrukturierung der Probenoberfläche ermöglicht. Auf diese Weise können wir Halbleitermaterialien, die nicht verdampfbar sind, für nanophotonische Anwendungen fabrizieren. Außerdem haben wir eine Methode zur Größenanpassung unserer Stempel entwickelt, mit welcher die Größe der Nanostrukturen stufenlos angepasst werden kann, ohne dass ein teurer neuer Prägestempel gekauft werden muss. Dies ermöglicht uns die schnelle Anpassung der Probeneigenschaften an unsere experimentellen Anforderungen. Die Integration von NIL in die Herstellung von bestehenden Bauteilen erfordert das Zusammenspiel von Mikro- und Nanostrukturen. Daher haben wir ein Verfahren zur Mikrostrukturierung unserer Nanoimprinting-Stempel entwickelt, um Platz für die Integration von Mikrostrukturen zu schaffen.

Contents

Chapter 1

Introduction

The application of nanostructures and nanostructured surfaces is becoming increasingly important in various research areas, including electronics [1], [2], magnetics [3], [4], photonics [1], [5], [6], and electrochemistry [7], [8]. But what makes nanostructures so unique? Nanostructures are structures with dimensions between a few and several hundred nanometers. Structures with such small dimensions exhibit unique physical properties compared to their bulk counterparts: Nanostructures show light-matter interactions in the visible light regime. The dimensions of nanostructures are comparable to the wavelength of visible light [9], and therefore the structures are primed for solar-driven photonic and plasmonic applications [10], [11]. Furthermore, the smaller the structure, the larger the ratio of the edge to the bulk of the material. In electrochemical and catalytic applications, the relevant physics happens at active sites of the catalytic material [12] that are typically concentrated at the undercoordinated sites like edges of structures or interfaces to adjacent materials [13]. The nanostructuring of catalytic materials can thus increase such edge effects. Additionally, miniaturizing existing devices using nanostructures increases the number of devices manufactured per area, saving resources and increasing performance per area [14].

The need for large-scale patterns of nanostructures unites all of these applications of nanostructures: The positive effect of miniaturization can only be fully exploited for devices with many individual components. The effects of light-matter interactions and edge effects of individual nanostructures are often relatively small and, therefore, difficult to measure. However, with billions of identical nanostructures on a large area, the effects of the individual islands add up to a measurable effect of the nanostructure ensemble.

In this work, we use nanoimprint lithography (NIL) to fabricate our nanos-

tructures because it allows large-area patterning, is inexpensive, and offers nanometer-scale precision and resolution [15]–[20]. In principle, a wide range of fabrication methods can be used to produce nanostructures, each with advantages and limitations. Self-assembly methods such as micellar nanolithography [21], template-assisted electrodeposition [22], or nanosphere lithography [23] can produce nanostructures. However, the geometry of the final nanostructures is predefined by the self-assembly method, which limits the versatility of their application. In industry, optical lithography is still the standard for producing nanosized components. Here, very short wavelengths in the extreme ultraviolet (EUV) regime are necessary to fabricate the nanostructures because the Abbe diffraction limit allows a minimum feature size of about $\lambda/2$, where λ is the optical wavelength of the used light. Optical lithography devices using EUV light are expensive and optimized for industrial purposes and, therefore, not applicable for research purposes. Instead, electron beam (e-beam) lithography is commonly used to fabricate nanostructures for scientific purposes. However, e-beam lithography lacks the ability of non-linear scaling of the size of the nanostructured area, which makes the nanopatterning of large areas a time-consuming and costly process.

In contrast, NIL enables the production of structures of a few nanometers with nanometer precision and allows inexpensive and fast nanopatterning over large areas from several square centimeters [24] up to wafer scale [25]. Furthermore, NIL provides the ability to fabricate arbitrarily shaped nanostructures. All of which makes it favorable compared to the other nanopatterning methods for scientific applications.

Since its first application almost 30 years ago [15], [26], nanoimprint lithography (NIL) has proved vital as a nanopatterning technique in research[19], [20]. Nanoimprinted structures are used in several research fields, including plasmonics[27], [28], electrochemistry [29], [30], and solar cell applications [31], [32]. All NIL processes unite using an imprinting stamp with a predefined 3D relief of the nanopattern. The imprinting stamps used in this work are fabricated with e-beam lithography to guarantee high feature resolution and maximal flexibility in feature design. Despite the inexpensive high-resolution nanopatterning abilities of nanoimprinting, the strong dependence on the imprinting stamp design limited the versatility of applications in the past. As a result, the applications were often chosen according to the capabilities of the NIL method and not vice versa.

In contrast, this work aims to advance the nanoimprint techniques at our

disposal to offer fabrication processes tailored to the requirements of their intended application. The starting point for customizing the NIL techniques is a lift-off NIL (LO-NIL) process previously developed by Robin Nagel in our group [33]. Here, a double-layer lift-off process is used to fabricate metal nanoisland arrays. In the process, nanoimprinting is used to pattern the top resist while underetching the bottom resist facilitates the lift-off process.

We show four different advances in the LO-NIL process, all with different approaches. Additionally, we present an application for the samples fabricated with each new NIL process. First, we extend the LO-NIL process to enable the embedment of metal nanoislands into an insulating layer. The newly formed metal-insulator interface induces a bifunctional effect, which enhances the catalytic activity of gold nanoislands regarding hydrogen evolution. Second, we change the approach of the NIL method from a bottom-up deposition process to a top-down etching process. The changed approach enables us to structure non-evaporable materials. In that way, we fabricate a GaP metasurface with enhanced light harvesting properties in the visible spectrum. Third, we developed a method to steplessly, inexpensively, and reliably tune the features of our imprinting stamp. The new method allows the fabrication of size-tailored nanostructures to tune the plasmonic resonance wavelength of the samples according to our experimental needs. Last, we incorporated optical lithography and NIL by patterning our imprinting stamps. Combining micro- and nanopatterning allows the easy integration of nanoimprinted features into existing and new devices.

Chapter 2

An Introduction to Nanoimprint Lithography

Nanoimprint Lithography (NIL) is a low-cost, high-throughput nanopatterning technique with nanometer resolution and precision [15]–[20]. During the NIL process, the 3D relief of a predefined nanoimprinting stamp is translated into a nanopatterned structure on a sample. The patterning can be achieved via the direct transfer of thin metal films from the stamp to the sample in a nano-transfer printing (nTP) process [34] or the transfer of the stamp features into a soft polymer. The nanopatterned polymer layer can later act as a mask for etching and material deposition processes [28]. The imprinting process differs depending on the polymer used. We distinguish between ultraviolet (UV) NIL and thermal NIL [17], [18]. For UV-NIL, a UV-curable polymer is used, which is cured by UV exposure while the stamp is applied to preserve the stamp features after the stamp removal [35]. For thermal NIL, a thermos viscous polymer is used. This polymer becomes viscous over a specific glass transition temperature, at which the imprint process is performed [36]. Before the stamp is removed, the polymer is cooled to harden the polymer and preserve the imprinted features. In this work, we use thermal NIL for all our processes.

2.1 Nanoimprinting Stamps

The imprinting stamp defines the features fabricated during the imprinting process. Therefore, the design of the imprinting stamp is detrimental to the possible applications of the imprinted samples. Several methods to fabricate imprinting stamps emerged, such as e-beam lithography[16], [28], [30], inter-

ference lithography [37]–[39], optical projection lithography[31], or the use of block co-polymers [40], [41]. The imprinting stamps used in this work are fabricated by e-beam lithography because it provides the most flexibility in creating the nanopatterns. Our five stamps consist of nanopillar structures arranged in a regular cubic lattice with feature sizes ranging from 45 nm to 1400 nm.

2.1.1 The Original Silicon Nanoimprinting Stamps

In the following, we refer to those five silicon nanoimprinting stamps as the original stamps. Furthermore, we use the size of the nano features of each stamp to name the stamp. For example we refer to the original stamp with 1400 nm as the original 1400 nm stamp. The original stamps are all fabricated using e-beam lithography. The fabrication process of such nanoimprinting stamps is time-consuming and requires nanometer precision. Unfortunately, we cannot provide such precision with our e-beam lithography capabilities. Therefore, all stamps are acquired from commercial distributors, who can provide the required accuracy in their e-beam processes.

Defect-free Original imprinting stamps with nanometer precision are essential for any nanoimprinting process, as any defects of the imprinting stamps are inevitably translated into defects in the later samples. Therefore, we analyze the five original stamps concerning systematic defects and the size and height of their nanopillars using scanning electron microscopy (SEM) and atomic force microscopy (AFM) images.

Defect and Size Analysis via SEM Imaging

Figure 2.1 shows SEM images of our original nanoimprinting stamps. The first row of the figure shows an SEM image with the same magnification of each stamp to illustrate the size differences between the five stamps. The second row of SEM images shows the same number of individual nanopillars for each stamp to emphasize the regular arrangement of the nanopillar arrays. The third row shows zoomed-in images of each stamp's features to analyze the pillars' size and shape. The nanopillars of all stamps are arranged in a cubic lattice with a center-to-center distance (pitch) about double the pillar size. The nanopillar arrays of the original 1400 nm, 350 nm, and 200 nm consist of square pillars with rounded corners, while the nanopillar arrays of the

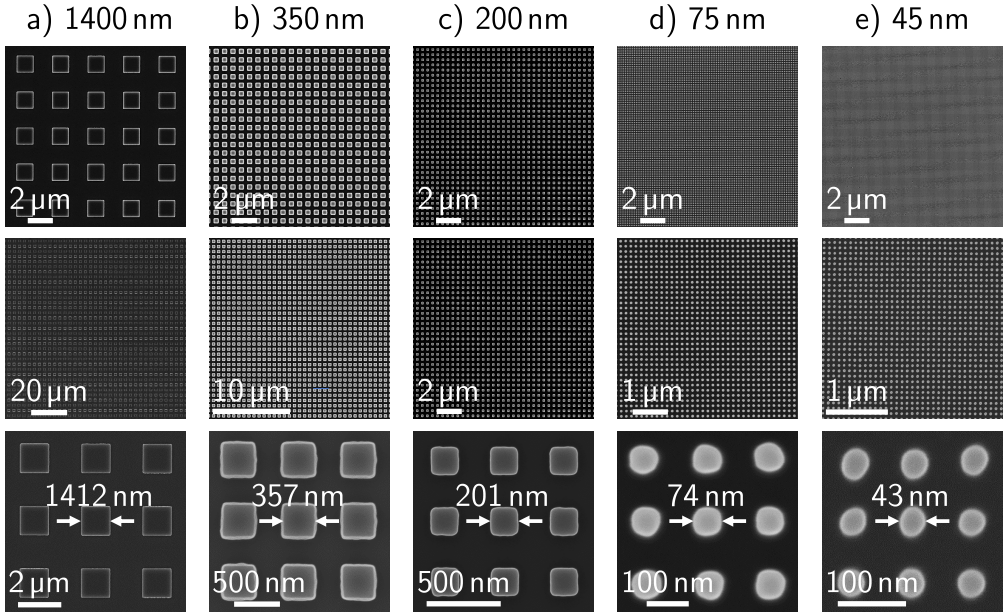

Figure 2.1: SEM images of a) the original 1400 nm stamp, b) the original 350 nm stamp, c) the original 200 nm stamp, d) the original 75 nm stamp, and e) the original 45 nm stamp. The respective top SEM image shows each stamp with the same magnification to emphasize the size difference between the stamps. The middle row shows SEM images with the same number of features for each stamp, and the bottom row shows a zoom onto the structures of each stamp. The measured side lengths/diameters of the pillars are 1412(16) nm, 357(4) nm, 201(2) nm, 74(1) nm, and 43(2) nm for the five stamps, respectively.

original 75 nm and 45 nm consist of circular pillars. For smaller feature sizes, it becomes harder to fabricate squares using e-beam lithography; therefore, we opted for circular pillars for sub-100 nm feature sizes to ensure a uniform pillar array. Figure 2.1 all nanopillar arrays of all stamps show no defects or missing pillars. Note that we encountered defects in the original stamps during this work. However, the yield of the original stamps is well above 99.9 %, and we can consider the stamps defect-free for our purposes.

Each stamp's side lengths and diameters are calculated by forming the mean value of measured side lengths or diameters for multiple nanopillars at different positions on each stamp. The standard deviation is also calculated from the individual measured values and given in parentheses behind

the measured. We measure side lengths of 1412(16) nm, 357(4) nm, and 201(2) nm for the square pillars of the original 1400 nm, 350 nm, and 200 nm stamps, respectively, and diameters of 74(1) nm and 43(2) nm for the circular pillars of the original 75 nm and 45 nm stamp, respectively. For the original 200 nm, 75 nm, and 45 nm, the measured pillar sizes are within a couple of nanometers of the nominal pillar sizes. Furthermore, the deviation of the pillar sizes is also within a couple of nanometers, which indicates a high uniformity of the imprinting stamps.

The zoom onto the nanopillars of the original 350 nm stamp shows a white frame around the nanopillars. The white frame arises from sidewalls that are not perfectly vertical, as shown in the topography measurements in the next section. However, the white frame makes it difficult to accurately measure the side length of the 350 nm nanopillars. The side length of 357(4) nm is measured without taking the white frame into account; with the white frame, the side length would increase to over 400 nm.

For the original 1400 nm stamp, the difference between the measured size and nominal size and the standard deviation of the side length is increased compared to the smaller stamps. We attribute this increase to shortcomings of the measurement method as we use a smaller magnification to evaluate the 1400 nm stamps. Here, it is not as easy to measure the side length of the nanopillars to the nanometer.

Height Analysis via AFM Imaging

Next, we analyze the height profiles of the original imprinting stamps. Therefore, we took AFM images and extracted the height profiles of each stamp. Figure 2.2 shows AFM height profiles of the original 1400 nm, 200 nm, 75 nm, and 350 nm stamps. The first three stamps in the figure have similar pillar heights at around 100 nm. We measure a height of 93 nm for the original 1400 nm and 200 nm stamp and a height of 102 nm for the original 75 nm stamp. Whereas, the original 350 nm stamp has a pillar height of 260 nm. The original 350 nm stamp was originally designed for a different application and later added to our stamp portfolio hence the height discrepancy.

Besides the pillar heights, we can extract valuable information about the shape of the sidewalls of each stamp from the AFM height profiles. The first three stamps in Figure 2.2a–c show almost vertical sidewalls, which is beneficial for a reproducible nanoimprinting process. The angled right

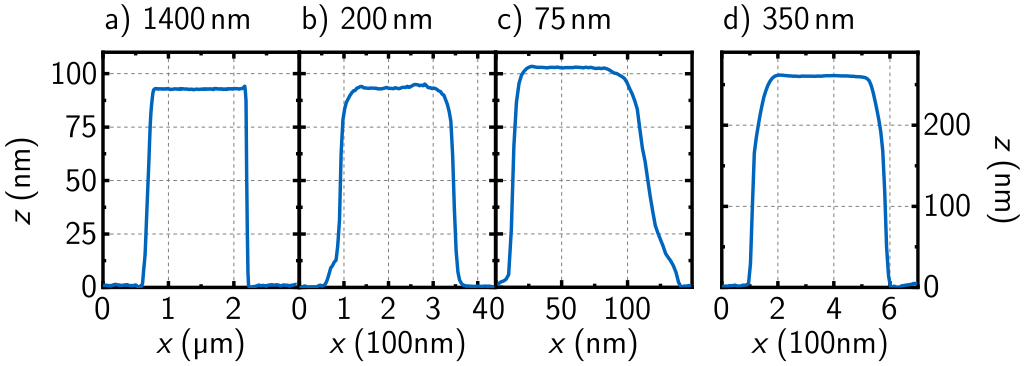

Figure 2.2: AFM height profiles of a nanopillar of a) the orignal 1400 nm stamp, b) the orignal 200 nm stamp, c) the orignal 75 nm stamp, and d) the orignal 350 nm stamp.

sidewall of the 75 nm stamp is attributed to an asymmetric AFM tip. As the AFM measures a convolution of the sample and tip, we measure an asymmetric height profile for the nanopillar with an asymmetric tip. The limitation to only measuring the convolution of the AFM tip and sample also explains the increased widths of the nanopillars compared to the SEM images because the width of the AFM tip is added to each measurement. Therefore, we use SEM images to measure the lateral dimensions of our structures and AFM to measure their topography.

In contrast to the vertical sidewalls of the first three nanopillars, the height profile in Figure 2.2d shows angled sidewalls in the top third of the 350 nm pillar. Here, the nanopillar broadens considerably, which explains the white frames in the SEM images in Figure 2.1b. We will keep the angled sidewalls in mind when analyzing the final nanoimprinted samples, as the broadening of the nanopillar can influence the final sizes of the nanoimprinted structures.

Unfortunately, we were not able to resolve an AFM height profile for the original 45 nm stamp as the AFM tip was not able to scan the small 40 nm gaps between the nanopillars of the stamp. However, as the original 45 nm stamp is from the same supplier as the original 1400 nm and 200 nm stamp, we assume the same height of 93 nm and vertical sidewalls for all three stamps.

Table 2.1 summarized the key parameters of all five original nanoimprinting stamps. The five nanoimprinting stamps are the foundation of all our

Table 2.1: Key parameters of our five original imprinting stamps

Nominal size	1400 nm	350 nm	200 nm	75 nm	45 nm
Measured size	1412 nm	357 nm	201 nm	74 nm	43 nm
Height	93 nm	260 nm	93 nm	102 nm	93 nm*
Pitch	3010 nm	700 nm	440 nm	150 nm	85 nm
Shape	square	square	square	circular	circular
Material	silicon	silicon	silicon	silicon	silicon

* Assumed value.

imprinting processes.

2.1.2 Fabrication of Semiflexible Nanoimprinting Stamps

The silicon nanoimprinting stamps introduced in the previous section could be directly used for nanoimprinting. However, the rigid nature of the silicon makes the original stamps prone to breaking during the imprinting process. As the original stamps are fabricated in an expensive e-beam process, we want to preserve the original stamps as long as possible. Therefore, we use a stamp replication process to fabricate semiflexible nanoimprinting stamps with the same features as the original stamp [34], [42]. We use a specially designed UV-curable hybrid polymer, OrmoStamp, for stamp replication and use the replicated stamps in our nanoimprinting processes afterward.

Original Stamp Preparation

Before replicating the original silicon stamps, we prepare the stamp surface for a smooth replication process. Therefore, we apply an anti-sticking layer (ASL) to the surface, which facilitates the separation between the original and the replicated stamp because the lift-off forces during replication are reduced.

To prepare the stamp for the ASL, the original stamp surface is cleaned and functionalized. First, the stamps are rinsed with acetone and isopropanol. Next, the silicon stamp is put into an O_2 plasma. The O_2 plasma removes residual organic compounds and functionalizes the silicon surface with hydroxyl groups, which enhance the bonding between the molecules of the

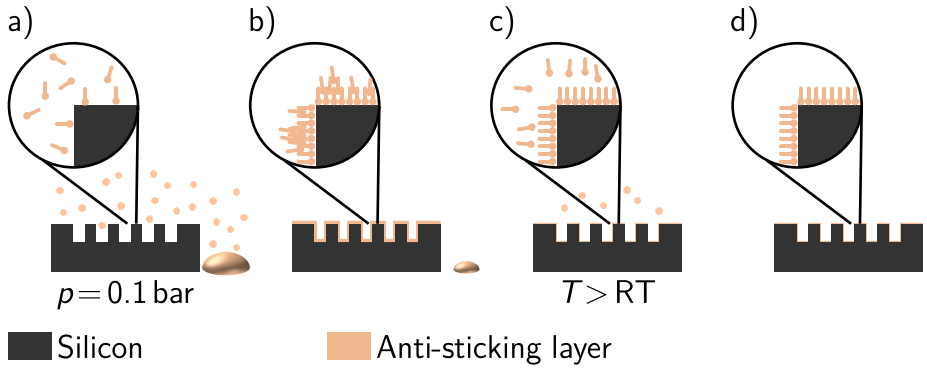

Figure 2.3: Schematic depiction of the ASL application process: a) The ASL molecules evaporate in a desiccator and cover the stamp surface. b) A monolayer of molecules chemically bonds to the stamp surface, while excessive molecules are physisorbed to the monolayer. c) The excess molecules are removed from the surface by heating the stamp. d) The stamp is covered by a monolayer of ASL molecules and ready for further use.

ASL and the silicon surface. We use Perfluorooctyltrichlorsilane (PFOTS) as ASL molecules; the silane end group bonds to the hydroxyl termination of the silicon surface, while the fluorinated tail provides Teflon-like anti-sticking properties. In addition, the silane group cannot chemically bond to the fluorinated tail, so a self-terminating monolayer of PFOTS is forming.

Figure 2.3 schematically depicts the ASL application process. First, the silicon stamp is put into a desiccator with a few drops of PFOTS. Next, the desiccator is evacuated to a pressure of around 0.1 bar for 15 min to evaporate the PFOTS as shown in Figure 2.3a. The ASL molecules fill the volume of the desiccator and eventually cover the silicon surface, where the silane groups react with the hydroxyl termination. Figure 2.3b schematically shows the silicon stamp surface covered in PFOTS after the desiccator treatment. Note, additional PFOTS molecules are physisorbed to the build-up monolayer. In a subsequent step, the stamp is heated to 130 °C for 10 min to remove excessive PFOTS molecules depicted in Figure 2.3c. Additionally, the higher stamp temperature facilitates the reaction of still-unbound PFOTS molecules to the silicon surface. Figure 2.3d shows the final ASL-coated silicon stamp, which is now ready for replication.

The Stamp Replication Process

For stamp replication, we use OrmoStamp, a UV-curable hybrid polymer designed for imprinting applications on top of a glass substrate, which enhances the stamp's durability and facilitates stamp handling. One cycle of the stamp replication process produces a stamp with inverted features. We perform the process twice to fabricate a replica of the original silicon stamps.

Figure 2.4 schematically depicts the stamp replication process. First, we prepare a glass substrate as support for the replicated stamp. The glass substrate's thickness depends on the stamp replica's use. For replicas used for further stamp replication, we use a thick glass wafer to enhance the lifetime of the replica. In contrast, we use thin semiflexible glass substrates for replicas meant for nanoimprinting. Either way, the glass substrates are cleaned in acetone and isopropanol using an ultrasonic bath to ensure a smooth replication process.
Figure 2.4a depicts the cleaned glass substrate. After the cleaning process, the surface of the glass substrate is roughened and functionalized by introducing hydroxyl groups to the surface using O_2 plasma. Figure 2.4b schematically illustrates the O_2 plasma process. The increased surface roughness and hydroxyl functionalization ensures the proper adhesion of the OrmoPrime adhesion promoter. Without preparing the surface, dewetting effects can occur during the subsequent spin coating of the OrmoPrime, and drops tend to form on the glass substrate. After the spin coating of the OrmoPrime, the substrate is baked on a hotplate to evaporate excess solvents. The final prepared glass substrate is shown in Figure 2.4c.

Next, we blow clean the prepared original stamp using a nitrogen gun. The original stamp is shown in Figure 2.4d. We apply the UV-curable polymer OrmoStamp onto the center of the original stamp, illustrated in Figure 2.4e. Next, the previously prepared glass substrate is placed onto the original stamp with the OrmoPrime side facing the original stamp as shown in Figure 2.4f. From the pressure of the glass substrate, the OrmoStamp spreads below the glass substrate. Depending on the size of the original stamp and the glass substrate, the spreading process may take a while. The amount of OrmoStamp used for the replication process is chosen so that the polymer can cover the whole original stamp, but no OrmoStamp is pressed out from under the edges of the glass substrate. Figure 2.4g shows the stamp-substrate stack after the OrmoStamp is spread evenly. Subsequently, the OrmoStamp

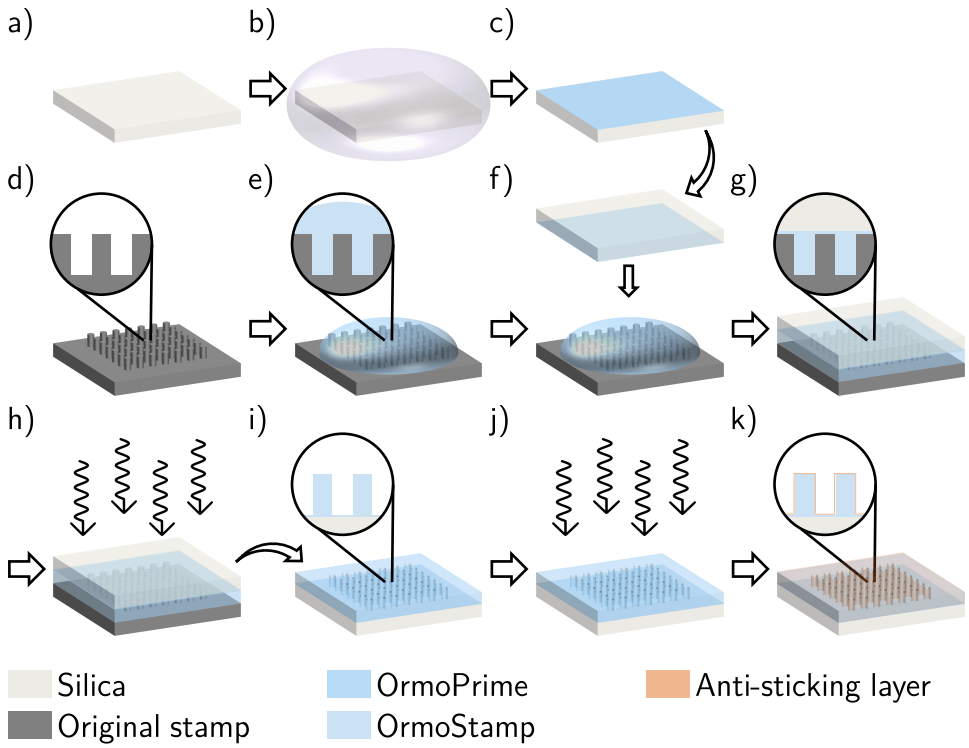

Figure 2.4: Schematic depiction of the stamp fabrication process: a) To remove unwanted contaminants, the silica substrate is cleaned using an ultrasonic bath in each acetone and isopropanol. b) After cleaning, the surface is roughened and functionalized via an O_2 plasma. c) A thin layer of OrmoPrime is spin coated onto the silica surface. d) The commercial stamp is cleaned from dust using nitrogen. e) A drop of OrmoStamp is applied to the stamp surface. f) The prepared silica substrate is placed onto the stamp with the OrmoPrime facing down onto the OrmoStamp. g) Under the weight of the silica substrate, the OrmoStamp spreads evenly between the stamp and substrate. h) Using UV exposure, the OrmoStamp film is hardened to preserve the stamp features. i) The silica substrate is removed. j) The newly formed stamp is again cured using UV exposure. k) Last, an anti-sticking layer is applied to the new stamp.

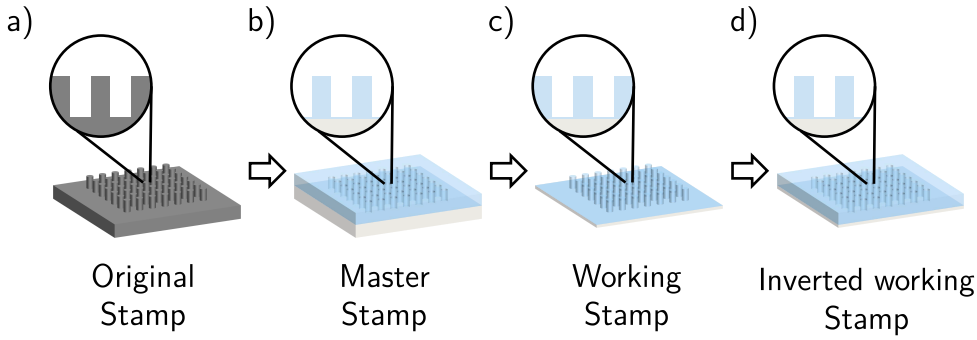

Figure 2.5: Schematic depiction of the evolution of stamps after multiple stamp fabrication cycles: a) The commercial stamp serves as the template for all stamps. b) After one cycle, the master stamp has the inverted features of the commercial stamp. c) After two cycles, the working stamp replicates the commercial stamp. d) After three cycles, the inverted working stamp has inverted features of the original and working stamp.

polymer is cured using UV light exposure from the top through the glass substrate as depicted in Figure 2.4h. The UV light hardens the OrmoStamp polymer, and the features of the original stamp are solidified onto the glass substrate.

After the UV hardening of the OrmoStamp, the glass substrate is mechanically removed from the original stamp. Here, the previously applied ASL of the original stamp ensures a smooth detachment of the glass substrate. Due to the adhesion promotion of the OrmoPrime, the hardened OrmoStamp structure sticks to the glass substrate. The polymer and the substrate form a new imprinting stamp illustrated in Figure 2.4i. To ensure a fully cured OrmoStamp, we perform an additional UV exposure of the new stamp depicted in Figure 2.4j. After the second UV exposure the stamp is annealed on a hot plate to evaporate the remaining solvent residuals from the OrmpStamp. Last, we apply an ASL to the newly fabricated imprinting stamp as explained in Section 2.1.2 to prepare the new stamp for another stamp replication process or the use in a nanoimprinting process.

We call the first inverted replica of the original silicon stamp master stamp. By repeating the replication process, we fabricate non-inverted replicas of the original stamp from the master stamp, called working stamps. The working stamps are then used for the nanoimprinting processes. Furthermore, a

working stamp with inverted features is beneficial in some nanoimprinting processes. We fabricate such inverted working stamps by cycling through the stamp replication process for a third time. Figure 2.5 shows the evolution of imprinting stamps through three replication cycles from the original silicon stamp to the inverted imprinting stamp.

Evaluation of the Stamp Replication Process

In this section, we evaluate the stamp replication process's reliability and precision regarding preserving the sizes and shapes of the original stamp's features. Therefore, we took SEM images of the working stamps to evaluate the replication process; the process parameters are listed in Appendix A.4. The OrmoStamp polymer is not conductive, which hinders direct imaging of the structures. Therefore, we deposit a few nanometers of gold onto the working stamps, which enables the imaging of the stamp in the SEM.

Figure 2.6 shows SEM images of working stamps with our five different feature sizes. The first row of the figure shows an SEM image with the same magnification of each working stamp to illustrate the size differences between the five stamps. The second row of SEM images shows the identical number of individual nanopillars for each stamp to emphasize the regular arrangement of the arrays and show possible defects in the arrays. The SEM images of the first three working stamps in Figure 2.6a–c show no defects in the arrays.

For the 75 nm working stamp, the bottom SEM image in Figure 2.6d shows three noticeable four-pillar defects indicated by the orange arrows. Four nanopillars slightly collapsed inward, forming four connected metal nanoislands on the final sample. Examples of such defects can be seen in Figure 2.10e in the next section. For the 45 nm working stamp, the top image in Figure 2.6 shows a dark rectangle in the array indicated by the blue arrow. Here, no nanopillars are present. The patch of missing nanoislands is inherited from the original silicon stamp, and we attribute the defect to a problem during the fabrication of the original stamp. However, compared to the whole nanopillar array, these defects are negligible. The SEM images of the working stamps show that the replication process reliably reproduces the feature shapes of the original stamp and introduces no defects or missing pillars to the nanopillar arrays.

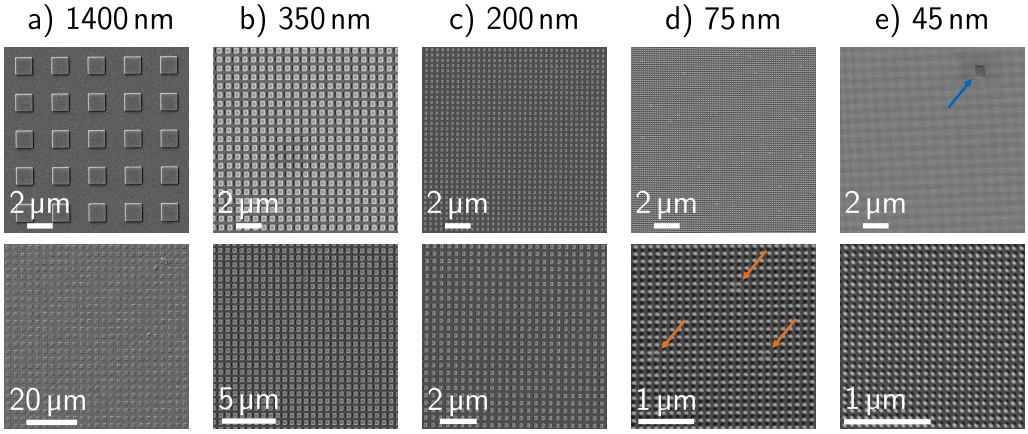

Figure 2.6: SEM images of a) a 1400 nm working stamp, b) a 350 nm working stamp, c) a 200 nm working stamp, d) a working 75 nm stamp, and e) a 45 nm working stamp. The respective top SEM image shows each stamp with the same magnification to emphasize the size difference between the stamps, while the bottom row shows SEM images with the same number of stamp features.

In addition, we took AFM images to evaluate the stamp replication process's influence on the replicated stamp's nanopillar height. Figure 2.7 shows an AFM height profile of the original 1400 nm stamp, its replica, the master stamp, and its once again replicated working stamp. The black dashed line indicates the height of the original stamp of 93 nm. The feature height of the replicas decreases with every replication process. We measure just 85 nm for the feature height of the final working stamp. The height reduction can be explained by a volume shrinkage of 4–6 % of the OrmoStamp during UV curing, according to the manufacturer [43]. Therefore, we must account for the decreased height when using the working stamps in our NIL processes and adjust the processes accordingly.

Furthermore, we measure 1426 nm, 1442 nm, and 1405 nm for the feature width of the original, master, and working stamps, respectively. In the process from the original to the master stamp, the volume shrinkage increases the hole in the master stamp. However, from the master to the working stamp, the shrinkage decreases the width of the working stamp pillar, evening out the increase in the first step. Therefore, we see no significant decrease in the side length between the original and the working stamp features because

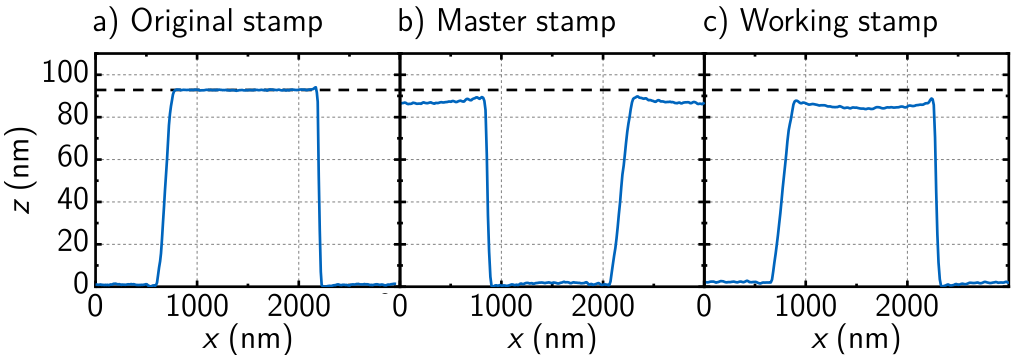

Figure 2.7: AFM height profiles of a nanopillar of a) the original 1400 nm stamp, b) its replicated 1400 nm master stamp and c) a 1400 nm working stamp replicated from the master. The black dashed line indicates the original 1400 nm stamp height.

the volume shrinkage of the first and second replication step cancel each other out.

2.2 Lift-off Nanoimprint Lithography

The foundation of all our imprinting processes is a double-resist lift-off NIL (LO-NIL) process developed by Robin Nagel in our group [33]. The process is designed to fabricate metal nanoisland arrays reproducing the features of the imprinting stamps. We use these semiflexible working stamps from the previous section to guarantee a clean imprinting result. The stamp features are transferred into the top imprint resist via thermal NIL. At the same time, the process utilizes a bottom lift-off resist layer to create an artificial undercut facilitating the metal lift-off process.

2.2.1 The Lift-off Nanoimprinting Process

This section introduces the detailed LO-NIL process for producing a gold nanoisland array on top of a silicon substrate, schematically depicted in Figure 2.8. Figure 2.8a illustrates the silicon substrate, where the grey structures indicate dirt on top of the substrate, like dust, resist residuals, or other organic compounds. The substrate is cleaned at the beginning to ensure a

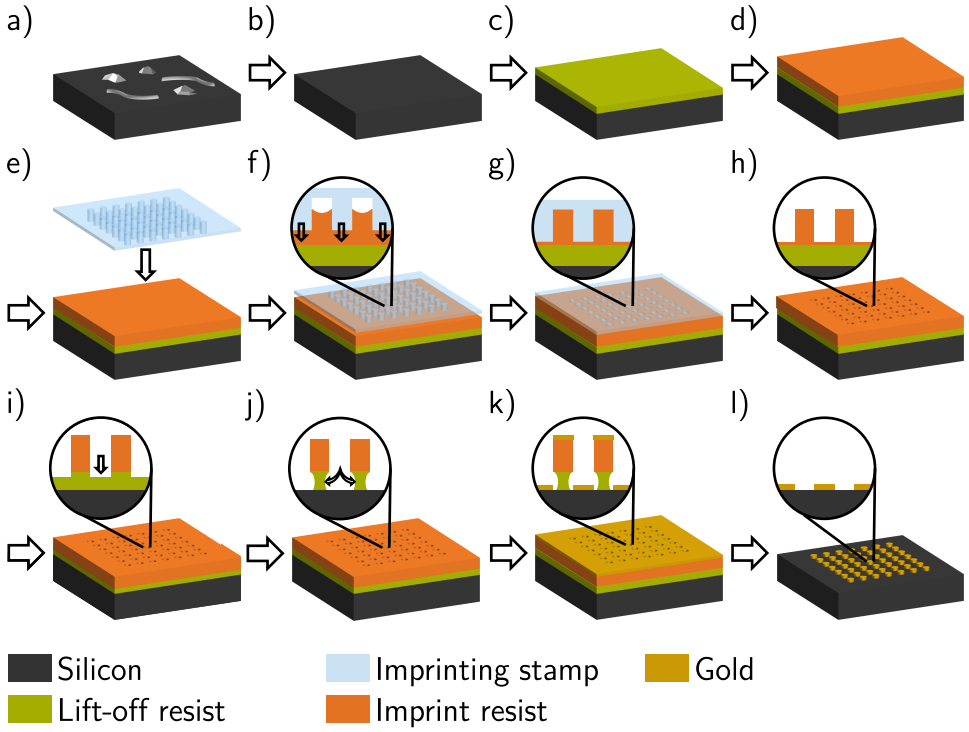

Figure 2.8: Schematic depiction of the double resist LO-NIL process of gold nanoislands on a silicon substrate: a) Out of the shelf, there are still unwanted contaminants on the silicon surface. b) The silicon substrate is cleaned in each DMSO, Acentone, and isopropanol using an ultrasonic bath. c) The lift-off resist (green) is spin coated onto the silicon surface. d) The imprinting resist (orange) is spin coated onto the lift-off resist. e) After the spin coating, the imprinting stamp is applied to the sample. f) During the imprinting process, the sample is heated above the imprinting resists glass transition temperature, and the imprinting stamp is pressed into the imprinting resist. g) When the stamp cavities are filled, the imprinting resist is cooled down again. h) The stamp is removed, and the features of the imprinting stamp are transferred into the imprint resist. The inset shows the inevitable residual layer of the imprint resist. i) The residual layer is removed via an anisotropic dry etching step, which also etches into the lift-off resist. j) Afterwards, an isotropic wet etching step of the lift-off resist is performed to expose the silicon surface and to create an artificial undercut. k) Subsequently, gold is evaporated onto the sample. l) After the lift-off of both resists, the gold nanoisland array remains on the silicon surface.

smooth fabrication process. We clean the substrate subsequently in each dimethyl sulfoxide (DMSO), acetone, and isopropanol using an ultrasonic bath. When we experience difficulties with resist adhesion during the spin coating processes, we additionally apply a O_2 plasma cleaning step to the substrate to remove any residual organic compounds. Figure 2.8b shows the cleaned silicon substrate. Our LO-NIL process is a double resist procedure with a lift-off resist at the bottom and the imprinting resist on top. The two resists must not intermix during the spin coating process, which means that the two resists must be based on different solvents. In addition, the lift-off resist must be wet-chemically etchable without etching the resist simultaneously. We use PMGI SF6 from Kayaku Advanced Materials, USA, as lift-off resist and mr-I8020R from MicroResist Technology, Germany, as imprint resist. The lift-off and the imprint resist are consecutively applied to the silicon substrate via spin coating. Figure 2.8c and Figure 2.8d show the sample after spin coating the lift-off resist and the subsequent spin coating of the imprint resist, respectively.

After the spin coating, a semiflexible imprinting stamp with the desired nanoarray pattern is applied to the sample as shown in Figure 2.8e. The stamp is placed in the center of the sample and pressed on applying pressure with a tweezer. Now, the Van der Waals forces hold the stamp in place, and the stamp-sample stack can be handled together. The stamp-sample stack is transferred into a Nano Imprinter from Obducat, Sweden, where the imprinting process is carried out. First, the stack is heated above the glass transition temperature of the imprint resist. Here, the imprint resist becomes viscous, and the stamp features can be pressed into the resist. Figure 2.8f shows the sample during imprinting. The inset of the figure illustrates the stamp pressing into the imprint resist, and the stamp cavities filling with the imprint resist. After the stamp is thoroughly pressed into the imprint resist, still under pressure, the stamp-sample stack is cooled below the glass transition temperature of the imprint resist to harden the imprint resist again. Figure 2.8g depicts the sample after imprinting. Next, the stamp is mechanically removed from the sample, leaving the stamp pattern in the imprint resist. In our case, the nanopillars of the stamp created nanoholes in the resist.

The imprinting process leaves an invertible residual layer of imprint resist at the bottom of each hole shown in Figure 2.8h. We aim to keep the residual layer as small as possible, usually around 5 nm. The residual layer of the

imprint resist must be removed before we can etch the lift-off resist. We use an anisotropic reactive ion etching (RIE) process to remove the residual layer, which etches the imprint resist only in the z-direction. Hence, the residual layer is removed while the sizes and shapes of the nanoholes in the resist are preserved. Note that the RIE process also etches into the lift-off resist. Therefore, the time of the residual layer etching step can be increased to decrease the time of the subsequent development step, which can be beneficial for the fabrication of sub-100 nm structures. Figure 2.8i shows the sample after the dry etching step. Afterward, the exposed lift-off resist is wet-chemically etched using a suitable developer. The isotropic etching step introduces an artificial undercut in the lift-off resist and exposes the silicon substrate in the nanoholes. The artificial undercut ensures a smooth lift-off process after the metal evaporation. Without the artificial undercut, the evaporated metal will likely form metal bridges from the top of the resist toward the metal in the nanoholes, which hinders a proper metal lift-off. The artificial undercut is shown in the inset of Figure 2.8j.

Now, the sample is prepared for metal deposition, and the desired thickness of gold is evaporated onto the sample. The gold attaches to the silicon substrate in the nanoholes and the top of the imprinting. To promote the adhesion of gold to the silicon substrate, we evaporate a thin titanium adhesion layer before the gold layer. Figure 2.8k shows the sample after evaporation. Last, the resists and the excessive gold are removed from the sample. For this lift-off process, we use a suitable remover in a heated ultrasonic bath. Subsequently, the finished sample is cleaned in acetone and isopropanol. The final sample is depicted in Figure 2.8i, where the stamp features are reproduced into a metal pattern on the silicon substrate.

2.2.2 Evaluation of the Lift-off Nanoimprinting Process

To evaluate the LO-NIL process, we took AFM images of the sample at different stages of the nanoisland fabrication; the process parameters are listed Appendix A.5. We extracted height profiles from the AFM images plotted in Figure 2.9. In the figure's background, we provide true-to-scale schemes of the sample at the respective step in the process. The thicknesses of the resists provided in the schemes are either measured by laser ellipsometry or calculated by using experimentally determined etching rates of the respective resists. Thus, comparing the height profiles and the schemes can validate

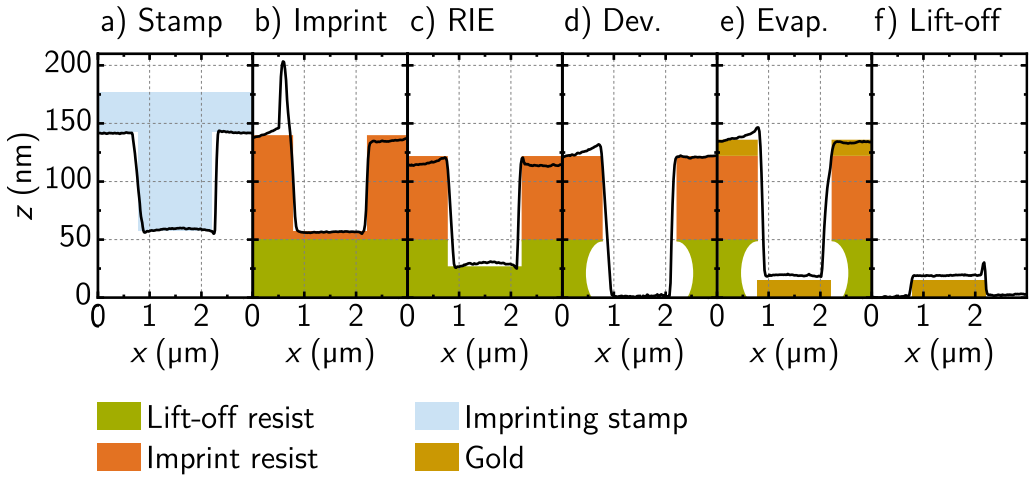

Figure 2.9: AFM height profiles of the features of a 1400 nm sample at different stages during the LO-NIL process: a) the 1400 nm working stamp, b) after imprinting, c) after the residual layer removal, d) after the development of the lift-off resist, e) after metal evaporation, and f) after lift-off. The background of each height profile depicts a true-to-scale scheme of the sample at the respective process step.

those calculations and improve our understanding of the process.

The LO-NIL process is carried out with a 1400 nm working stamp with a feature height of 85 nm as shown in Figure 2.9a. The AFM height profile matches the schematic depiction of the stamp. The lift-off and imprint layer thicknesses used for this sample are 50 nm and 70 nm, respectively. This results in a residual layer thickness of 5 nm and a hole depth of 85 nm after the imprinting process, as shown in Figure 2.9b. We attribute the spike in the height profile of the figure to imprint resist that is pushed upwards due to the mechanical forces acting during the stamp demolding process. Figure 2.9c shows the AFM height profile of the sample after the anisotropic residual layer removal. The RIE process removes the residual layer and etches almost half into the lift-off resist. The detailed process parameters for the RIE etching step can be found in Appendix A.5 among all other NIL process parameters. The artificial undercut produced by the development of the lift-off resist cannot be directly imaged by the AFM. However, the height profile in Figure 2.9d indicates the exposure of the underlying substrate

surface. The evaporation of gold shifts the AFM height profile in Figure 2.9e upwards because the gold is deposited uniformly onto the sample. Finally, the gold nanoisland remains on the substrate surface after the lift-off. We measure a gold nanoisland height of 18 nm in Figure 2.9f, which Is higher than the deposited 3 nm titanium plus 11 nm gold. The increased height is attributed to underestimating the deposition rate during evaporation. Hence, we keep in mind that the metal layers tend to be thicker than intended. The spike at the left edge of the gold nanoisland is a so-called lift-off ear, which occurs when gold grains that form on the resist sidewalls connect to the metal nanoisland [33]. Overall, the series of AFM profiles impressively demonstrates how the finely tuned individual processes of LO-NIL interact to produce an excellent result.

Precision and Resolution of the LO-NIL Process

To further analyze the capabilities of the LO-NIL process regarding precision and resolution, we took SEM images of gold nanoislands fabricated with each of our five imprinting stamps, shown in Figure 2.10. The magnifications and arrangement of the SEM images are the same as those of the five original stamps in Figure 2.1 in Section 2.1.1 to directly compare the nanoimprinted samples with the stamps. The first row of SEM images shows the same magnification for all five nanoisland sizes. The second row shows a section of each nanoisland array with the same number of metal islands, and the third row shows a zoom onto individual nanoislands of each array.

We first survey the SEM images for systematic defects like deformations of nanoislands, missing or connected nanoislands, or non-lift-off gold residuals. The nanoisland arrays of the first four samples with nanoisland sizes of 1400 nm, 350 nm, 200 nm, and 75 nm show no defects or missing nanoislands. The yield of the LO-NIL process is well above 99 % for those four feature sizes.

However, the array fabricated with the 45 nm stamp in Figure 2.10e shows a defective nanoisland array. We can distinguish three parts in the top SEM image: a dark area in the middle where the LO-NIL process produced nanoislands, an almost white part where the lift-off was not completed, and a grey area where a closed gold film covers the sample surface. The LO-NIL process using the 45 nm stamps is most delicate as the edge-to-edge distance of the individual features is only 40 nm. The small distance between the features

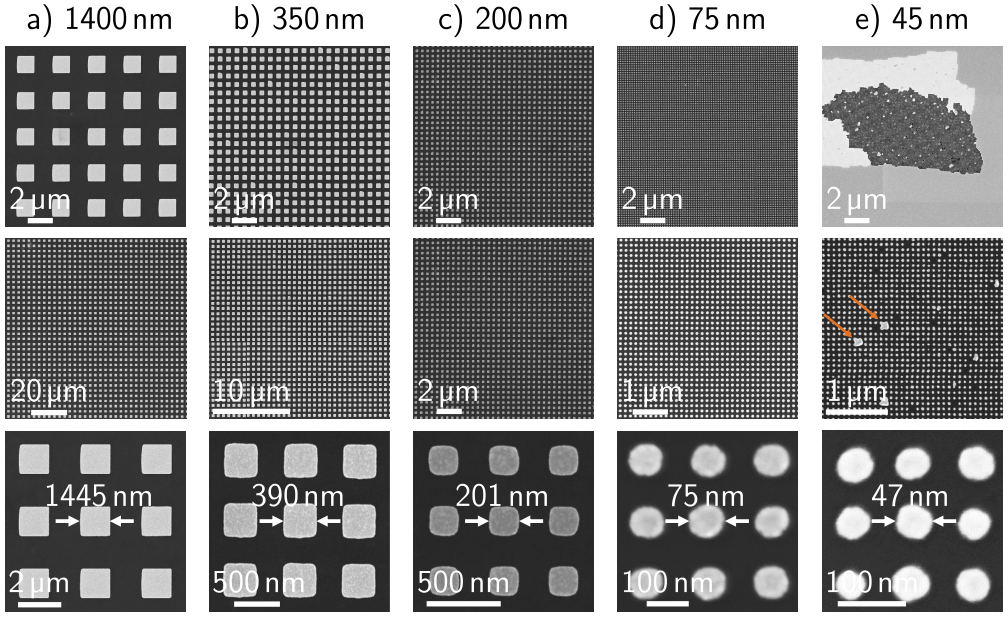

Figure 2.10: SEM images of nanoisland gold nanoislands arrays fabricated with of a) a 1400 nm stamp, b) a 350 nm stamp, c) a 200 nm stamp, d) a 75 nm stamp, and e) a 45 nm stamp. The respective top SEM image shows each nanoisland array with the same magnification to emphasize the size difference between the arrays. The middle row shows SEM images with the same number of features for each sample, and the bottom row shows a zoom onto the individual nanoislands. The measured side lengths/diameters of the gold nanoislands are 1445(12) nm, 390(7) nm, 201(2) nm, 75(1) nm, and 47(3) nm for the five stamps, respectively.

limits the development time because of the limited space for underetching. For too long development times, the developer etches through the lift-off resist, and the imprint resist is lifted off the sample, leaving the bare substrate surface. Metal evaporation leaves a gold film in areas where the resist is lift-off explaining the grey area in Figure 2.10e. We try compensating for the shorter development times by increasing the residual layer etching time. However, this can lead to difficulties during the lift-off as bridges between the gold on top of the imprint resist and the nanoislands can form during evaporation if the imprint resist layer gets too thin. The improper lift-off areas appear as a patterned gold film in the SEM, the white areas in Figure 2.10e. Both defect types are discussed in more detail in Section 2.2.3

Table 2.2: Side length/diameter comparison of stamp pillars of all five stamps and nanoislands fabricated with them using the LO-NIL process.

	Original stamp	Nanoisland array	Difference
1400 nm stamp	1412(16) nm	1445(12) nm	33 nm
350 nm stamp	357(4) nm	390(7) nm	33 nm
200 nm stamp	201(2) nm	201(2) nm	0 nm
75 nm stamp	74(1) nm	75(1) nm	1 nm
45 nm stamp	43(2) nm	47(3) nm	4 nm

on common defects during nanoimprinting. The SEM image in the second row of Figure 2.10e shows a part of the sample where the LO-NIL process produced nanoislands. However, we recognize missing islands and connected islands in the image. The connected islands marked by the orange arrows stem from collapsed working stamp pillars, as seen in Figure 2.6d in the previous section. Unfortunately, we could not fabricate a defect-free metal nanoisland array with the 45 nm stamp. We suggest using a thinner lift-off layer to shorten the overall etching times for further development toward a defect-free array. Furthermore, AFM imaging of the 45 nm working stamps could bring vital information on the height of the nanopillars of the stamp to adjust the imprint layer accordingly and further decrease the thickness of the residual layer.

Next, we analyze the precision of the LO-NIL process by comparing the shapes and feature sizes of the gold nanoisland arrays with the feature sizes of the original imprinting stamps. The shapes of the three square and two circular nanopillar arrays are all preserved in the gold nanoisland arrays. We measure side lengths of 1455(12) nm, 390(7) nm, and 201(2) nm for the 1400 nm, 350 nm, 200 nm nanoisland arrays, and diameters of 75(1) nm and 47(3) nm for the 75 nm and 45 nm nanoisland arrays, respectively. The measured sizes for the nanoislands are compared to the respective sizes of the original stamp in Table 2.2. The feature sizes of all five nanoisland arrays increased or stayed equal compared to the stamp features. We see a higher deviation between the sizes of nanoislands and the stamp features for the samples with larger features.

The side length of the 1400 nm nanoislands increased by 33 nm. In the

bottom SEM image in Figure 2.10a, we recognize a small curvature of the left edge of the nanoislands. We assume that this curvature leads to the overall increased side length measurement. When the working stamp is mechanically removed from the sample after imprinting, shear forces are applied to the stamp. Those forces can lead to a small deformation of the holes in the imprint resist. The force per nanopillar is especially high for the 1400 nm stamp, which can lead to a small curvature of one edge of the nanoislands. The deformation of the imprint resist is one of the common defects arising from the LO-NIL process and is discussed in more detail in Section 2.2.3.

The side length of the 350 nm nanoislands is significantly increased by 33 nm to 390 nm compared to the stamp features. In the bottom SEM image in Figure 2.2b, we see no deformations of the nanoislands. Therefore, deformations of the nanoislands during the LO-NIL process can be ruled out as the cause for the side length increase. The AFM height profile in Figure 2.2d showed an increase in size for the 350 nm stamp in the top third of the nanopillar. As the form of the nanopillars is directly translated into the form of the hole in the imprint resist, the size of the hole increases in the bottom third of the hole. The angled sidewalls of the hole are etched during the anisotropic residual layer etching step, and the overall size of the hole is widened. Therefore, the side length of the nanoislands increases.

The side length of the 200 nm nanoislands equals the side length of the stamp nanopillars. For the 75 nm and the 45 nm nanoislands the difference in diameter is 1 nm and 5 nm, respectively. We assume that the size difference of the 45 nm structures will be even better when the LO-NIL process is also optimized for defect-free production with the 45 nm stamps. The small differences for the smaller feature sizes make the LO-NIL method a nanostructuring method with nanometer precision, especially for structure sizes below 200 nm.

2.2.3 Common Defects of Nanoimprinted Nanoisland Arrays

The previous section shows that the LO-NIL process can reliably produce metal nanoisland arrays with nanometer precision. However, we also saw that defects can arise in the final samples if the process is not working correctly, for example, for 45 nm nanoislands. In the following, we discuss five

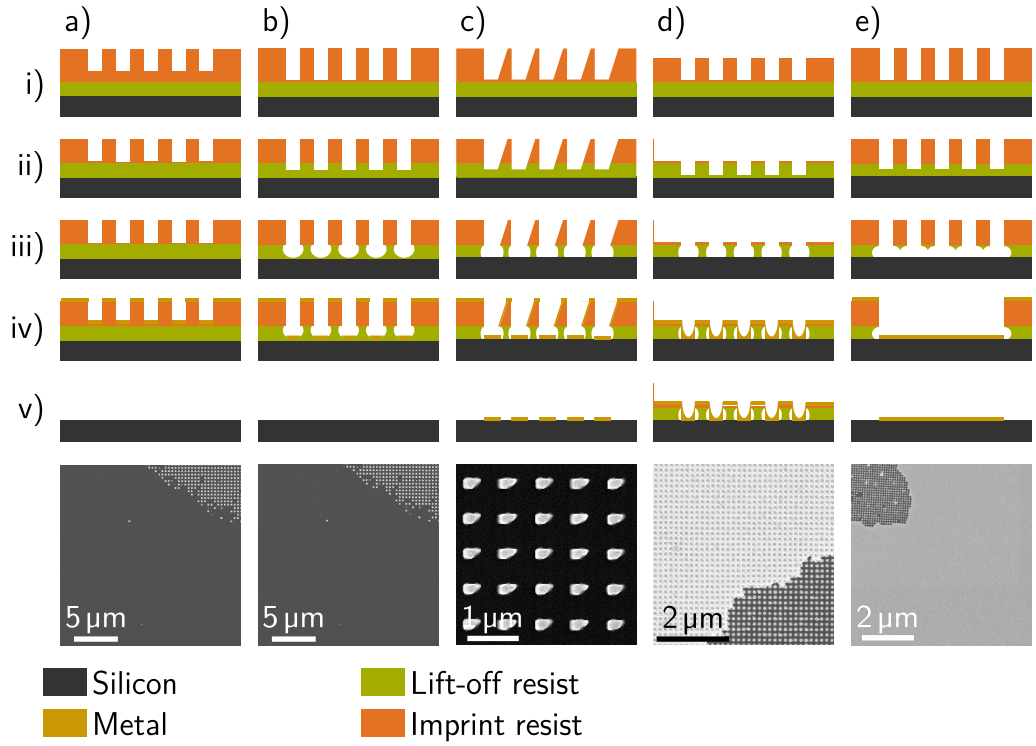

Figure 2.11: Schematic depiction of the workflow of the LO-NIL process for different common defect causes: a) no complete residual layer removal, b) no complete development, c) deformation of imprinted holes, d) too thin imprint resist, and e) too long development. For each common defect, the sample is depicted at different steps in the LO-NIL process: i) after imprinting, ii) after residual layer removal, iii) after development, iv) after metal deposition, and v) after lift-off. The SEM images under the schematic workflows show how each defect appears in the SEM.

common defect types seen in imprinted nanoisland arrays, their origin, and how to avoid them.

Figure 2.11 schematically depicts the process flow of the LO-NIL process from the residual layer removal to the final lift-off for all five defect types. In addition, an SEM image of an exemplary nanoisland array with the respective defect is shown in the bottom row of the figure. Every defect arises through a different problem at one of the steps during the process flow.

The first two defects have the same result; no metal nanoislands remain on the sample surface after lift-off. All the gold evaporated onto the sample is lifted off if the substrate surface is not exposed for evaporation during the LO-NIL process. This defect can occur in two ways: either the residual layer of the imprint resist is not entirely removed, or the lift-off resist is not fully developed to expose the substrate surface. Figure 2.11a shows the process flow for a not entirely removed residual layer. Usually, if the anisotropic RIE step did not entirely remove the residual layer, the residual layer was thicker than expected. A thicker residual layer stems from a thicker imprint resist layer or less high nanopillars of the working stamp. The left residual layer prevents the lift-off resist from being etched during the development step, and the silicon surface cannot be exposed for evaporation. Instead, the evaporated metal is deposited on the resist and completely removed with the underlying resist during lift-off. In the SEM image, the bare silicon surface is visible beside an area where the lift-off produced metal nanoislands. The nanoislands in the corner show that the defect does not necessarily arise over the whole sample.

The process flow for the same defect arising from a not fully developed lift-off resist is shown in Figure 2.11b. The residual layer is removed, but the development time is too short to etch through the lift-off resist. As a result, the evaporated metal can again not be deposited onto the substrate surface and is instead evaporated onto the lift-off resist. Again, the lift-off removes the metal with the resists, and the bare silicon surface remains. The SEM image is the same as the previous defect because the two causes for an entirely removed metal cannot be distinguished easily. Therefore, the first step to fixing the fabrication process is identifying which defect type causes the missing nanoislands. Before changing the process parameters, it is worth remeasuring the thickness of the imprint layer and the height of the working stamp features to calculate the residual layer thickness accurately. Suppose the calculated thickness of the residual layer is not larger than usual. Then, we optimize the LO-NIL process by increasing the development time because an incompletely developed lift-off resist is the more common defect type. Should an increased development time not lead to a defect-free nanoisland array, we increase the residual layer etching time to resolve the issue.

We introduced the third common defect type already during the side length measurement of the 1400 nm nanoisland array in Section 2.2.2. The side length of the nanoislands was increased due to a slight curvature of one edge

of the nanoislands caused by the shear forces during the stamp removal. Sometimes these shear forces lead to more significant deformations of the holes in the imprint resist, translated into deformations of the final metal nanoislands during the LO-NIL process. The process flow of the LO-NIL with deformed holes is depicted in Figure 2.11c. After the imprinting and stamp removal, the right side of the holes is deformed. The deformation leads to a one-sided hole widening while removing the residual layer. The rest of the process goes as usual; however, the metal nanoislands are now one-sidedly deformed. The SEM image shows metal nanoislands with a deformation on the right side. To avoid the deformation defect in the array, the working stamp must be removed as carefully as possible. If the defect arises more frequently over a considerable variation of samples, the imprint resist might be expired, which affects its mechanical stability. Then, a new imprint resist resolves the problem.

The following common defect type occurs if the imprint resist layer becomes too thin after the residual layer removal shown in Figure 2.11d. The imprint resist is thinner than usual after the imprinting process, either because the imprint resist was spined on thinner by accident or to suit a working stamp with a small nanopillar height. The residual layer removal process reduces the thickness of the imprint resist further. Bridges can then form between the metal on top of the imprint resist and the metal islands on top of the substrate in the resist's holes. These metal bridges prevent proper lift-off, leaving a film of connected nanoislands. Note that the defect can also arise if the residual layer etching time is too long, decreasing the imprint resist's overall thickness. The SEM image shows a sample where the lift-off was not working correctly. Characteristic for the defect is the visibility of the underlying nanoisland pattern in the gold layer. An accurate calculation of the maximum imprint resist thickness for a minimal residual layer can maximize the thickness of the imprint layer and mitigate the defect. If the imprint resist layer thickness is maximized, and the defect still occurs, the residual layer etching time can be reduced to preserve as much imprint resist as possible. However, the decreased etching time can increase development times as the lift-off resist is etched less during the residual layer removal.

The last common defect type arises from a lift-off of the resist layers during the development step. The process flow for the last common defect type is depicted in Figure 2.11e. If the undercut of the lift-off resist reaches the adjacent hole, the imprint resist on top loses its suspension and is lift-off.

Then, the metal deposition produces a flat gold film without the patterned resist mask. The SEM image shows a sample where most of the substrate is covered with a flat metal film; the process only worked correctly in a small part in the top right corner. The flat metal film has no visible pattern, which distinguishes the film from the gold film of the previous defect. The imprint resist tends to be lift-off in large flakes, which are visible with the naked eye during the development process, and the development time can be reduced accordingly for the subsequent samples. A shorter development time should solve the problem arising from lifted-off imprint resist.

Multiple defect types can occur on the same sample as seen in Figure 2.10 in Section 2.2.2 for the 45 nm nanoisland array. Multiple defects on the same sample usually indicate a narrow success window for the process in the parameter space. Therefore, the whole process should be reevaluated for this specific sample type, especially when the solutions to the defects in a single array are mutually exclusive. For example, suppose one sample has areas without nanoislands due to a too-short development time and some areas with a flat gold film due to a too-long development time. Resolving both issues with the current process parameters is impossible in that case.

2.3 Materials and Methods for Nanoimprint Lithography

The LO-NIL process requires all steps to be precisely coordinated to produce an optimal result. Therefore, a detailed understanding of the physics and concepts behind the individual process steps is vital for a successful fabrication of nanostructures. This section presents the fundamentals behind the utilized methods and the requirements for materials used in the LO-NIL process.

2.3.1 Substrates

The substrate is the basis of every sample because it gives the sample or device its fundamental properties and supports the nanostructures during and after fabrication. The LO-NIL method is applicable to various material systems and substrates. However, there are a few prerequisites for the substrates to guarantee a successful imprinting process. In the following, we

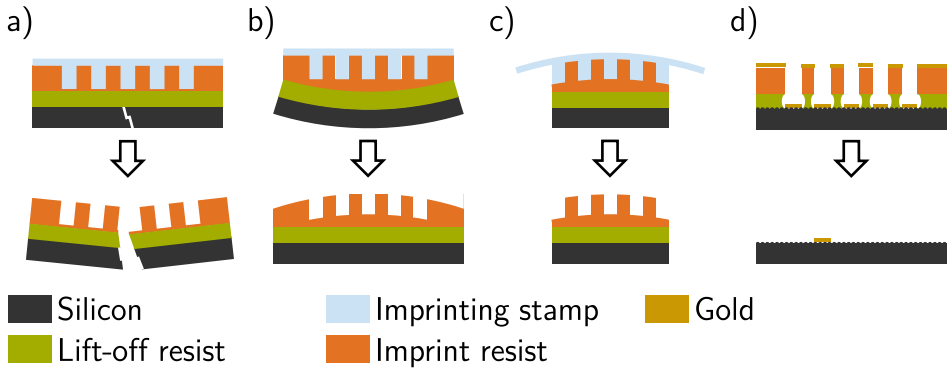

Figure 2.12: Schematic depiction of problems caused by the use of unsuitable substrates for the LO-NIL process: a) mechanical unstable substrate, b) bendable substrate, c) too small substrate, and d) substrate with too high surface roughness.

present four primary requirements for the substrates for LO-NIL: mechanical stability under pressure, no substrate bending during imprinting, sufficient substrate size, and low surface roughness. Figure 2.12 schematically shows the consequences if the substrates do not meet the respective requirement.

First, the substrate must withstand the applied pressure during the imprinting process. Otherwise, the substrate will be damaged or broken during imprinting, as depicted in Figure 2.12a. Second, a bendable substrate would lead to an uneven imprinting process as the substrate is likely to bend in the middle, and resist is accumulated in the formed hollow. This accumulation of resist leads to an increased residual layer thickness toward the middle of the sample. We experienced such behavior with free-standing silicon nitride thin films only supported at the edges. The air below the films allowed the films to bend during the imprinting process, as shown in Figure 2.12b. Third, if the substrate is significantly smaller than the stamp, the semiflexible stamp is bent over the edges of the sample as shown in Figure 2.12c. The stamp bending also leads to a thicker residual layer toward the middle of the sample and consecutively to an uneven LO-NIL process. We solved this issue by using a frame with matching thickness around the substrate to increase the bearing area of the stamp. Fourth, high surface roughness decreases the adhesion capabilities of the gold nanoislands, which leads to a poor lift-off as the metal nanoislands are not properly sticking to the surface, as shown in Figure 2.12d.

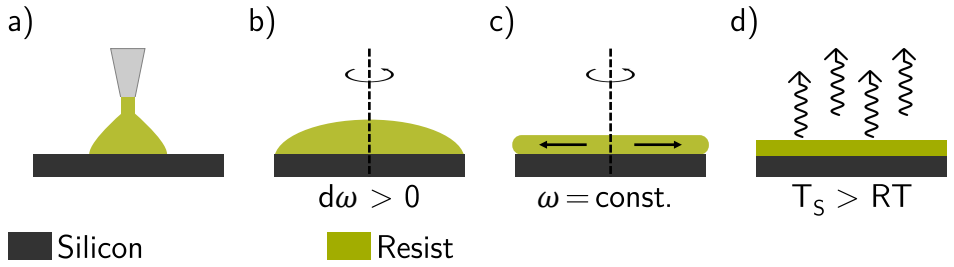

Figure 2.13: Schematic depiction of the spin coating process: a) dispersion of resist onto the substrate, b) angular acceleration of the sample, c) spinning of the sample with constant angular speed, and d) soft bake of the sample.

2.3.2 Spin Coating

Well-defined and reproducible resist thicknesses are vital for the fabrication of nanoisland arrays using LO-NIL. We use spin coating to apply resist layers with thicknesses below 100 nm to our samples. Spin coating relies on the distribution of liquids or solutions due to centrifugal forces created via substrate rotation [44]. Figure 2.13 schematically depicts the individual steps of the spin coating process.

First, the coating material is applied to the center of the substrate. We apply our resists using a syringe with a 0.25 µm RC filter to remove any larger particles to avoid defects in the final resist films. For an optimal spin coating result, we apply enough resist to cover the whole surface of our substrates. Next, the resist-covered substrate is accelerated to the desired angular rotation speed, which leads to a fast expulsion of excessive resist. The immediate expulsion stops when the viscous shear forces balance with the rotational acceleration, and the remaining resist can follow the rotation [44]. The substrate is then rotating at a constant rotational speed. The interplay between the centrifugal and fluid viscous forces now dominates the layer's thinning. In this stage, the thinning is uniform and visible due to changing interference colors [44]. At the same time, the resist solvents start to evaporate, which leads to increased resist viscosity until the resist freezes out and the final thickness is reached. Typically 90 % of the solvents evaporate during the spinning process. The sample is heated after spin coating to evaporate the residual solvents in the resist. The final sample is now ready for further processing.

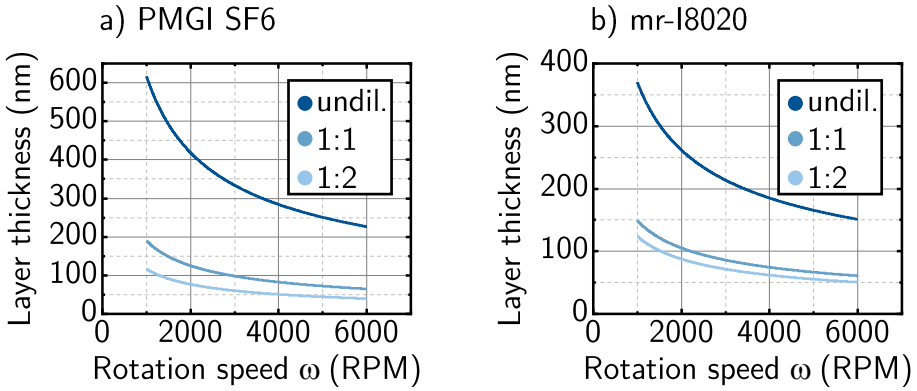

Figure 2.14: Calculated spin-coating curves for a) the lift-off resist PMGI SF6 and b) the imprint resist mr-I8020R at different dilutions. Adapted from [33]

The final resist film's thickness depends on material properties like viscosity, solvent evaporation rate, the concentration of the solvent, and the spin coating process parameters like angular acceleration and rotation speed. The final thickness h in dependence on the rotation speed ω can be described by the following simplified law [44]–[46]:

$$h = a\omega^{-b} \,, \tag{2.1}$$

with the constants a and b. The constant a summarizes all the material properties, while the constant b typically is between 0.5 and 1 for thin films [44]. Spin coaters have a maximum rotation speed ω_{max}, which limits the thinning of the resist to a minimal thickness

$$h_{\text{min}} = a\omega_{\text{max}}^{-b} \,. \tag{2.2}$$

The viscosity of the resist can be decreased by adding a suitable thinner before the spin coating process, so the final thickness of the resist can be decreased beyond h_{min}. Figure 2.14 shows spin-coating curves for our lift-off resist PMGI SF6 diluted with its suitable thinner T-thinner, and our imprint resist mr-I8020R diluted with its thinner ma-T 1050. The final thickness of each resist is plotted over ω in rotations per minute (rpm). The thickness decreases for increasing ω and dilution of the resist. We can extract the applicable ω and dilution for the desired thicknesses from the plot. However,

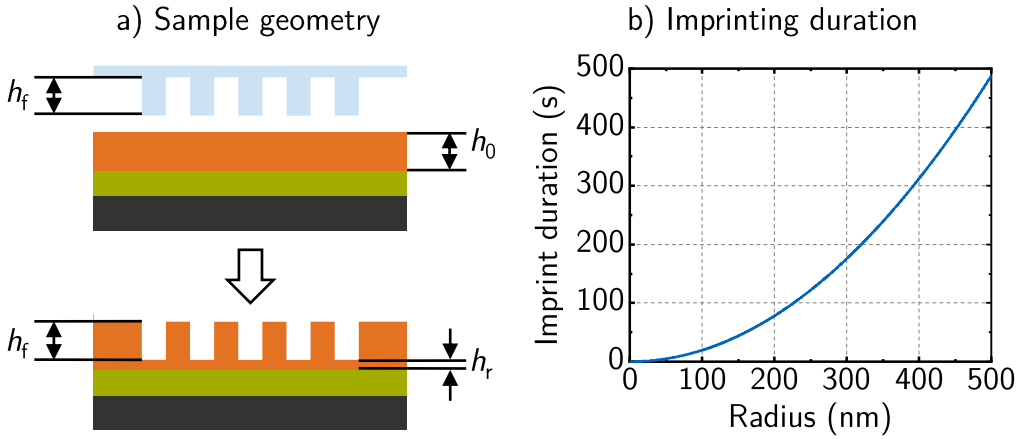

Figure 2.15: a) Schematic depiction of the geometrical parameters of the imprint stamp and imprint resist before and after the imprinting step. b) Calculated imprint duration dependent on the feature radius of features in a cubic square lattice with fill factor $\nu = 19.6\,\%$ for an assumed imprint pressure of 30 bar, resist viscosity of 1×10^5 Pa s, h_0 of 70 nm, and h_r of 5 nm.

we regularly measure the thickness of our resist using laser ellipsometry as the thicknesses can vary due to environmental parameters and changes in the composition of the resist over time.

2.3.3 Imprinting

During the imprinting process, the protruding features of the imprinting stamp are pressed into the viscous imprint resist. This imprinting process can be described as a squeezed flow of viscous material, where the vertical protruding features of the resist squeeze the underlying imprint resist [47]. The squeezing leads to a lateral resist flow into the stamp cavities until the cavities are filled. To introduce the physics behind the squeezed flow and discusses the resulting critical parameters for the imprinting process, we define the geometrical parameters of the sample before and after the imprinting process in Figure 2.15a, where h_0 marks the initial height of the imprint resist, h_f the height of the features of the stamp, and h_r the height of the residual layer after the imprinting process. Additionally, the stamp's fill factor ν describes the quotient of the area covered by features over the

Table 2.3: Feature Size, pitch, and fill factor of our five imprinting stamps

Feature Size	1400 nm	350 nm	200 nm	75 nm	45 nm
Pitch	3010 nm	700 nm	440 nm	150 nm	85 nm
Fill factor	21.6 %	25.0 %	20.7 %	19.6 %	22.0 %

total area of the stamp. For nanofeatures arranged in a cubic lattice ν can be calculated by

$$\nu = \frac{A_\mathrm{f}}{p^2} \ , \tag{2.3}$$

where A_f is the area of the stamp features, and p is the pitch of the array. Table 2.3 shows our five imprinting stamps' side lengths/diameters, pitches, and fill factors.

In the following, we assume that the imprint resist is incompressible and its total volume is preserved. Thus, the volume of the imprint resist before imprinting V_b equals the volume after V_a. From that, we can calculate h_r depending on h_0 and h_r using the stamp's fill factor ν and the patterned area A_patt using this following continuity equation:

$$V_\mathrm{b} = V_\mathrm{a} \tag{2.4}$$
$$A_\mathrm{patt} h_0 = A_\mathrm{patt} h_\mathrm{r} + (1-\nu) A_\mathrm{patt} h_\mathrm{f} \tag{2.5}$$
$$h_0 = h_\mathrm{r} + (1-\nu) h_\mathrm{f} \tag{2.6}$$
$$\Rightarrow h_\mathrm{r} = h_0 - (1-\nu) h_\mathrm{f} \ . \tag{2.7}$$

Knowing h_r is crucial for every NIL process as h_r dictates the etching time for the residual layer removal step.

The squeezed resist flow underneath the stamp features can be modeled by solving the Navier-Stokes equation for nonslip boundaries [47], [48]. Additionally, the resist is treated as an incompressible liquid with constant viscosity. For circular-shaped features, the following expression calculates the height of the resist below the stamp feature over time t [49]:

$$\frac{1}{h(t)^2} = \frac{1}{h_0^2} + \frac{4F}{3\pi\eta_0 R^4} t \tag{2.8}$$

with the imprint force F, the radius of the cylinders R, and the polymer viscosity η_0. The final thickness below the stamp feature is described by h_r. Inserting $h_\mathrm{r} = h(t_\mathrm{total})$ we can calculate the total imprinting time t_total by

$$t_\mathrm{total} = \frac{3\eta_0 R^2}{4p}\left(\frac{1}{h_\mathrm{r}^2} - \frac{1}{h_0^2}\right) , \tag{2.9}$$

where we assume a constant pressure $p = {}^{F}/_{\pi R^2}$ under each stamp feature, which relates to the imprinting pressure p_imp by $p = {}^{p_\mathrm{imp}}/_{\nu}$. Analyzing the equation, t_total increases quadratically with the radius R of the stamp features. Therefore, smaller features are imprinted faster than larger features.

We calculated the imprinting time depending on R for a cubic lattice of circular features. In our standard LO-NIL process an h_0 of 70 nm leads to an h_r of 5 nm. The imprinting pressure of 30 bar translates to 150 bar under the stamp features, and at an imprinting temperature of 165 °C, the manufacturer gives a resist viscosity of around 1×10^5 Pa s. The calculated t_total is plotted in Figure 2.15b. The imprinting durations range from under 10 s for R below 20 nm to almost 500 s for structures with an radius of 500 nm. The drastic increase in imprinting time with feature size limits the applicability of our NIL processes for micrometer-scale features.

The second implication from Equation (2.9) is that a residual layer is inevitable because the imprinting duration goes to infinity for vanishing h_r. In contrast, increasing h_r would decrease t_total, but an increased residual layer would impede a smooth LO-NIL process. We use an imprinting time of 300 s for all our NIL processes. This time guarantees a residual layer of 5 nm or less for all our feature sizes except the 1400 nm stamp while keeping the time consumption of the imprinting process reasonably short. Furthermore, a thicker residual layer for the 1400 nm stamp can be handled during the subsequent etching of the residual layer and lift-off resist because the large features allow for longer etching times.

2.3.4 Plasma Cleaning and Activation

We use O_2 plasma to clean our samples from organic residuals and activate their surface for subsequent processing. We use a Q150 plasma system from Parylene Systems GmbH, Germany, for this work. The system generates a plasma with microwave radiation at a frequency of 2.45 GHz with an adjustable power between 50–1200 W. The generated O_2 radicals and ions move

freely in the process chamber and eventually hit the sample surface, where they can undergo a chemical reaction causing chemical etching of the sample surface. The O_2 plasma removes organic contaminations from the sample surface and activates the surface via the generation of hydroxyl groups [50], [51], which facilitates the adhesion of polar resists and the bounding of the ASL molecules. The plasma power and etching time vary depending on the material and the intended use of the sample. The specific plasma treatment parameters for each process are in Appendix A.3.

2.3.5 Anisotropic Reactive Ion Etching

Reactive ion etching (RIE) is a dry etching technique that uses the plasma of one or more process gases to physically and chemically etch materials, depending on the used gases. The etching is carried out in a process chamber initially pumped to around 1×10^{-5} mbar and then flooded with the process gases. Next, the plasma is ignited in the chamber at constant pressure, and the ionized gas species are accelerated onto the sample. We used a PlasmaLab 80 plus reactive ion etcher from Oxford, UK, for this work. This RIE system has two channels to power the plasma: capacitive coupled plasma (CCP) and inductively coupled plasma (ICP).

The CCP is driven by a radio frequency (RF) voltage applied to two parallel plates at the top and bottom of the chamber. The RF voltage is driven at a frequency of 13.56 MHz, and the resulting electromagnetic field ionizes the gas species, separating the electrons from the gas atoms [52]. The much lighter electrons can follow the applied RF voltage in contrast to the heavier ions. Around the electrode plates, electrons hit the electrode and charge it negatively. The formed negative potential is called the direct current (dc) bias [52], [53]. The dc bias then leads to the acceleration of the positively charged ions toward the electrode. The bottom plate electrode of the capacitor supports the sample during the etching process. So, the gas ions are accelerated onto the sample surface. The strength of the dc bias is a measure of the velocity of the bombarding ions, which relates to the physical etching power and the directionality of the process [53]. Therefore, a higher dc bias leads to a higher anisotropy of the RIE process. The ICP is inductively ignited by a high-frequency source. The ICP power has only a minor influence on the dc bias due to the inductive nature of the plasma generation [53]. Therefore, the density of the plasma can be controlled by

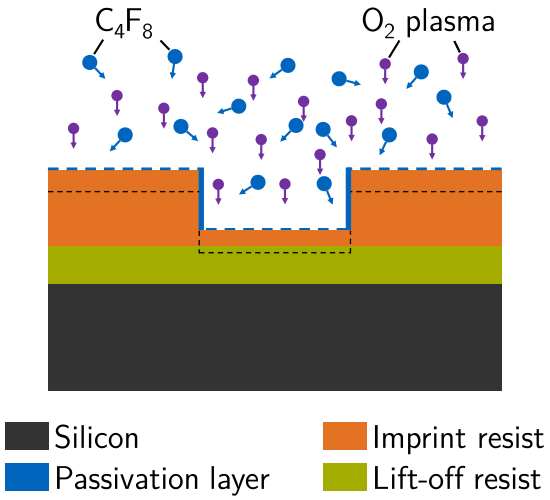

Figure 2.16: Schematic depiction of a two-gas anisotropic RIE process. The C_4F_8 gas forms a passivation layer on all surfaces, while the vertically directed O_2 plasma etches this layer and the underlying resist only on horizontal surfaces. Hence, the vertical surfaces are not etched; thus, the RIE process preserves all lateral dimensions.

the ICP power independently from the dc bias. The plasma density is a measure of the ion current hitting the sample surface. Increasing the ion current can increase the etch rate of the RIE process. The etch rate can also be increased by increasing the dc bias, but a high dc bias can damage the sample [53].

We use O_2 plasma in the RIE to remove the residual layer of the organic imprint resist. Besides the physical etching component based on the bombardment of the sample with accelerated ions, O_2 radicals chemically etch the resist surface. This chemical etching process is not dependent on the ions' velocity; therefore, scattered radicals also contribute to the reaction. Those scattered radicals can etch the sidewalls of the imprint resist holes, leading to an increased nanoisland diameter. Inspired by the Bosch process for deep silicon etching [54], we use additional C_4F_8 gas to increase the anisotropy of the etching process and avoid the widening of the imprinted structures. The C_4F_8 plasma forms long Teflon-like polymers that passivate the surface of the imprint resist. The physical directional etching can penetrate the passivation

layer and removes the residual layer, while the passivation layer impedes the chemical etching of the sidewalls.

Figure 2.16 schematically depicts the anisotropic RIE etching process of the residual layer. The blue line indicates the passivation layer formed by the C_4F_8 plasma, which can be penetrated by the directional physical etching of the O_2 plasma indicated by the dashed parts of the line. At the end of the process, we apply a short purely O_2 RIE step to remove the passivation layer from the sidewalls. The black dashed line represents the geometry of the sample after the RIE etching process. This anisotropic RIE process can be easily adapted for other material systems like the directional etching of SiO_2 [55]. In contrast, only O_2 plasma at small dc biases is used for a maximal isotropic RIE process [28]. The specific etching parameters for each process can be found in Appemdix A.5.

2.3.6 Metal Deposition

The metal films used in this thesis are all applied by electron beam physical vapor deposition (PVD). For metal evaporation, we use a Pro Line PVD 75 system from the Kurt J. Lesker Company, USA. The whole process is carried out in an evaporation chamber at ultra-high vacuum (UHV) of less than 1×10^{-7} mbar generated by a turbomolecular pump. The system uses a load lock chamber to transfer the samples into the evaporation chamber without breaching the UHV. The individual metals are evaporated using a focused electron beam generated via heating a tungsten filament. As the evaporation rate is dependent on the temperature of the material, the rate can be adjusted via the intensity of the electron beam. During evaporation, a quartz crystal (XTAL) measures the deposition rate of the metal onto the samples. The system automatically adjusts the e-beam intensity to reach the desired deposition rate. Then, the sample shutter opens and automatically closes when the desired film thickness is reached. The deposition rates for the used metals are $1.2\,\text{Å}\,\text{s}^{-1}$ for chromium and titanium, $2\,\text{Å}\,\text{s}^{-1}$ for gold, and $3\,\text{Å}\,\text{s}^{-1}$ for aluminum. The desired film thicknesses vary depending on the NIL process and the application of the nanoislands and can be found in Appendix A.7. Our NIL processes are not solely restricted to metals. The only requirement for the nanoisland material is that the material is evaporable; for example, we deposited SiO_2 on a gold surface in [30]. In some cases, sputtered materials are also applicable. However, the sputtering

process can lead to difficulties during the lift-off process because it is more likely that bridges between the material in the holes and on top of the resist form during sputtering as sputtering is a more isotropic deposition method.

2.3.7 Imaging

The SEM images in this work are all taken with a Nvision 40 FIB/SEM from Zeiss, Germany. We use an aperture of 30 µm and an extraction voltage of 5 kV. Unless otherwise stated, all SEM images are taken with the system's inlense electron detector to maximize the contrast between different materials.

The AFM images for this work are taken with a Dimension Icon AFM from Bruker, USA. We operate the AFM in ScanAsystMode using ScanAsyst-Air AFM tips. The ScanAsystMode measures a force-distance curve at every measurement point by physically "pressing" the AFM tip into the sample. This measurement mode ensures a high resolution even for small feature sizes. Later, the AFM height profiles are extracted from the measured images, tilt corrected, and leveled to their lowest point.

The optical microscope images in this work are taken with a profile-analyzing laser microscope VK-X250K from Keyence, Japan. The microscope combines classical white light imaging with laser imaging to enhance the resolution of the final images.

Chapter 3

Metal Nanoisland Arrays Embedded in an Insulator Layer

So far, we can fabricate nanoislands on top of a substrate using our LO-NIL process. However, for some experiments, it can be beneficial to embed the nanoislands into a material layer. Furthermore, having two different materials at the bottom of the nanoislands and surrounding the nanoislands can be helpful. For example, for electrochemical applications, it is desired to have the nanoislands electrically conducted to the underlying material while having the underlying material electrically passivated to the environment [30]. Therefore, we use doped silicon as the underlying substrate and SiO_2 or Si_3N_4 as the surrounding passivation material. To fabricate such embedded nanoisland electrodes, we adapt our standard LO-NIL process based on [33] by adding a dry etching step to etch through the passivation layer and expose the silicon surface for evaporation. We further refer to the new process as embedded LO-NIL.

3.1 Substrate Preparation

The embedded LO-NIL process and the electrochemical application of the samples impose additional requirements on the substrates. TheSiO_2 layer for the embedment must be applied to the top of the substrate. Therefore, we acquire thermally oxidized silicon substrates. Furthermore, an aluminum contact must be applied to the substrate's backside to guarantee proper electrical conductivity for the electrochemical setup.

The process to prepare the silicon substrate for the embedded LO-NIL is schematically depicted in Figure 3.1. The top scheme in each figure shows the

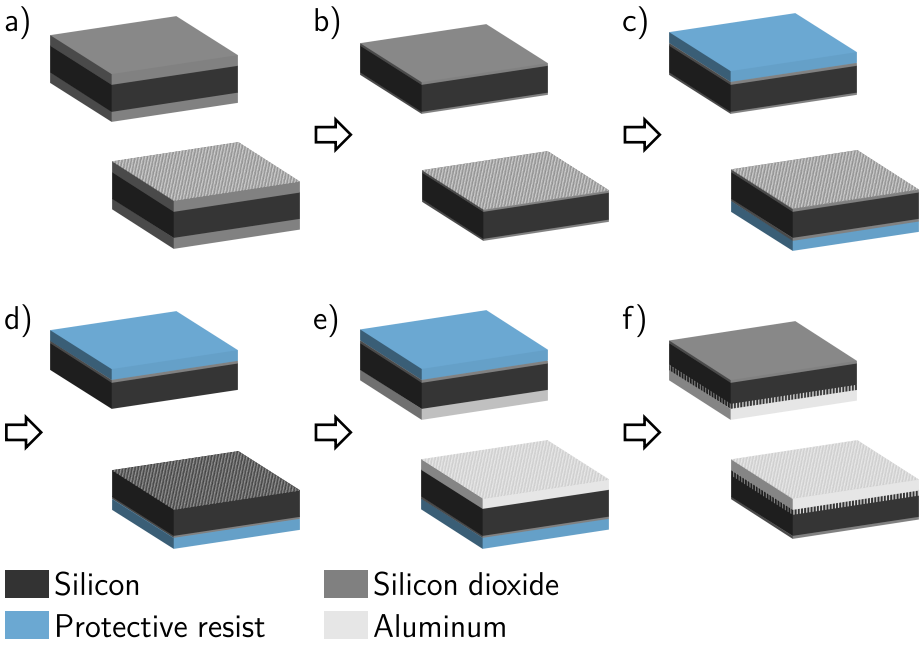

Figure 3.1: Schematic depiction of the substrate preparation process for the embedded LO-NIL process: a) The thermally oxidized silicon substrate is cleaned in each DMSO, acetone, and isopropanol using an ultrasonic bath. b) The SiO_2 layer is etched to the desired thickness using an HF solution. c) A protective resist is applied to the top of the substrate. d) The remaining SiO_2 is removed from the backside of the substrate using an HF solution. e) Within 30 minutes, aluminum is deposited onto the backside of the substrate. f) The protective resist is removed, and the substrate is annealed to ensure an ohmic back contact.

top view of the substrate, and the bottom scheme shows the back view. The backside of the substrate is not polished, indicated by the textured surface. First, the thermally oxidized silicon substrate is cleaned using an ultrasonic bath in each DMSO, acetone, and isopropanol. Figure 3.1a shows the oxidized and cleaned silicon substrate. The initial thickness of the SiO_2 layer of the substrates is typically around 50 nm. However, for the embedment of the nanoislands, we need a SiO_2 thickness of 10–15 nm. Therefore, we use a hydrofluoric acid (HF) based solution to etch the SiO_2 to the desired thickness, depicted in Figure 3.1b. Afterward, we apply a protective resist via spin coating to preserve the SiO_2 layer during the subsequent steps. The

applied resist is shown in Figure 3.1c. Any HF resistive resist or polymer can be used as a protective resist.

Next, we prepare the backside of the sample to apply the aluminum contact. Therefore, the remaining SiO_2 is removed using the HF solution again, depicted in Figure 3.1d. After the HF removal, the bare silicon surface is hydrogen terminated [56]. This hydrogen termination prevents the surface from natively oxidizing for about 30 minutes. The aluminum back contact is evaporated within this time frame to ensure a clean metal-semiconductor interface with no intermediate oxide layer, shown in Figure 3.1e. After the aluminum deposition, the substrate is annealed to increase the contact quality further. The aluminum partly diffuses into the silicon during annealing, resulting in an ohmic contact. The protective resist is removed before the annealing process; otherwise, it would be burned and stuck to the substrate surface. The final substrate with the thin SiO_2 layer on top and the aluminum back contact is shown in Figure 3.1f.

3.2 The Embedded Lift-off Nanoimprint Lithography Process

We introduce the embedded LO-NIL process exemplarily for the fabrication of gold nanoislands on a silicon substrate embedded into a SiO_2 layer. Figure 3.2 schematically depicts the fabrication process. We use silicon with a thin SiO_2 layer on top as a substrate, where nanoislands are embedded into the SiO_2 layer. First, the substrate is cleaned consecutively in each DMSO, acetone, and isopropanol using an ultrasonic bath. The clean substrate is shown in Figure 3.2a. Next, the lift-off and imprint resist are applied to the substrate via spin coating. We choose the thickness of the imprint resist to minimize the residual layer after the imprinting step. After the spin coating of the resists, we apply the imprinting stamp to the sample and transfer the stamp-sample stack into the imprinting device. Figure 3.2b shows the sample after the spin coating of the resists and before the imprinting process. The sample is heated above the imprint resist's glass transition temperature during imprinting. Above this temperature, the imprint resist becomes viscous, and the stamp can be pressed into the resist. Under pressure, the resist fills the stamp cavities, and the stamp's features are molded into the

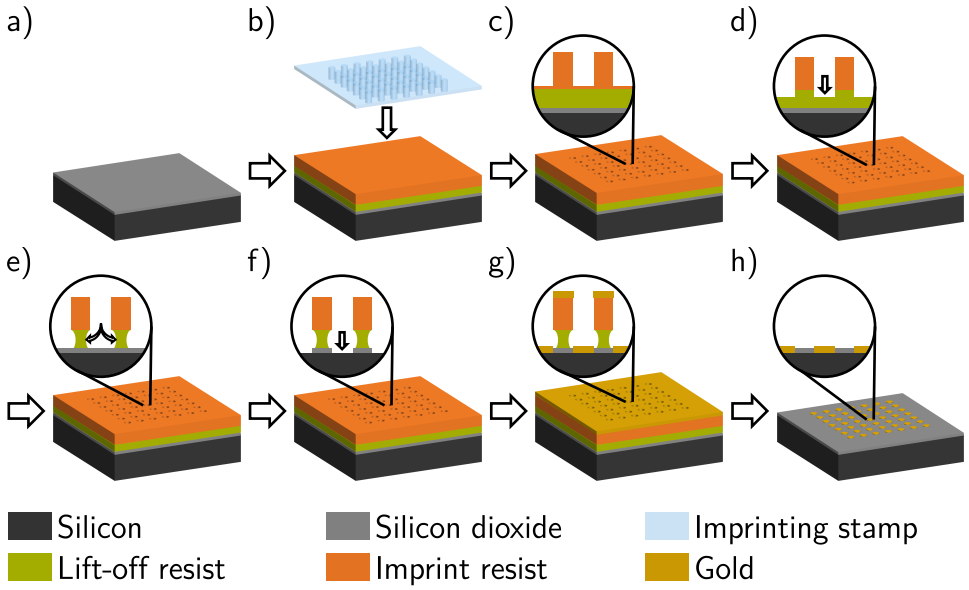

Figure 3.2: Schematic depiction of the double resist LO-NIL process of gold nanoislands embedded in a SiO_2 layer on a silicon substrate: a) The silicon substrate with a thin SiO_2 layer on top is cleaned in each DMSO, acetone, and isopropanol using an ultrasonic bath. b) The lift-off resist (green) and the imprint resist (orange) are spin coated onto the SiO_2 layer before the imprinting stamp is applied to the sample. c) The actual imprinting process transfers the features of the imprinting stamp into the imprint resist. The inset shows the inevitable residual layer of the imprint resist. d) The residual layer is removed via an anisotropic dry etching step, which also etches into the lift-off resist. e) Afterwards, an isotropic wet etching step of the lift-off resist is performed to expose the SiO_2 surface and to create an artificial undercut. f) To enable embedment of the gold, the SiO_2 layer is removed in the holes in an anisotropic dry etching step. g) Subsequently, gold is evaporated onto the sample. h) After the lift-off of both resists, the gold nanoisland array remains on the silicon surface.

imprint resist. After the cavities are filled, the sample is cooled below the glass transition temperature of the imprint resist to harden the resist. Then, the stamp is mechanically removed from the sample. Figure 3.2c shows the sample after imprinting and stamp removal. The inset of the figure shows a cross section through the sample, where the inevitable residual layer is visible. The residual layer is removed in an anisotropic dry etching step.

Note that during the dry etching of the residual layer, the lift-off resist is also partly etched. The result of the dry etching is depicted in Figure 3.2d. Next, we create an artificial undercut in the lift-off resist by an isotropic wet etching step using a suitable developer to ensure a smooth lift-off. The isotropic wet etching process additionally exposes the underlying SiO_2 layer. However, the imprint resist is not etched during the process. Figure 3.2e shows the sample after the development.

We anisotropically etch through the now exposed SiO_2 layer with another dry etching step to embed the nanoislands. The imprint resist acts as a mask for this process, and therefore we only remove the SiO_2 in the holes created by the imprinting process. The RIE process automatically terminates when the silicon surface is reached because the used gases are not etching silicon. As the selectivity between the imprint resist and the SiO_2 is poor during the dry etching process, we want to reduce the etching time to a minimum to preserve as much imprint resist as possible to ensure a smooth lift-off in the end. At the same time, we must completely penetrate the SiO_2 layer to ensure good electric contact between the metal and the silicon. Hence, we aim for etching times such that we etch a couple of nanometers more than the thickness of the SiO_2 layer. Figure 3.2f shows the sample after the SiO_2 etching. Now, we evaporate gold onto the sample as shown in Figure 3.2g. In the last step, we remove the imprint and the lift-off resist using a suitable remover in an ultrasonic bath. After the lift-off, the remaining gold nanoislands on the silicon substrate are embedded into the SiO_2 layer. Figure 3.2h shows the final embedded gold nanoislands array.

3.3 Comparison of the LO-NIL and Embedded LO-NIL Process

In the following, we look at samples fabricated with the embedded LO-NIL process and compare their quality to those fabricated with our standard LO-NIL process introduced in Section 2.2.1; the process parameters are listed in Appendix A.5. Figure 3.3 shows SEM images of embedded LO-NIL samples fabricated with the original 1400 nm, 350 nm, 200 nm, and 75 nm stamp. The top row of the figure shows overview SEM images with the same magnification for all four samples, whereas the bottom row shows zoomed-in

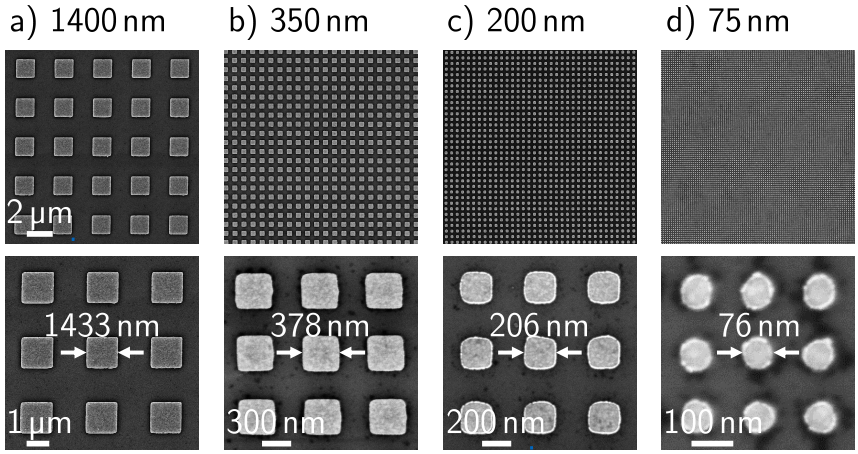

Figure 3.3: SEM images of gold nanoisland arrays fabricated with a) the original 1400 nm stamp, b) the original 350 nm stamp, c) the original 200 nm stamp, and d) the original 75 nm stamp. The top row shows an overview SEM image of each sample with the same magnification for each image. The second row shows a zoom onto the structures of each gold nanoisland array. The side lengths of the gold nanoislands are 1433(23) nm, 378(4) nm, 206(3) nm, for the original 1400 nm stamp, the original 350 nm stamp, and the original 200 nm stamp, respectively. The diameter for the original 75 nm stamp is 76(1) nm.

SEM images of the nanoislands of each sample. The overview images in Figure 3.3 show no systematic defects in the nanoisland arrays or missing islands. Therefore, the embedded LO-NIL process is not introducing defects to the nanoisland arrays, and hence the reliability of the new process is comparable to the reliability of our standard LO-NIL process.

Focusing on the zoomed-in SEM images, the shapes of the individual features are well preserved during the process for the three square and the circular stamp. For the circular 75 nm features, the edges are arguably rougher and less defined as the features of the LO-NIL samples in Section 2.2.1, which could arise from the additional etching step. However, the difference between the samples from the two methods is marginal. We measure side lengths of 1433(23) nm, 378(4) nm, and 206(2) nm for the 1400 nm, the 350 nm, and the 200 nm sample, respectively, and a diameter of 76(1) nm for the 75 nm sample. Comparing the measured sizes for the embedded structure with the non-embedded LO-NIL structures from Section 2.2.1, the measured sizes are

Table 3.1: Side length/diameter comparison of stamp pillars of all five stamps and nanoislands fabricated with them using the LO-NIL process and the embedded LO-NIL process.

	Original stamp	LO-NIL	Embedded LO-NIL
1400 nm	1412(16) nm	1445(12) nm	1433(23) nm
350 nm	357(4) nm	390(7) nm	378(4) nm
200 nm	201(2) nm	201(2) nm	206(2) nm
75 nm	74(1) nm	75(1) nm	76(1) nm

not significantly different. Table 3.1 adds the measured sizes for the embedded structures to the already known size of the used stamps and LO-NIL structures. We do not see a trend to significantly larger or smaller structure sizes between the LO-NIL and the embedded LO-NIL samples. The significant deviation of the samples produced from the original 350 nm stamp compared to the original 350 nm stamp arises from the stamp's conic shape, already discussed in Section 2.2.1.

Overall, the embedded LO-NIL process is not introducing any new systematic defects to the arrays or the individual features and therefore is as reliable as our standard LO-NIL process. Hence, we successfully extended the variability of our imprinting technique, opening up new application areas for embedded nanoisland arrays.

3.4 Application: Enhanced Hydrogen Evolution Reaction at the Metal-Insulator Interface

The electrochemical applications of our imprinted nanoisland arrays are conducted in close cooperation with the group of Professor Krischer at the Technical University of Munich. In this cooperation, our group provides the imprinted samples while Professor Krischer's group performs the electrochemical experiments. This section presents a particular electrochemical application for metal nanoislands embedded in an insulator to enhance the metal electrode's catalytic activity, utilizing a bifunctional effect at the metal-insulator interface. The electrochemical experiments for the appli-

cation were conducted by Thomas Maier from Professor Krischer's group. Parts of the presented application are already published in [30], and a detailed report on all involved experiments can be found in Thomas Maier's dissertation [57]. The application shows the opportunities created by the embedded LO-NIL process.

3.4.1 Electrochemical Fundamentals

To better understand the electrochemical application of the embedded LO-NIL samples in this section, we briefly introduce the involved electrochemical concepts. Electrochemical reactions are reactions where a charge transfer across the interface between an electrolyte and an electrode takes place [58]. In our application, we are primarily interested in the kinetics of such electrochemical reactions. After understanding the reaction kinetics and their limiting factors, we can increase the overall electrochemical reaction rate by addressing the found limiting factors.

Electrode-Electrolyte Interface

There are many different ways to create an electrode-electrolyte interface. However, this work concentrates on the interface between a metal electrode and an aqueous electrolyte, at which an electron transfer reaction can occur. Figure 3.4 schematically depicts what happens when a metal electrode is brought into contact with an electrolyte. The top row of the figure shows the band alignment happening due to the difference in the chemical potential of electrons μ between the electrode and electrolyte. The bottom row of the figure shows the influence of this band alignment on the charge carriers at the metal-electrolyte interface.

The metal and electrolyte are isolated in Figure 3.4a. The chemical potential of electrons of the metal μ_{M} lies below the chemical potential of electrons in the electrolyte μ_{E} [58]. There is no force on the charge carriers, and they can move freely in the respective system.

In Figure 3.4b, metal and electrolyte are brought into contact. In contact, an exchange of electrons between the two systems becomes possible. The difference in chemical potential leads to the formation of an electric potential $\Delta\Phi$ across the metal-electrolyte interface [59]. The electric potential establishes a force on the free charge carriers in the metal and the electrolyte.

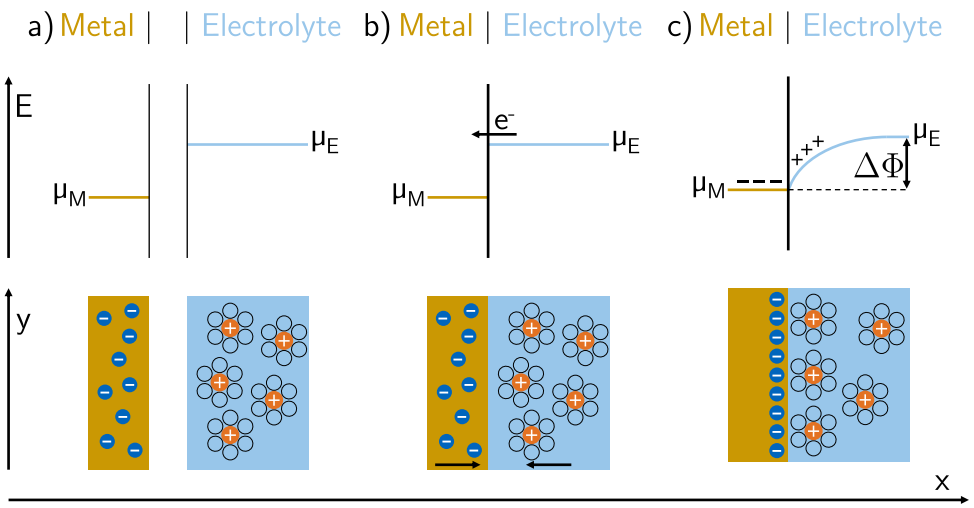

Figure 3.4: Bandalignement and formation of the electrochemical double layer at a metal-electrolyte interface. The top panel shows the energy landscape, and the bottom panel shows the behavior of the charge carriers of the system for a) the metal and electrolyte separated, b) the metal and electrolyte brought into contact, and the charges allowed to flow across the interface, and c) the equilibrium state at the metal-electrolyte interface with band alignment completed and electrochemical double layer established

.

Hence, in the metal, electrons are drawn to the interface, whereas in the electrolyte, the positively charged cations surrounded by their hydration shell are attracted toward the electrode-electrolyte interface. The accumulating charges at the surface on both sides form the so-called electrochemical double layer.

After the equilibrium state is reached, the electrochemical potentials of the metal and the electrolyte are equal at the interface, as shown in Figure 3.4c. Also, an equilibrium is reached for the charge accumulation at the interface. The accumulated electrons in the metal reside at the metal surface in a thin layer of less than 0.1 Å [58]. Therefore, no significant band bending occurs in the metal. On the electrolyte side, it is primarily the size of the cations with their surrounding hydration shell that defines the distance between the interface and the first layer of charges. Behind this compact first layer of cations, additional cations are arranged more loosely in the diffuse part of

the electrochemical double layer. The formed electric potential $\Delta\Phi$ across the interface drops across the electric double layer in the electrolyte. The exact nature of the potential drop is discussed in more detail in [60], [61].

One-Step One-Electron Reaction

First, we look at a one-step one-electron reaction, here the whole reaction can be described in one step where one electron is transferred:

$$\mathrm{O} + \mathrm{e} \rightleftharpoons \mathrm{R} \ , \tag{3.1}$$

where O is the oxidized educt and R is the reduced product of the involved chemical species. During the forward reaction, electrons flow from the electrode to the species in solution. During the backward reaction, electrons flow from the species in solution to the electrode. These electron currents are called cathodic current I_c and anodic current I_a, respectively [58]. The overall current is, per convention, defined as

$$I = I_a - I_c \ . \tag{3.2}$$

The cathodic and anodic currents are proportional to the forward and backward reaction rates, respectively [58]. Therefore, the measured current across the electrode-electrolyte interface is a good indicator of the electrochemical reaction kinetics. In equilibrium, the net current I is zero, as the forward and backward reactions are at the same rate. The equilibrium potential E_{eq} depends on the specific reaction [61]. An external potential E can be applied to the electrode to drive either the forward or the backward reaction. For the reaction, only the difference of the electrode potential E to the equilibrium potential E_{eq} of the reaction matter [62]; this difference is the so-called overpotential η:

$$\eta = E - E_{\mathrm{eq}} \ . \tag{3.3}$$

In general, the current density j is measured instead of the total current I as it is easier to compare the current density of different electrode areas. The measured current density j dependent on the overpotential η is given by the Butler-Volmer equation [61]:

$$j(\eta) = j_0 \left(e^{\frac{\beta F \eta}{RT}} - e^{\frac{-(1-\beta) F \eta}{RT}} \right) \ , \tag{3.4}$$

where j_0 is the exchange current density, β the transfer coefficient, F the Faraday constant, R the universal gas constant, and T the temperature. The kinetic parameters j_0 and β depend on the electrode material and structure. Therefore, both are indicators of the catalytic properties of the electrodes [58]. We generally want to maximize the current density j for a given overpotential η. Hence, a high j_0 is an indicator of a good catalyst.

Multi-Step Reactions

So far, we have looked at a one-step one-electron reaction, where the overall reaction involves the transfer of a single electron in a single electrochemical step. However, many electrochemical reactions require the transfer of multiple electrons. Additionally, the reaction can contain purely chemical reaction steps, where no electrons are transferred. Therefore, a general electrochemical reaction where n electrons are transferred consists of n electrochemical steps and m chemical steps [58]. Fortunately, for most electrochemical reactions, one of the $n+m$ steps is significantly slower than the other steps. The overall current density depends on the reaction rate of this rate-determining step (RDS) [58]. This RDS is influenced by the experimental environment and the used electrode material and structure [63]. The Butler-Volmer equation for multi-step reactions is given by

$$j(\eta) = j_0 \left(e^{\frac{\alpha_\mathrm{a} F \eta}{RT}} - e^{\frac{-\alpha_\mathrm{c} F \eta}{RT}} \right) , \tag{3.5}$$

where α_a and α_c are the anodic and cathodic observable charge transfer coefficients [58]. Besides those coefficients, the form of the equation is the same as its pendant of the one-step reaction. However, j_0, α_a, and α_c are now dependent on the reaction mechanism and the reaction kinetics of the RDS [58]. Hence, comparing and optimizing these quantities for different electrode materials and structures is especially interesting.

Tafel Analysis

The Butler-Volmer equation can be approximated for overpotentials far from equilibrium to experimentally evaluate the exchange current density and transfer coefficients. When the reaction is driven far away from the equilibrium, at large positive or large negative overpotentials, Equation (3.5)

simplifies to

$$j(\eta) = j_{\mathrm{a}}(\eta) = j_0 \left(e^{\frac{\alpha_{\mathrm{a}} F \eta}{RT}} \right) \tag{3.6}$$

or

$$j(\eta) = j_{\mathrm{c}}(\eta) = j_0 \left(-e^{\frac{-\alpha_{\mathrm{c}} F \eta}{RT}} \right) \ , \tag{3.7}$$

respectively. Using the logarithm, we get the anodic and the cathodic Tafel equations from Equations 3.6 and 3.7, respectively [64]:

$$\log_{10}(j_{\mathrm{a}}) = \log_{10}(j_0) + \frac{\alpha_{\mathrm{a}} F}{\ln(10) RT} \eta \tag{3.8}$$

and

$$\log_{10}(j_{\mathrm{c}}) = \log_{10}(j_0) + \frac{\alpha_{\mathrm{c}} F}{\ln(10) RT} \eta \ . \tag{3.9}$$

The measured current density is logarithmically plotted over the overpotential to evaluate the Tafel equations. From a linear fit to the data, j_0 is evaluated from the y-intersect and the respective α from the slope of the fit. Furthermore, the Tafel slope TS is defined as the inverted slope of Equations 3.8 and 3.9 [61] as

$$TS_{\mathrm{a}} = \frac{\ln(10) RT}{\alpha_{\mathrm{a}} F} \tag{3.10}$$

and

$$TS_{\mathrm{c}} = \frac{\ln(10) RT}{\alpha_{\mathrm{c}} F} \ . \tag{3.11}$$

The Tafel slope has the unit mVdec^{-1} and depends on the RDS. Hence, the overall Tafel slope indicates the RDS of the electrochemical reaction [58].

Hydrogen Evolution Reaction

The hydrogen evolution reaction (HER) is a two-electron reaction. The specific reaction mechanism differs depending on the pH value of the electrolyte. In acidic media, the HER occurs by the reduction of protons; in alkaline media, the HER occurs via the reduction of water. The HER can be divided into three elementary steps: the Volmer step, the Heyrovsky step, and the Tafel step. The overall reaction can occur by combining those steps via the Volmer-Heyrovsky or Volmer-Tafel mechanism [58]. In the following, we look at the individual reactions in acidic and alkaline media.

In acidic media, the overall HER reaction is

$$2\,H^+(aq) + 2\,e^- \longrightarrow H_2(sol)\ , \tag{3.12}$$

and the elementary steps are given by:

$$\text{Volmer step:} \qquad H^+ + e^- + * \longrightarrow H_{ad} \tag{3.13}$$
$$\text{Heyrovsky step:} \qquad H_{ad} + H^+ + e^- \longrightarrow H_2 + * \tag{3.14}$$
$$\text{Tafel step:} \qquad 2\,H_{ad} \longrightarrow H_2 + 2\,*\ . \tag{3.15}$$

The * indicates a free adsorption site on the electrode surface.

In alkaline media, the overall HER reaction is

$$2\,H_2O + 2\,e^- \longrightarrow H_2(sol) + 2\,OH^-(aq)\ , \tag{3.16}$$

and the elementary steps are given by:

$$\text{Volmer step:} \qquad H_2O + e^- + * \longrightarrow H_{ad} + OH^- \tag{3.17}$$
$$\text{Heyrovsky step:} \qquad H_{ad} + H_2O + e^- \longrightarrow H_2 + OH^- + * \tag{3.18}$$
$$\text{Tafel step:} \qquad 2\,H_{ad} \longrightarrow H_2 + 2\,*\ . \tag{3.19}$$

For most metals, it is experimentally observed that the hydrogen adsorption step, the Volmer step, is the RDS [65]. This is especially true for our systems, where we mainly use gold as electrode material. Hence, the performance of a gold electrode depends on the optimization of the hydrogen adsorption step. The catalytic activity of a metal system for hydrogen adsorption depends on multiple variables [66]–[68]. One of the main factors is the Free Adsorption Energy ΔG_{ad} of the metal surface; ΔG_{ad} should be close to zero, as for a large positive ΔG_{ad} the hydrogen will hardly adsorb to the surface and for large negative ΔG_{ad} the hydrogen will hardly desorb from the surface. A discussion of additional factors and a more in-depth analysis of particular metals can be found in [67], [68]. Overall, every enhancement of the hydrogen adsorption mechanism of our electrodes directly translates into an enhancement of the hydrogen evolution reaction, as the hydrogen adsorption step is the rate-determining step for gold electrodes.

3.4.2 Increased Hydrogen Evolution Activity of Nanostructured Electrodes

After the introduction of all necessary electrochemical concepts, we can focus on the application of the metal nanoisland arrays embedded in an insulating layer. The interface between the metal and the insulator leads to a bifunctional effect, which enhances the Volmer step of the HER in alkaline media [57]. The enhanced Volmer step increases the overall catalytic activity of the structured metal electrodes regarding the HER.

Linear Sweep Voltammetry and Tafel Analysis

We want to analyze how the different nanoisland arrays fabricated with the embedded LO-NIL method perform regarding the HER. To analyze the catalytic performance of our samples, linear sweep voltammograms (LSV) are recorded. In an LSV, an electric potential E is applied to the sample while the current density j is measured. The applied potential is given against the Reversible Hydrogen Electrode (RHE). Figure 3.5a shows the measured voltammograms for structured electrodes with structure sizes of 1400 nm, 350 nm, 200 nm, and 75 nm in an alkaline medium as a plot of j over E in V vs. RHE. The LSVs were recorded in 0.1 M NaOH/Ar sat.'d electrolyte. A good catalyst is characterized by a high current density j for small values of the electrode potential $|E|$. Looking at Figure 3.5a, the needed electrode potential for a certain current density decreases with decreasing nanoisland size. For instance, to reach a current density of 0.1 mA/cm^2 the needed potential drops by 120 mV from the 1400 nm nanoislands to the 75 nm nanoislands indicated by the orange arrow in Figure 3.5a. Thus, the catalytic activity

Table 3.2: Tafel slopes and exchange current densities for the nanostructured electrodes

Structures size d	Tafel slope	Exchange current density j_0
1400 nm	122 mV/dec	2.0×10^{-4} mA/cm^2
350 nm	121 mV/dec	4.7×10^{-4} mA/cm^2
200 nm	121 mV/dec	9.2×10^{-4} mA/cm^2
75 nm	119 mV/dec	20×10^{-4} mA/cm^2

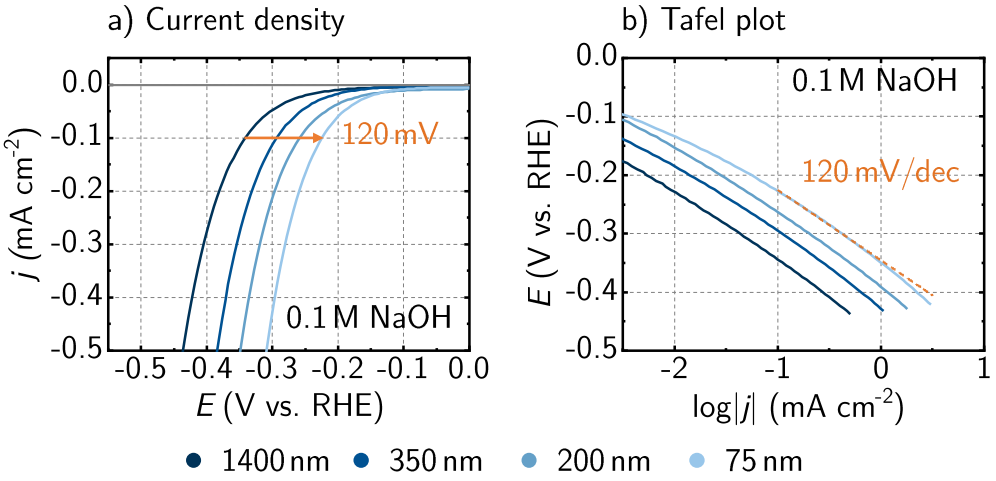

Figure 3.5: a) LSV measurements for gold nanoisland electrodes with feature sizes of 1400 nm, 350 nm, 200 nm, and 75 nm. The orange arrow shows the overpotential decrease with decreasing feature size of 120 mV. b) Corresponding Tafel plots of the LSVs in a). The orange dashed line indicates the Tafel slope of the Volmer step of 120 mV/dec of gold electrodes. The LSVs were recorded in 0.1 M NaOH/Ar sat.'d electrolyte. Adapted from [30].

regarding the HER is enhanced for the electrodes with smaller nanoisland sizes.

A Tafel analysis is performed to analyze the structured electrodes' HER kinetics further. To evaluate the Tafel slopes of the individual electrodes, E is plotted over the logarithm of j. Figure 3.5b shows the Tafel plots for the data of the structured electrodes with structure sizes of 1400 nm, 350 nm, 200 nm, and 75 nm discussed in Figure 3.5a. All plots show a linear behavior over the whole potential range. The fitted Tafel slopes given in Table 3.2 are all close to 120 mV/dec, which is exemplarily indicated for the 75 nm structures by the orange dashed line. The equal Tafel slope of 120 mV/dec for all electrodes indicates the first electron transfer as the rate-determining step for HER for all measured electrodes in alkaline media [69], [70], which is the Volmer step for the relatively low applied electrode potentials [70]–[73]. Furthermore, the exchange current density j_0 for all electrodes is extracted from the Tafel plot by linearly extrapolating the data till the y-intersect. The found j_0 for each electrode is given in Table 3.2. The exchange current

density increases with decreasing nanoisland size, also indicating a higher catalytic activity regarding the HER for smaller nanoislands.

Enhanced Catalytic Activities at the Nanoisland Edges

We attribute the enhanced catalytic activity of smaller nanoislands to the increasing edge-to-bulk ratio for decreasing nanoisland size. We assume a higher catalytic activity at the edges of the nanoislands compared to the bulk part of the islands. To verify this assumption, we make the following geometric assumptions schematically shown in Figure 3.6a. We divide the area of the nanoislands A with structure size d in an edge area A_e, a small ring with width d_e, and the bulk area A_b, where

$$A = A_\mathrm{e} + A_\mathrm{b} \ . \tag{3.20}$$

Now, we want to quantify the edge-to-bulk ratio $A_\mathrm{e}/A_\mathrm{b}$ in more detail. Under the assumption $d_\mathrm{e} \ll d$ the edge-to-bulk ratio for square features is

$$\frac{A_\mathrm{e}}{A_\mathrm{b}} = \frac{d^2 - (d-2d_\mathrm{e})^2}{(d-2d_\mathrm{e})^2} = \frac{4dd_\mathrm{e} - 4d_\mathrm{e}^2}{(d-2d_\mathrm{e})^2} \overset{d_\mathrm{e} \ll d}{=} \frac{4dd_\mathrm{e}}{d^2} = \frac{4d_\mathrm{e}}{d} \ , \tag{3.21}$$

and for square features, the edge-to-bulk ratio evaluates to

$$\frac{A_\mathrm{e}}{A_\mathrm{b}} = \frac{\left(\pi\frac{d}{2}\right)^2 - \left(\pi\frac{d}{2} - d_\mathrm{e}\right)^2}{\left(\pi\frac{d}{2} - d_\mathrm{e}\right)^2} = \frac{dd_\mathrm{e} - d_\mathrm{e}^2}{\left(\frac{d}{2} - d_\mathrm{e}\right)^2} \overset{d_\mathrm{e} \ll d}{=} \frac{dd_\mathrm{e}}{\frac{d^2}{4}} = \frac{4d_\mathrm{e}}{d} \ . \tag{3.22}$$

In the limit of $d_\mathrm{e} \ll d$, the edge-to-bulk ratio for both shapes is equal and can be approximated as A_e/A. Moreover, the edge-to-bulk ratio increases proportionally to $1/d$ for decreasing nanoisland size.

To validate the assumption that the increasing edge-to-bulk ratio for smaller nanoisland sizes enhances the catalytic activity regarding the HER, we plot the evaluated exchange current densities j_0 of each structure size over $1/d$ shown in Figure 3.6b. The blue dots indicate j_0 for each structure size. The four points show a linear increase of j_0 with the increase of $1/d$, underlined by the blue dashed line, a linear fit to the data. The golden dot indicates j_0 for a not-structured gold film at $1/d = 0$ [57]. The linear fit matches the value of the golden dot at $1/d = 0$.

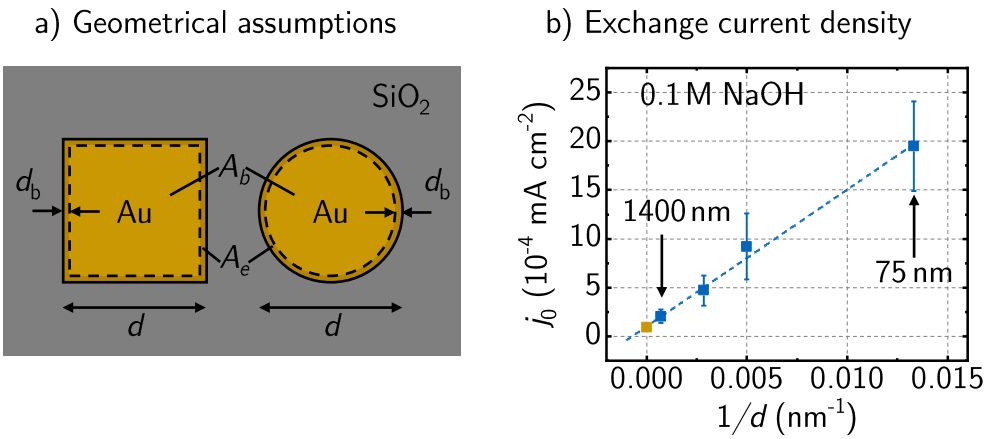

Figure 3.6: a) Geometric assumptions regarding the division of the nanoisland area into a bulk area A_b and an edge area A_e for the square and circular nanoislands. b) The exchange current density j_0 plotted versus the inverse nanoislands structure size $1/d$ in blue. The blue dashed line gives a linear fit to the data, and the golden dot shows j_0 for a continuous gold film at $1/d = 0$. Adapted from [30], [57].

We want to give a quantitative analysis for the linear dependence of j_0 on $1/d$. Therefore, we start with the overall measured current I, which can be divided into the current from the bulk area I_b and the current from the edge area I_e:

$$I = I_\mathrm{b} + I_\mathrm{e} \ . \tag{3.23}$$

With the previous geometric assumptions for the total current density j of the system Equation (3.23) translates to

$$j = \frac{A_\mathrm{b}}{A} j_\mathrm{b} + \frac{A_\mathrm{e}}{A} j_\mathrm{e} \ . \tag{3.24}$$

Inserting Equation (3.7), the current density in the Tafel approximation, into Equation (3.24), we get

$$j_0 \left(-e^{\frac{-\alpha_\mathrm{c} F \eta}{RT}}\right) = \frac{A_\mathrm{b}}{A} j_{0,\mathrm{b}} \left(-e^{\frac{-\alpha_{\mathrm{c,b}} F \eta}{RT}}\right) + \frac{A_\mathrm{e}}{A} j_{0,\mathrm{e}} \left(-e^{\frac{-\alpha_{\mathrm{c,e}} F \eta}{RT}}\right) \ , \tag{3.25}$$

with $j_{0,\mathrm{b}}$ and $j_{0,\mathrm{e}}$ the exchange current densities, and $\alpha_{\mathrm{c,b}}$ and $\alpha_{\mathrm{c,e}}$ the transfer coefficients for the bulk and the edge areas, respectively. As the Tafel

slopes for all structure sizes are similar, we can also assume similar transfer coefficients for both areas and the overall reaction:

$$\alpha_{\mathrm{c}} = \alpha_{\mathrm{c,b}} = \alpha_{\mathrm{c,e}} \ . \tag{3.26}$$

Therefore, the exponential parts of Equation (3.25) are the same for all overpotentials η. Hence, the equation simplifies to

$$j_0 = \frac{A_{\mathrm{b}}}{A} j_{0,\mathrm{b}} + \frac{A_{\mathrm{e}}}{A} j_{0,\mathrm{e}} \ . \tag{3.27}$$

Inserting Equation (3.20) in Equation (3.27) we get

$$j_0 = j_{0,\mathrm{b}} + \frac{A_{\mathrm{e}}}{A} \left(j_{0,\mathrm{e}} - j_{0,\mathrm{b}} \right) \ . \tag{3.28}$$

Last, we can insert the approximated edge-to-bulk ratio from Equation (3.21) into Equation (3.28) to get the final result of

$$j_0(d) = j_{0,\mathrm{b}} + \frac{4 d_{\mathrm{e}}}{d} \left(j_{0,\mathrm{e}} - j_{0,\mathrm{b}} \right) \ . \tag{3.29}$$

Equation (3.29) shows the linear dependence of the exchange current density j_0 on $1/d$ as evaluated in Figere 3.6. The exchange current density at $1/d = 0$ corresponds to the exchange current density of the bulk film. With decreasing structure size, j_0 increases dependent on the difference between the exchange current densities of the edge and the bulk area. The increase in j_0 confirms that $j_{0,\mathrm{e}}$ is significantly larger than $j_{0,\mathrm{b}}$ and the catalytic activity at the edges is increased compared to the bulk of the nanoislands.

Bifunctional Effect

In the previous section, we identified an increased exchange current density at the edges $j_{0,\mathrm{e}}$ of the nanoislands as the reason for the increased HER activity for smaller electrode structures. In the following, we present the assumed mechanism behind the increased $j_{0,\mathrm{e}}$. The Tafel analysis in the previous section revealed the Volmer step as the RDS for all our electrodes. Hence, the increased $j_{0,\mathrm{e}}$ can be attributed to an enhancement of the Volmer step of the HER. In an alkaline medium, the Volmer step at a gold interface is

$$\mathrm{Au^*} + \mathrm{e^-} + \mathrm{H_2O} \longrightarrow \mathrm{Au{-}H} + \mathrm{OH^-(bulk)} \ ,$$

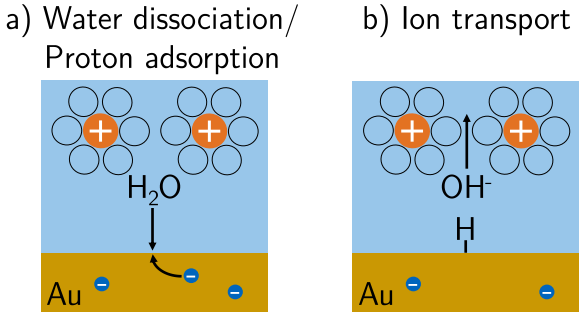

Figure 3.7: Schematic depiction of the Volmer mechanism at a gold-electrolyte interface in alkaline medium. a) The dissociation of a water molecule from the double layer region and the proton adsorption at a free adsorption site on the gold surface. b) The transport of the excess OH^- ion through the double layer into the bulk electrolyte. Adapted from [57].

here the bulk denotation indicates that the OH^- species must be transported into the bulk of the electrolyte to complete the reaction. In particular, after the reaction on the gold surface, the OH^- species must get passed the electrochemical double layer above the electrode surface. Therefore, the Volmer step at a gold film can be divided into two steps, the proton absorption on the gold surface via water dissociation and the OH^- ion transport through the double layer:

$$\begin{aligned} &\text{Proton absorption:} && \mathrm{Au^* + e^- + H_2O} && \longrightarrow \mathrm{Au{-}H + OH^-(surface)} \\ &\text{Ion transport:} && \mathrm{OH^-(bulk)} && \longrightarrow \mathrm{OH^-(surface)}\ . \end{aligned}$$

The two reaction steps are schematically depicted in Figure 3.7. Figure 3.7a shows the water dissociation and proton adsorption step. Here, a water molecule from the double-layer region reacts with an electron at a free adsorption site on the metal surface. After the adsorption step, the excess OH^- ion has to be transported through the electrochemical double layer into the bulk electrolyte, as shown in Figure 3.7b. From the literature, we know that a high polarization of the electrode is beneficial for the water dissociation and proton absorption step for various reasons [70], [74], [75]. However, a high electrode polarization of the electrode lowers the rate of the OH^- ion transport step [72]. As a higher electrode polarization increases the rigidity of the electrochemical double layer, the energy needed for the OH^- ion to

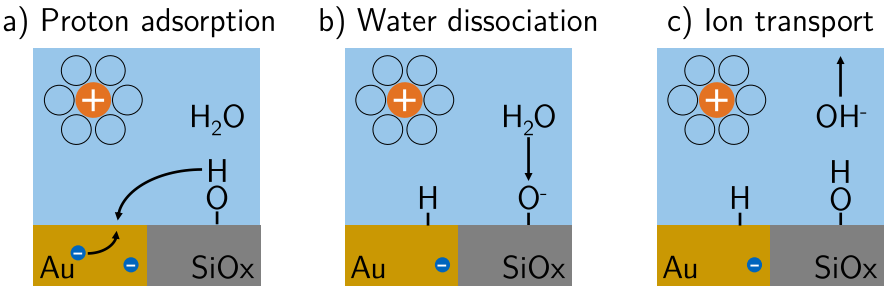

Figure 3.8: Schematic depiction of the proposed bifunctional Volmer mechanism at a gold-insulator-electrolyte interface in alkaline medium. a) The proton adsorption of a proton from the O−H termination of the insulator at a free adsorption site on the gold surface. b) The dissociation of a water molecule at the insulator surface. c) The transport of the excess OH^- ion through the double layer free region into the bulk electrolyte. Adapted from [57].

penetrate the double layer increases. The counteracting dependence of the rates of both steps on the electrode polarization hinders an effective enhancement of the Volmer step at continuous gold surfaces. Hence, the exchange current density for bulk gold $j_{0,\mathrm{b}}$ is limited.

By structuring the electrode surface using the embedded LO-NIL method, we introduce a metal-insulator interface at the edges of each nanoisland to the system. We assume the Volmer reaction mechanism to change due to the presence of the insulator [57]:

$$\begin{aligned}
&\text{Proton absorption:} && \mathrm{Au^* + Si{-}OH + e^-} && \longrightarrow \mathrm{Au{-}H + Si{-}OH^-} \\
&\text{Water dissociation:} && \mathrm{Si{-}OH^- + H_2O} && \longrightarrow \mathrm{Si{-}OH + OH^-(surface)} \\
&\text{Ion transport:} && \mathrm{OH^-(bulk)} && \longrightarrow \mathrm{OH^-(surface)}\ .
\end{aligned}$$

Figure 3.8 schematically depicts the steps of the proposed mechanism. The presence of the insulator, in this case SiO_2, splits the proton absorption and water dissociation step into two separate steps because the SiO_2 acts as a local proton source for the system. For that, a proton from the O−H terminated insulator surface spills over onto a free adsorption site at the gold nanoisland. The spillover is shown in Figure 3.8a. Afterward, the water dissociation happens on the new O^- termination of the SiO_2 surface, depicted in Figure 3.8b. Last, the OH^- ion is transported towards the bulk electrolyte

in the insulator region where the characteristic of the electrochemical double layer is advantageous for the transport, shown in Figure 3.8c. The new bifunctional mechanism has two major advantages compared to the previous Volmer mechanism. First, with the hydrogen spillover from the insulator and the water dissociation happening at the insulator surface, no water molecule from the double layer above the metal surface must be dissociated. Thus, the proton adsorption and water dissociation processes are spatially decoupled [57]. Second, the excess OH^- ion must not get passed the electrochemical double layer above the metal electrode, which safes the reorganization energy of the double layer penetration. Hence, the ion transport becomes energetically more favorable. Both effects lead to an enhanced catalytic activity of the edge area of the nanoislands [57].

It is important to state that besides the proposed effect, other edge effects also play a role in the behavior of the nanostructured electrodes. However, the discussion of those effects is beyond the scope of this work. In this work, we focused on introducing the bifunctional effect, which is achievable due to the possibility of embedding metal nanoisland arrays into an insulating layer using the embedded LO-NIL fabrication method. For an in-depth analysis of the bifunctional effect and other catalytic properties of our structured nanoisland electrodes, we refer to [57].

Chapter 4

Nanopatterning of Semiconductor Metasurfaces

With our standard LO-NIL and embedded LO-NIL process, we can fabricate nanostructured samples by evaporating a material onto the surface of a substrate. However, for some applications, it is not possible to evaporate the desired materials; for example, crystalline structures can hardly be evaporated. Thus, the two LO-NIL methods do not apply to those systems. Nevertheless, a nanostructuring of non-evaporable materials is desired in various applications. For example, the nanostructuring of semiconductors enables applications in nanophotonics. Therefore, we developed a method to etch the nanofeatures into the substrate rather than evaporating them on top. We use an inverted imprinting stamp for the new method to fabricate imprint resist pillars instead of holes in the resist. Later, the imprint resist pillars are directly used as the mask for the etching process of the sample features. In the following, we refer to the new nanostructuring method as the direct etching NIL process.

4.1 The Direct Etching Nanoimprint Lithography Process

We introduce the direct etching NIL process exemplarily for fabricating gallium phosphide (GaP) nanopillars. Figure 4.1 schematically depicts the direct etching NIL process. Before the process, the substrate is cleaned in each DMSO, acetone, and isopropanol using an ultrasonic bath. Figure 4.1a shows the substrate after the cleaning procedure. Next, the imprint resist is applied

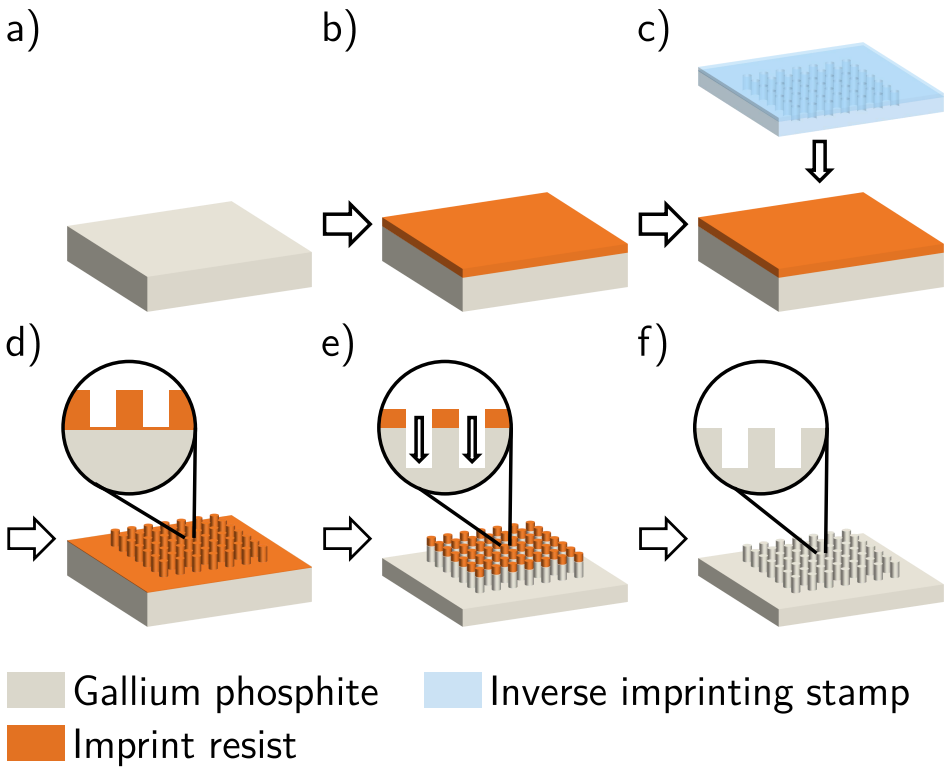

Figure 4.1: Schematic depiction of the direct etching NIL process to fabricate GaP nanopillars: a)The GaP substrate is cleaned in each DMSO, Acentone, and isopropanol using an ultrasonic bath. b) The imprinting resist (orange) is spin coated on the GaP substrate. e) After the spin coating, the inverse imprinting stamp is applied to the sample to generate resist pillars during the imprinting process. d) The imprinting process produces cylindrical resist nanopillars. Also, the process leaves an inevitable residual layer on the substrate surface. e) Using the resist nanopillars as an etching mask, the pillars are transferred into the GaP substrate via an anisotropic dry etching step. f) Last, the remaining imprint resist is removed.

to the sample via spin coating. Note that no lift-off resist is needed for the direct etching NIL process. Figure 4.1b shows the sample with applied imprint resist. For the imprinting process, we use an inverse imprinting stamp to create resist pillars rather than holes in the resist. The inverse imprinting stamps are fabricated by adding an additional OrmoStamp replication

cycle to the working stamp fabrication process, described in Section 2.1.2. Figure 4.1c shows the sample and inverse imprinting stamp before the imprinting process. During imprinting, the stamp-sample stack is heated above the glass transition temperature of the imprint resist. Here, the imprint resist becomes viscous, and the imprinting stamp is pressed into the imprint resist until the cavities of the imprinting stamp are filled. Afterward, the stamp-sample stack is cooled below the glass transition temperature to harden the imprint resist. Now, the stamp is mechanically removed from the sample. The imprint resist is now patterned in the form of pillars on the sample surface shown in Figure 4.1d. The inset in the figure shows a cross section through the sample where the pillars and the inevitable residual layer of the imprint resist are visible. We choose the initial thickness of the imprint resist to minimize the residual layer's thickness while ensuring the full height of the pillars.

Next, the resist pattern is transferred into the gallium phosphide substrate via an anisotropic RIE step. In this process, the pillars of the imprint resist act as the mask for the etching process. The used dry etching process also etches the imprint resist. Hence, the imprint resist's residual layer must not be removed before etching. The residual layer is first etched away during the dry etching process, then the GaP is etched. Figure 4.1e shows the sample during the anisotropic RIE step. The poor selectivity between the imprint resist and the GaP regarding the RIE process also leads to a limited maximal achievable height of the GaP pillars. The maximal height is reached when the imprint resist pillars are entirely removed during the etching step. For GaP, the imprint resist is etched twice as fast as the substrate. Hence, the maximal GaP height is half the height of the features of the used imprinting stamp. After the dry etching, the sample is cleaned in each DMSO, acetone, and isopropanol using an ultrasonic bath to remove all imprint resist residuals. The final sample is shown in Figure 4.1f.

4.2 Application: Photoengineering Gallium Phosphide for Enhanced Solar Energy Harvesting

The direct etching NIL process was developed for application in semiconductor photocatalysis. Here, semiconductors act as the light-harvesting and catalytic active medium to convert solar into chemical energy [76]. Unfortunately, these semiconductor materials are usually non-evaporable. Therefore, the nanostructuring has to be performed via etching of the materials, making the direct etching NIL process the optimal choice for fabrication. The semiconductor photocatalysis applications of imprinted nanoisland arrays were conducted in close cooperation with Ludwig Hüttenhofer from the Ludwig Maximilians University Munich. In this cooperation, our group provided the imprinting know-how and carried out the imprinting processes while Ludwig Hüttenhofer performed the experiments and analysis. This section briefly introduces the application of the direct etching NIL process for fabricating GaP metasurfaces. These metasurfaces exhibit an enhanced solar light harvesting performance due to anapole excitations. The presented application is already published in [77], and a detailed report of all involved experiments can be found in Ludwig Hüttenhofer's dissertation [78].

4.2.1 Fundamental Concepts of Nonradiative Nanophotonics

In the following, we introduce the fundamental concepts of semiconductor photocatalysis and photoengineering. The energy needed to split a water molecule is 1.23 eV per electron treansferred [79]. Therefore, the band gap energy of a semiconductor photoelectrode must exceed 1.23 eV to drive solar water splitting. Additionally, the necessary alignment of the semiconductor band gap with the redox potentials of the water splitting reaction increases the band gap energy of a suitable semiconductor to 1.6–2.4 eV [79]. For photocatalytic water splitting applications, high absorption of the incoming sunlight is favorable to increase the solar energy conversion capabilities of the device. However, with the visible spectrum ranging from about 1.5–3.0 eV, most suitable semiconductors cannot absorb sunlight over the whole spectral range because they can only absorb light with photon energies exceeding their

band gap energy.

Photonic engineering aims to enhance or extend the absorption capabilities of the semiconductors by structuring the material accordingly. The overall goal is to increase the absorbed power P_{abs} of the semiconductor by enhancing the electromagnetic field E inside the semiconductor volume V as the absorbed power directly links to E via

$$P_{\text{abs}} = \frac{\pi c}{\lambda} 2nk \int |E|^2 \, dx \tag{4.1}$$

with n and k the real and imaginary parts of the refractive index of the semiconductor, respectively [78]. The parameters n and k are dependent on the used material and are frequency dependent. Therefore, the chosen semiconductor dictates the basic absorption characteristics of the absorber. Semiconductors suitable for water splitting usually have low k values for visible and near-infrared light due to the constraints regarding the band gap energy and the band alignment.

To enhance the absorbance, we must increase E inside the semiconductor volume. Note that for non-absorbing materials with $k = 0$, an increase in E would not result in increased absorption. Thus, only the absorbance of materials, which already absorb light with $k > 0$, can be enhanced by photonic engineering.

An increase in E can be achieved by engineering and structuring the semiconductor [78]. In this work, we introduce the structuring of GaP into nanoislands to excite nonradiative anapole excitations and evoke lattice modes due to coupling between individual islands of the nanoisland arrays [77]. Both effects lead to increased confinement of E inside the semiconductor volume.

Anapole Excitations

Anapole excitations (AE) are nonradiative excitations that enable the confinement of the incident light into subwavelength volumes [80]. The far-field scattering for AEs is suppressed compared to radiative excitations such as electric and magnetic dipole resonances, which scatter most of the absorbed photon energy radiatively into the far field. The suppression of the far-field scattering arises from the interplay of multiple photonic modes inside the illuminated particle [81]. The material and geometrical conditions for anapole states can be derived from Mie theory [82]. The formalism established for

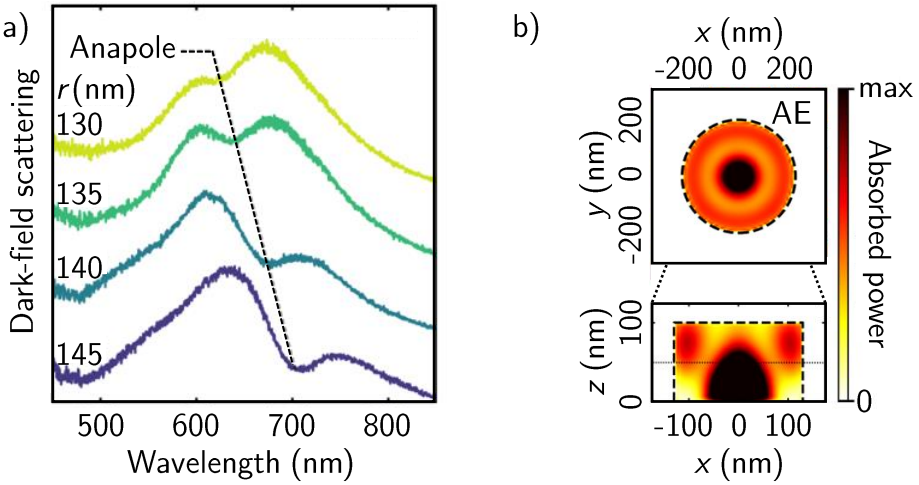

Figure 4.2: a) Dark-field scattering spectra of single GaP nanoislands with varying radii. b) Color map of the absorbed power profile for the AE of a GaP nanoisland as horizontal and vertical cross sections. Adapted from [77].

metallic particles can be equally applied to semiconductor materials. However, the mathematic derivation of the anapole states is beyond the scope of this work. A comprehensive derivation of the conditions for anapole states can be found in [83].

The light-scattering characteristics of single nanoislands can be characterized using dark-field scattering. The investigated nanoislands were fabricated using electron beam lithography [77]. Figure 4.2a shows dark-field scattering spectra for individual nanoislands with different radii r. For all nanoislands, a dip in the spectra is visible. This scattering minimum can be related to the AE, for which far-field scattering is suppressed. The AE-related scattering minimum red shifts with increasing r. Therefore, the spectral position of the AE can be shifted by engineering the nanoisland radius. Figure 4.2b shows the absorbed power profile of an AE in a GaP nanoisland with radius $r = 130\,\text{nm}$ and height $h = 100\,\text{nm}$ for depolarized excitation. The top image illustrates a top view of the power profile at $z = h/2$, and the bottom image illustrates a side view at $y = 0$. The absorbed power was calculated from FDTD simulations of the electric field distribution in the nanoislands [77]. The confined electromagnetic field in the nanoislands leads to high absorbed power in the bottom center part of the nanoislands. Therefore, tuning the

AE to a spectral region where the nanoisland material lacks absorption capabilities can enhance the overall absorption performance of the structured semiconductor.

Lattice Resonance

So far, we have looked at the excitation of a single nanoisland. Now, we look at the influence of a nanoisland array on the AE of the system. Therefore, arrays with 20×20 GaP nanoislands are prepared using electron-beam lithography [77]. Besides the radius r of the individual islands, the center-to-center distance, the pitch p, of the arrays is varied. Figure 4.3a shows transmittance spectra of the nanoisland arrays. The upper panel shows the transmittance spectra of five nanoisland arrays with varying r and $p = 350\,\text{nm}$. In comparison, the lower panel shows the transmittance spectra of five nanoisland arrays with the same r variation but $p = 400\,\text{nm}$. In both panels, all spectra have a pronounced transmittance minimum. The minimum transmittance arises from a maximum absorbance due to AEs in the nanoislands [77]. The spectral position of the AEs red shifts with increasing r in accordance with the dark-field scattering measurements above. Additionally, the overall transmittance decreases with increasing r, which can be related to a higher fill factor of the sample surface for larger nanoislands. However, the wavelength of the AE is not dependent on the pitch of the nanoislands as the position of the AE-related transmission minima remains nearly unchanged from $p = 350\,\text{nm}$ to $p = 400\,\text{nm}$.

Besides the pronounced minimum due to the AE, a second dip in transmittance arises for the spectra. In the upper panel, the second transmission minimum lies at 525 nm and is independent of r. For the spectra in the lower panel, the additional minimum lies at 600 nm. The additional transmission minima can be assigned to an emerging lattice resonance (LR) [77]. The spectral position of the LR is dependent on the pitch p of the nanoisland arrays but independent of the radius r of the individual nanoislands. Hence, the spectral position of the LR can be shifted by engineering the pitch of the nanoisland array.

Figure 4.2b shows the absorbed power profile of an LR in a GaP nanoisland array with $r = 130\,\text{nm}$, $h = 100\,\text{nm}$, and $p = 350\,\text{nm}$ for depolarized excitation. The top image illustrates a top view of the power profile at $z = h/2$, and the bottom image illustrates a side view at $y = 0$. The absorbed power

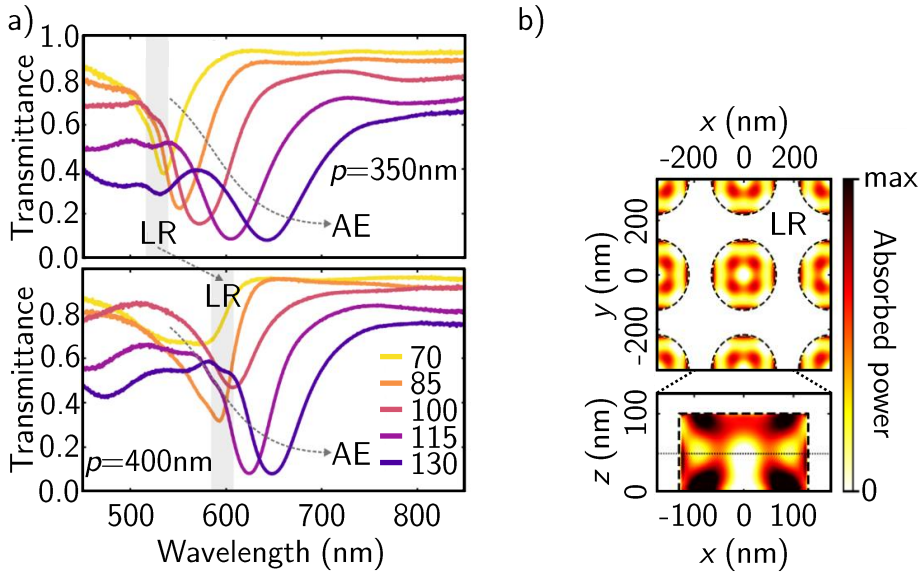

Figure 4.3: a) Transmission spectra of GaP nanoislands arrays with varying radii and pitch. b) Color map of the absorbed power profile for the LR of a GaP nanoisland array as horizontal and vertical cross sections. Adapted from [77].

was calculated from FDTD simulations of the electric field distribution in the nanoislands [77]. The LR promotes absorption hotspots at the edges and the top face of the nanoisland, thus closer to the surface of the nanoisland than the AEs.

Overall, the spectral position of the AE and the LR of a nanoisland array can be shifted separately. While the AE depends on the radius of the individual nanoislands, the LR depends on the center-to-center distance between the nanoislands. Therefore, smart engineering of the nanoisland array properties allows the optimal use of both absorption enhancement mechanisms.

4.2.2 Increased Sunlight Harvesting in Imprinted Gallium Phosphide Metasurfaces

Gallium phosphide is a suitable semiconductor for applications in photocatalytic water splitting [84]. The band gap energy of GaP exceeds the needed energy for water splitting, and the band edges align with the redox potentials

of the reaction. However, GaP is an indirect semiconductor, which weakens the absorption capabilities for wavelengths $\lambda > 450\,\text{nm}$ [85].

We aim to enhance the absorption of the GaP device by nanostructuring the surface via direct etching NIL applying the concepts of AE and LR introduced in the previous section. To best increase the absorption in the GaP, the spectral position of AE and the LR must lie in the weak absorption regime at $\lambda > 450\,\text{nm}$. Furthermore, the AE and LR should be spectrally separated to maximize absorption and cover a more extensive spectral range. For that, a nanoisland array with a pitch p of 350 nm, nanoisland diameter d of 260 nm, and height of 100 nm is applicable because, as seen in Figure 4.3a, the spectral positions of the arrays AE and the LR are around 525 nm and 650 nm, respectively.

Gallium Phosphide Nanoisland Array Fabrication

For the GaP nanoisland arrays with $d = 260\,\text{nm}$ and $p = 350\,\text{nm}$, a new imprinting stamp must be fabricated because our previously used imprinting stamps have different pitches and diameters. The new stamp is fabricated with electron-beam lithography. A detailed description of the fabrication process can be found in [78]. Figure 4.4a shows SEM images of the new imprinting stamp. The top image shows an overview of the nanopillar array. The pillars are arranged in a cubic lattice with the desired pitch of 350 nm. The electron-beam lithography process introduced no systematic defects or missing islands to the stamp. The bottom image shows a zoomed-in SEM image on the pillars of the stamp. We measure a pillar diameter of 199(10) nm, which is significantly smaller than the desired diameter of 260 nm. However, the diameter for the stamp pillars was purposely chosen to be smaller than the desired diameter of the GaP nanoislands as the direct etching NIL process increases the feature diameter during the process. Note that the feature height is halved during the direct etching NIL process. Therefore, the height of the pillars of the imprinting stamp is 200 nm to achieve 100 nm in height for the nanoislands.

Figure 4.4b shows SEM images of a GaP nanoisland array fabricated with the new imprinting stamp using the direct etching NIL process; the process parameters are listed in Appendix A.5. Again, the top image shows an overview of the nanoisland array with no defects or missing islands. Thus, the direct etching NIL process reliably transfers the stamp pattern into the

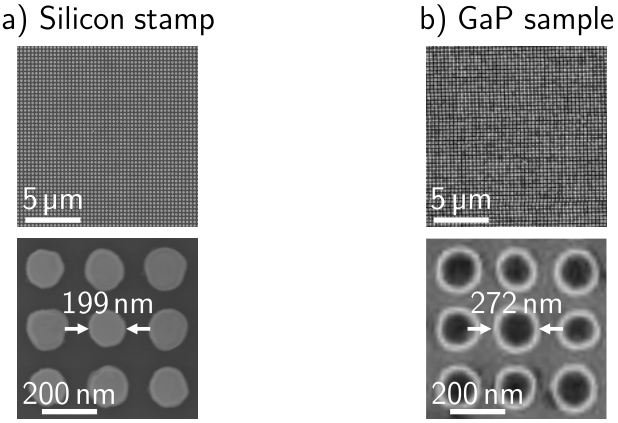

Figure 4.4: SEM images of a) the custom-build imprinting stamp and b) the GaP nanoisland array fabricated with the custom-build stamp [77]. The respective top image shows an overview SEM image of the stamp and sample, and the respective bottom image shows a zoom of the structures of the stamp and sample. The diameters of the structures are 199(10) nm and 272(11) for the stamp and sample, respectively. Adapted from [77].

GaP layer. The zoomed-in SEM image at the bottom shows the individual GaP nanoislands with a measured diameter of 272(11) nm. We attribute the increased diameter of the nanoislands compared to the stamp pillars to charging effects during the dry etching of the GaP. Charges accumulate in the insulating imprint resist during the RIE process. As a result, the arising electrical fields deflect further incoming ions, and the effective area of the resist mask increases. Nevertheless, the final nanoisland diameter is sufficiently close to the desired diameter of 260 nm. In the following sections, we analyze the properties of the resulting GaP metasurface.

Optical Characterization of the GaP Nanoisland Array

After the fabrication of the GaP metasurface via direct etching NIL, the sample is characterized via optical transmission and reflection spectroscopy under perpendicular illumination. Figure 4.5a shows the measured transmittance, reflectance, and absorbance spectrum of the GaP metasurface for the visible spectrum. The grey line in the figure indicates the terrestrial solar spectrum. The signatures of the LR and the AE are pronounced in the

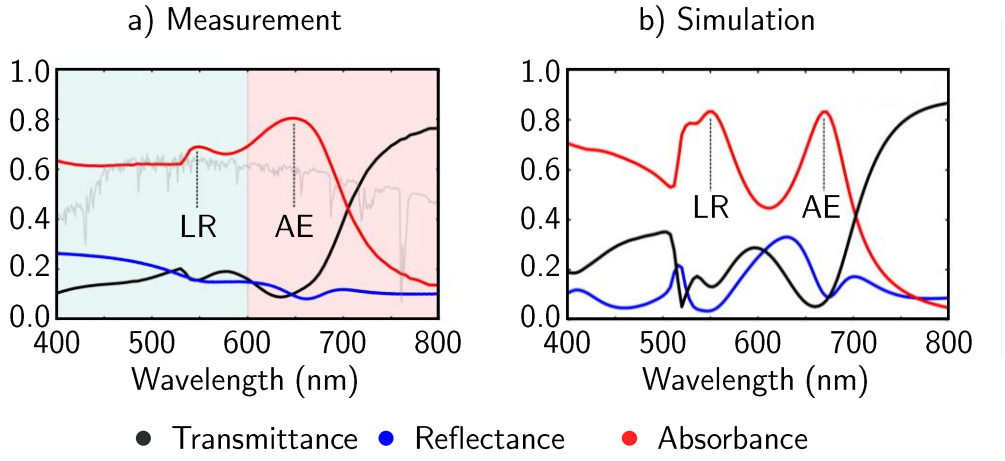

Figure 4.5: a) Measured transmission, reflection, and absorption spectra for the GaP metasurface. The grey line indicates the terrestrial spectrum of the sun. The LR and AE are indicated for the absorption spectrum. b) Simulated transmission, reflection, and absorption spectra for the GaP metasurface. The LR and AE are indicated for the absorption spectrum. Adapted from [77].

transmittance and the absorbance spectrum at $\lambda = 550\,\text{nm}$ and $\lambda = 640\,\text{nm}$, respectively. The measurements are compared with FDTD-simulated spectra of the GaP metasurface. Figure 4.5b shows the simulated transmittance, reflectance, and absorbance spectra for the metasurface under perpendicular illumination. The simulation provides good agreement with the measured data. The additional sharp transmission minimum at $\lambda = 520\,\text{nm}$ is attributed to a simulation artifact, which was also observed in previous FDTD simulations [77]. The transmission minima at $\lambda = 550\,\text{nm}$ and $\lambda = 660\,\text{nm}$ are assigned to the LR and the AE of the nanoisland array, respectively [77]. The simulation confirms that the minima in transmission arise from maxima in absorption. Thus, the nanostructuring of the GaP surface leads to an enhanced absorption in the spectral range at $\lambda > 450\,\text{nm}$.

Enhanced Solar Energy Harvesting of the Gallium Phosphide Metasurface

We want to evaluate the overall solar energy harvesting capabilities of the GaP metasurface. The aim is to use the enhanced absorption to increase the photocatalytic activity of the GaP semiconductor catalyst. In the following, we want to compare the performance of a flat GaP film and the GaP metasurface. Figure 4.6a compares absorbance spectra for a flat GaP film and the GaP metasurface. Here, the red line shows the spectrum of the metasurface, and the dashed red line shows the spectrum of the film. The absorbance of the metasurface is higher for $\lambda > 550\,\mathrm{nm}$. The spectral region for enhanced absorption corresponds to the spectral positions of the LR and the AE in the metasurface. The decreased absorbance of the metasurface away from the AE is attributed to its smaller surface fill factor compared to the film because only about 50 % of the substrate are covered with GaP pillars [78].

Last, the catalytic performance regarding the hydrogen evolution reaction (HER) between a flat GaP film and the metasurface is tested. The conversion rate of solar energy into chemical energy is the determining factor to evaluate the solar energy harvesting performance of the GaP electrodes. Therefore, the incident-photon-to-current conversion efficiency (IPCE) is calculated as a figure of merit. The IPCE is the quotient of incoming photons and photoexcited electrons transferred in the electrochemical reaction:

$$\mathrm{IPCE} = \frac{c\,h\,I_{\mathrm{ph}}}{\lambda\,P_{\mathrm{light}}} \tag{4.2}$$

with c the speed of light, h the Planck constant in eV, and I_{ph} and P_{light} the photocurrent and the irradiance of photons at wavelength λ, respectively. The values of I_{ph} are calculated from chronoamperometry measurements under chopped light excitation. The chopping of the light excitation allows the calculation of only the current arising from the illumination of the sample [78].

Figure 4.6b shows the IPCE for a GaP film and the metasurface in light and dark green, respectively. The IPCE of the metasurface exceeds the IPCE of the film over the whole spectral range despite the absorption of the metasurface only being higher than the absorption of the film for $\lambda > 550\,\mathrm{nm}$. Therefore, the metasurface must possess more beneficial characteristics enhancing the HER than just enhanced light absorption. Among those characteristics is the increased surface-to-volume ratio of the metasurface compared

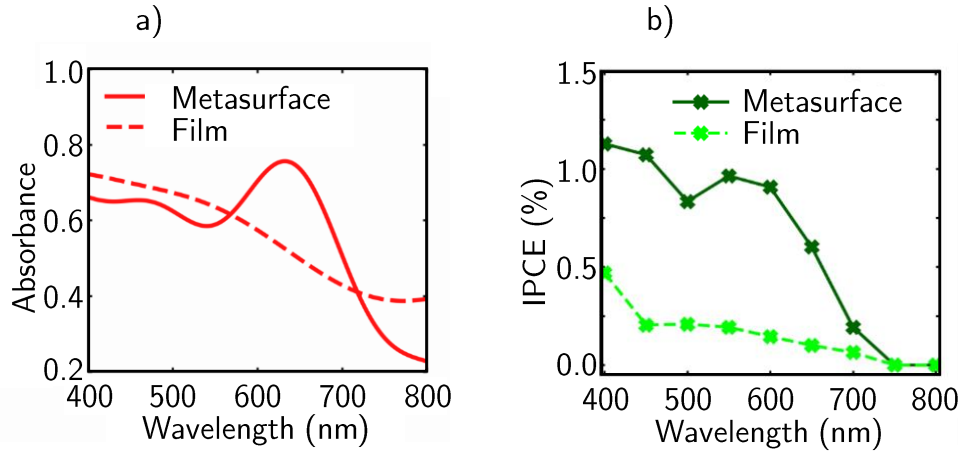

Figure 4.6: a) Absorption spectra of the GaP metasurface and a GaP film with platinum co-catalyst applied in each case. b) Incident photon-to-current conversion efficiency of photoelectrodes based on the GaP metasurface and a GaP film. The metasurface outperforms the film over the whole spectral range. Adapted from [77].

to a flat film, which increases the number of catalytically active sites [77]. Furthermore, the nanostructuring decreases the average distance between the excitation spot of the electrons and the electrode-electrolyte interface, which decreases the recombination probability during the migration towards the surface [78]. However, a detailed analysis of the involved mechanisms is beyond the scope of this work. For an in-depth discussion of the involved processes and conducted experiments regarding the solar energy harvesting of the GaP metasurface, we refer to the dissertation of Ludwig Hüttenhofer [78]. Nevertheless, we showed the possible application of the direct etching NIL process to enhance the photocatalytic performance of semiconductor photocatalysts like GaP.

Chapter 5

Imprinting Stamp Feature Size Tuning

The features fabricated with every NIL process depend highly on the used imprinting stamp. However, the production of original stamps for NIL processes is a time-consuming and resource-intensive process. Therefore, producing a new original stamp for each experiment to change the feature sizes slightly is not feasible. Thus, a lack of structural versatility arises for the final imprinted structure. To overcome these limitations, we developed processes to tune the final feature sizes of our imprinted nanoisland arrays.

To prevent the original stamps from being damaged, we never use them directly for our imprinting processes. Instead, we use the original stamps as templates for semi-flexible single-use working stamps [34], [42] as described in Section 2.1.2. Preferably, we would like to tune the features of these working stamps. However, the features of the working stamps are not tunable, neither via dry nor wet etching techniques. Thus, to tune the dimensions of the imprinting stamp and preserve the original stamp, we must fabricate a new stamp, which can be used as the new original stamp for the working stamp fabrication. There are two possible methods to achieve size tuning of the imprinted features; we can either tune the features of the imprinting stamp before the imprinting process (stamp tuning) or the features in the imprint resist during the NIL process (resist tuning).

Resist tuning is performed by altering the dimensions of the imprint resist features after the imprinting process; for example, by using V-shaped imprinting stamps where anisotropic etching of the resist increases the width of the fabricated lines [39], by imprinting in combination with angeled evaporation to decrease the width of grating lines [86], or by isotropically widening

imprinted holes in a resist to increase the size of imprinted nanoislands [28]. The advantage of the resist tuning approach is its versatility and adaptability during the process. The disadvantages of the resist tuning approach are the complexity of the process and that resist tuning techniques only allow to remove resist in the process; therefore, it only allows the increase of holes or grooves in the resist. Thus, the feature sizes of the final NIL structures can only be tuned larger when using a lift-off process, or they can only be tuned smaller when using an etching process.

Other than that, stamp tuning makes it possible to tune the size of the stamp features directly. As a result, the final imprinted structures can be smaller or larger, independent of the later imprinting process. For example, the imprinting mold is isotropically etched to decrease the feature size [32] or isotropically coated with a suitable coating to increase the feature size [87]. Additionally, laser melting allows for reshaping the features of a stamp [88], or multi-stack imprinting allows for fabricating stamps with a combination of different stamps [89]. The advantage of the stamp tuning approach is the enhanced reproducibility of samples compared to resist tuning, as one tuned stamp acts as a template for all samples of one size produced with NIL. Furthermore, once tuned, the stamp can be used in all established imprinting methods, and no more complex procedures must be applied. The disadvantage of the stamp tuning approach is that the original stamp itself is altered, and the original pattern is lost. Thus, a replica must be fabricated before tuning to preserve the original stamp.

In this work, we focus on stamp tuning processes to decrease the size of the imprinted features. Furthermore, we want to utilize the light-matter interactions of the metal nanoislands in later experiments. Thus, we are particularly interested in tuning the 75 nm imprinting stamp, as the metal nanoisland arrays fabricated with this stamp show light-matter interactions in the visible regime. However, as the fabrication process of the 75 nm metal nanoisland arrays is delicate, we use the 200 nm stamps first to check the feasibility of our tuning processes.

Inspired by our existing resist tuning process, we developed a first tuning process where we use isotropic dry etching of the imprint resist to tune the feature size of SiO_2 stamps referred to as the resist tuning process. An inverted working stamp creates resist pillars on SiO_2, which are tuned and act as an etching mask to transfer the newly sized pillars into the SiO_2. The process can fabricate tuned imprinting stamps. However, nonuniform

Table 5.1: Properties and limitations of the three nanoimprinting stamp tuning processes.

	Resist tuning	**Resist HF tuning**	**Chromium HF tuning**
Complexity	low	medium	high
Tuning material	Imprint resist	SiO_2	SiO_2
Etching mask	Imprint resist	Imprint resist	Chromium
Successful tuning	No	350 nm stamp	Yes
Limitations	Shape retention, Feature height	Feature height	None

etching of the imprint resist limits the reliability of the process.

Therefore, we advanced the process by shifting the tuning process from the imprint resist into the SiO_2. So, we first used the resist pillars as an etching mask to transfer the stamp pattern into the SiO_2 and then tuned their size using a hydrofluoric acid (HF) base solution. The advanced process is called the resist HF tuning process. The shift of the tuning process enabled a smoother tuning process. However, the poor selectivity between the imprint resist and the SiO_2 limits the feature height of the new stamp, which prohibits the fabrication of nanoisland arrays.

We exchanged the imprint resist pillars with chromium nanoislands to overcome the height limitations. Those chromium nanoislands are fabricated with our standard LO-NIL process and increase the selectivity during the SiO_2 dry etching. The new process allows us to fabricate feature heights comparable to the original stamps and tune the feature size reliably below 30 nm. The final chromium HF tuning process is published in [55].

Table 5.1 summarizes the properties and limitations of the three tuning processes, which are introduced in more detail in the rest of this chapter.

5.1 The Resist Tuning Process

Inspired by our previous resist tuning process to increase the size of metal nanoislands [28], we developed the resist tuning process utilizing isotropic etching of the imprint resist. We combine the resist tuning process with the

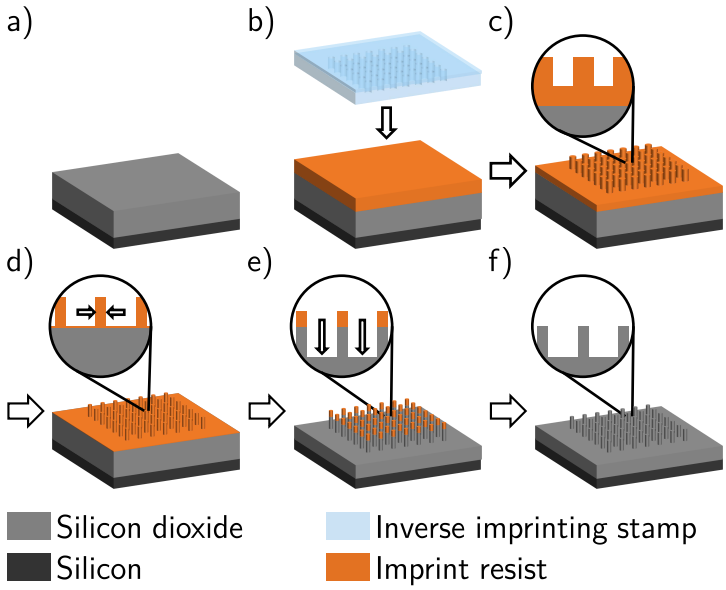

Figure 5.1: Schematic depiction of an imprinting feature tuning process. The imprinted feature sizes are tuned by tuning the dimensions of the imprinting resist and using the tuned resist features as a dry etching mask for an anisotropic RIE process. a) The silicon/chSiO2 substrate is cleaned in each DMSO, Acentone, and Isopropanol using an ultrasonic bath. b) The imprint resist (orange) is spin coated onto the SiO_2 surface before the inverse imprinting stamp is applied to the sample. c) The imprinting process produces cylindrical resist nanopillars. Also, the process leaves an inevitable residual layer on the substrate surface. d) The diameter of the resist nanopillars is tuned via an isotropic dry etching step. e) Using the tuned resist nanopillars as an etching mask, the pillars are transferred into the SiO_2 via an anisotropic dry etching step. f) Last, the remaining imprint resist is removed.

direct etching NIL from Section 4.1 to fabricate a tuned imprinting stamp. For that, we use SiO_2 as the material for the tuned stamps, as we can reliably etch SiO_2 in an anisotropic RIE process.

Figure 5.1 schematically depicts the developed stamp tuning process. We start by cleaning a silicon substrate with a SiO_2 layer in an ultrasonic using each DMSO, acetone, and isopropanol. Figure 5.1a shows the cleaned substrate. After cleaning, we apply the imprint resist to the SiO_2 surface via spin coating. Figure 5.1b shows the sample after the spin coating of the imprint resist and before the imprinting step. Next, we use an inverted

working stamp to fabricate resist pillars on top of the SiO_2 surface in the imprint resist. During the imprinting step, the stamp is pressed into the resist forming pillars on top of the SiO_2.

Figure 5.1c shows the sample after imprinting. We choose the thickness of the imprint resist so that a sufficiently thick residual layer remains for the isotropic shrinking of the resist pillars. The resist pillars and the thick residual layer are shown in the inset of Figure 5.1c. Now, we use a RIE process to shrink the resist pillars isotropically [28]. The pillars and the residual layer are etched in this process, but the lateral and downward etch rates are unequal. However, the ratio between both etch rates is stable, which allows the calculation of the needed residual layer thickness depending on the desired lateral tuning. Ideally, the imprint resist thickness is chosen so that the residual layer is just removed after the tuning process. As we want to maximize the height of the resist pillars to ensure a maximum height of the final stamp, we would rather leave a small residual layer than remove too much material, resulting in a decrease in resist pillar height. Figure 5.1d depicts the sample after tuning.

We use the tuned resist pillars as a mask for an anisotropic RIE step to transfer the pillars into the SiO_2. During the anisotropic RIE process shown in Figure 5.1e, the resist and the SiO_2 are etched simultaneously due to a lack of etching selectivity of the two materials. Therefore, there is an upper limit for the achievable SiO_2 pillar height using this process. The sample is etched until the imprint resist pillars are consumed to maximize the height of the SiO_2 pillars. Nevertheless, we perform a cleaning procedure afterward using a suitable resist remover to ensure the removal of all resist residuals and a clean stamp surface. The final tuned SiO_2 stamp depicted in Figure 5.1f can now act as an original stamp for future NIL processes.

5.1.1 Resist Tuning of the Original 200 nm Stamp

As mentioned, we use the original 200 nm stamp to test our tuning processes, as the fabrication processes with this stamp are less delicate than for the 75 nm stamp; the process parameters are listed in AppendixA.5. Figure 5.2 shows SEM images of the original 200 nm stamp and tuned SiO_2 stamps after 60 s, 90 s, 120 s, and 150 s of tuning with the resist tuning process. The top row of the figure shows SEM overviews of each stamp, and the bottom row shows a zoomed-in SEM on individual stamp pillars.

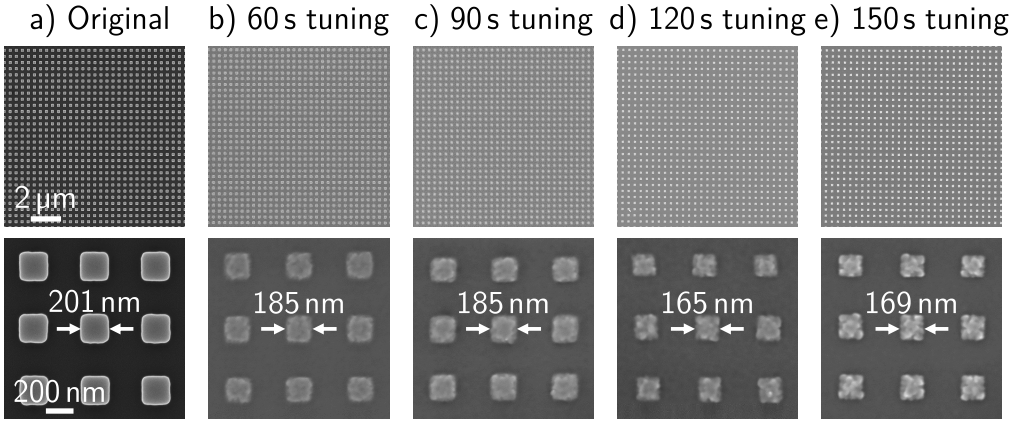

Figure 5.2: SEM images of a) the original 200 nm stamp, b) a SiO_2 stamp after 60 s RIE resist tuning, c) a SiO_2 stamp after 90 s RIE resist tuning, d) a SiO_2 stamp after 120 s RIE resist tuning, and e) a SiO_2 stamp after 150 s RIE resist tuning. The respective top image shows an overview SEM image of each stamp, and the respective bottom image shows a zoom of the structures of each stamp. The side lengths of the square pillars are 200(1) nm, 185(6) nm, 185(8) nm, 165(7) nm, and 169(9) nm for the original stamp and the tuned stamps, respectively.

To evaluate the side length and side length deviation for each stamp's features, we take several SEM images of different positions on each stamp and evaluate the side length of each square pillar in these SEM images. Then, we calculate the mean value and standard deviation from the resulting side lengths, giving us the side length and its deviation for each stamp. In the following, the side length deviation is given in parentheses after the side length values.

Figure 5.2a shows the SEM images of the original 200 nm stamp. The square features of the stamp are periodically arranged in a cubic lattice with a center-to-center distance of 440 nm. The overview image shows no defects in the lattice. The zoomed-in SEM image shows the square features of the stamp with slightly rounded corners. We measure a side length of 201(2) nm, giving the original 200 nm stamp a uniformity of a couple of nanometers between individual features.

Focusing on the overview SEM images of the tuned SiO_2 stamps in Figure 5.2b–e, we see no defects in the nanopillar arrays of the stamps; in particular, no pillars are missing in the array. Therefore, we can state that the

resist tuning process is not introducing systematic defects into the nanopillar arrays.

Turning to the zoomed-in SEM images of the tuned SiO_2 stamps in Figure 5.2b–e, we measure side lengths of 185(6) nm, 185(8) nm, 165(7) nm, and 169(9) nm after tuning times of 60 s, 90 s, 120 s, and 150 s, respectively. The measured side lengths translate to lateral tuning rates of $0.13\,\mathrm{nm\,s^{-1}}$, $0.09\,\mathrm{nm\,s^{-1}}$, $0.15\,\mathrm{nm\,s^{-1}}$, and $0.11\,\mathrm{nm\,s^{-1}}$. These rates are too unstable to predict the final side lengths precisely. Nevertheless, the square shape of the nanopillars is preserved during the tuning process. However, the individual pillars are not as smooth as those of the original stamp. With increasing tuning time, the surfaces and edges of the pillars get rougher. We attribute this behavior to an uneven etching of the imprint resist during the tuning process. Uneven vertical etching leads to a rough surface of the final stamp pillars because a thickness difference in the resist translates to a thickness difference in the silicon oxide during the anisotropic RIE etching step. Similarly, uneven lateral etching leads to rough pillar edges because lateral inhomogeneities are transferred from the resist into the silicon oxide.

Pillar Height Analysis of the Tuned Stamps

To further investigate the differences between the original and the tuned stamps, we took AFM images of the original 200 nm stamp and the resist tuned stamp after 60 s of RIE tuning. Figure 5.3 shows AFM line scans of a pillar of each of the two stamps. In Figure 5.3a, the blue line shows the height profile of a nanopillar of the original 200 nm stamp, and the black dashed line indicates the height of the pillar at 93 nm. The nanopillar of the original stamp has a flat top and almost vertical sidewalls. The side length of the pillar is slightly larger than the above measured 201 nm. This increase originates from the measured convolution of the AFM tip and the nanopillar. We generally use SEM images to evaluate the lateral dimensions of our stamps and samples and AFM images to evaluate their topography.

In Figure 5.3b, the blue line shows the height profile of a nanopillar of a resist tuned stamp after 60 s of RIE tuning. Again, the black dashed line indicates the pillar height of the original 200 nm stamp. However, the tuned stamp's height profile differs from the original stamp's profile. First, with a height of 50 nm, the nanopillar of the tuned stamp is shorter than the nanopillar of the original stamp. Furthermore, the top of the tuned

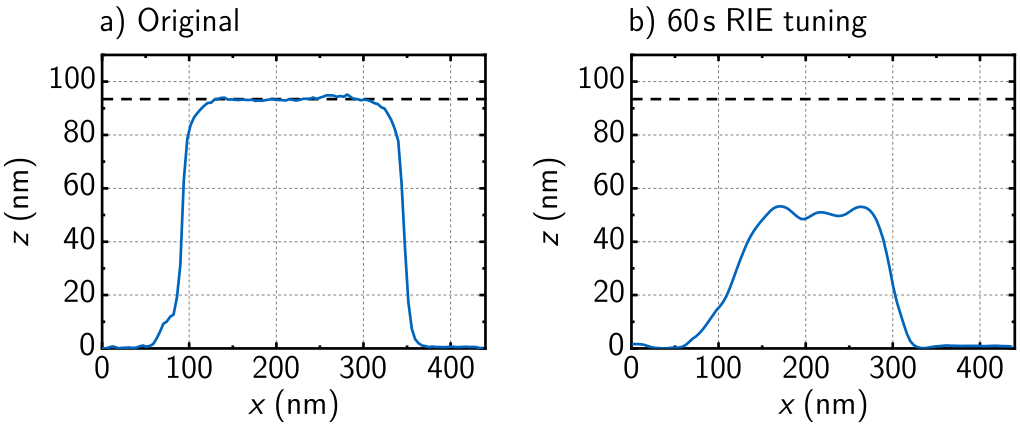

Figure 5.3: AFM height profiles of a) the original 200 nm stamp and b) a SiO_2 stamp after 60 s of tuning with the resist tuning process. The black dashed line indicates the height of the original 200 nm stamp in each graph.

nanopillar is rougher than the top of the original pillar, and the sidewalls are less steep. The smaller height of the tuned pillar can be attributed to a poor etch selectivity of the imprint resist and SiO_2 during the RIE process to transfer the features into the SiO_2. During the process, the imprint resist is etched almost twice as fast as the SiO_2. We already expected a rougher top surface for the tuned stamp, which originated from an uneven etching of the imprint resist during the tuning process, as seen in the SEM images above. The less steep sidewalls are attributed to charging effects of the SiO_2 during its anisotropic dry etching and an uneven lateral etching of the imprint resist during the tuning process. For now, it is hard to distinguish the influences of charging effects and uneven etching during the RIE process. Therefore, we discuss the charging effects in more detail in the subsequent chapters, where their influences can be stated more reliably.

Extended RIE Tuning Times

The overall goal of the feature size tuning is to study the influence of the nanoisland size on light-matter interactions of our metal nanoisland arrays in the visible regime. In simulations, our gold nanoislands show a plasmonic response in the visible light regime for sizes below 100 nm. We need to tune the 200 nm stamps even smaller to achieve such dimensions. Therefore, we

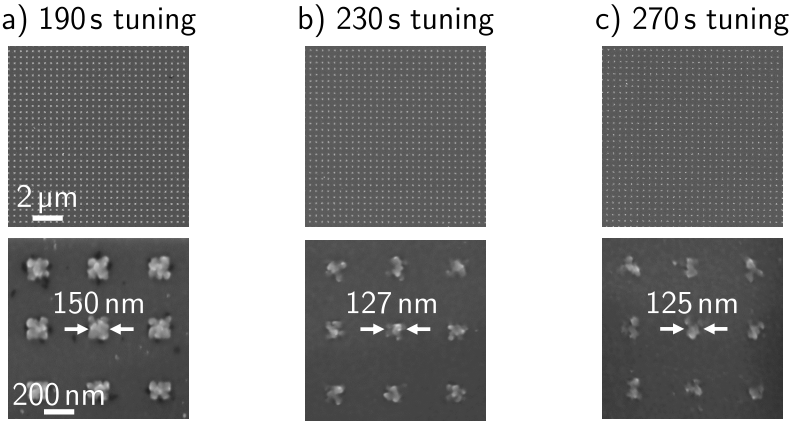

Figure 5.4: SEM images of a) a SiO_2 stamp after 190 s RIE resist tuning, b) a SiO_2 stamp after 230 s RIE resist tuning and, c) a SiO_2 stamp after 270 s RIE resist tuning. The respective top image shows an overview SEM image of each stamp, and the respective bottom image shows a zoom of the structures of each stamp. The side length of the square pillars are 150(11) nm, 124(14) nm, and 125(15) nm for the tuned stamps, respectively.

we fabricated SiO_2 stamps with tuning times of 190 s, 230 s, and 270 s.

SEM images of those stamps are shown in Figure 5.4a–c, respectively. Again, the top row of images shows overviews of the nanopillar arrays of each stamp, and the bottom row shows zoomed-in SEM images of the individual features of the stamps. The overview images again show no defects. Therefore, longer tuning times do not lead to the introduction of missing pillars or systematic defects into the nanopillar arrays. Focusing on the zoomed-in SEM images, we measure side lengths of 150(11) nm, 127(14) nm, and 125(24) nm for the stamps after 190 s, 230 s, and 270 s RIE tuning, respectively. We see an apparent increase in the side length deviation with increasing tuning time. Furthermore, with increasing tuning time, the square shape of the pillars is less and less preserved.

After 270 s of etching in Figure 5.4c, the nanopillars are hardly recognizable as squares. The uneven etching of the imprint resist prohibits the tuning of the 200 nm original stamp down the desired sizes of around 100 nm. Thus, this resist tuning process is not suitable for our goals. Therefore, we must advance the process for a more reliable tuning of the SiO_2 stamps. We shift the tuning from the resist pillars to the SiO_2 pillars for the new tuning

process. Compared to the imprint resist, the SiO_2 oxide can be reliably and isotropically etched using HF based solutions.

5.2 The Resist HF Tuning Process

In the previous section, we introduced the resist tuning process to tune the dimensions of our imprinting stamps. However, the process fell short of our needs as we could not reliably tune the stamp feature sizes to the desired side lengths of about 100 nm. The main reason for the unreliable tuning is the uneven etching of the imprint resist during the tuning step of the process. To overcome this problem, we shift the tuning part of the process from the imprint resist into the SiO_2. For that, we first reproduce the original imprinting stamp using the imprint resist as an etching mask and then tune the features of this reproduced stamp. Diluted and buffered HF solution enables a slow and controlled isotropic etching of SiO_2, which allows us to precisely tune the dimensions of the features of the reproduced stamps.

The new process is schematically depicted in Figure 5.5. Equal to the previous, the silicon substrate with a layer of SiO_2 on top is cleaned in each DMSO, acetone, and isopropanol using an ultrasonic bath. Figure 5.5a shows the clean substrate. Again, we apply a layer of imprint resist to the substrate via spin coating. In Figure 5.5b, the sample is depicted after spin coating and before the imprinting step. We use an inverted stamp to create pillars of imprint resist on top of the SiO_2 layer during the imprinting process. As the imprint resist pillars are not tuned this time, we adjust the thickness of the imprint resist to produce an as thin as possible residual layer. The final pillars and the residual layer are shown in the inset of Figure 5.5c.

From this point onwards, the new resist HF tuning process differs significantly from the previous resist tuning process. Rather than isotropically shrinking the imprint resist pillars, we transfer the features directly into the SiO_2. For that, we use the same anisotropic dry etching process as before. To maximize the height of the SiO_2 pillars, we aim for an etching time where the imprint resist is just etched away. Figure 5.5d shows the sample during the etching process. After etching, the nanopillars are transferred from the resist into the SiO_2. To remove all residuals of the imprint resist, we clean the sample again in each DMSO, Acetone, and Isopropanol using an ultrasonic bath. The clean reproduced stamp is depicted in Figure 5.5e. Now,

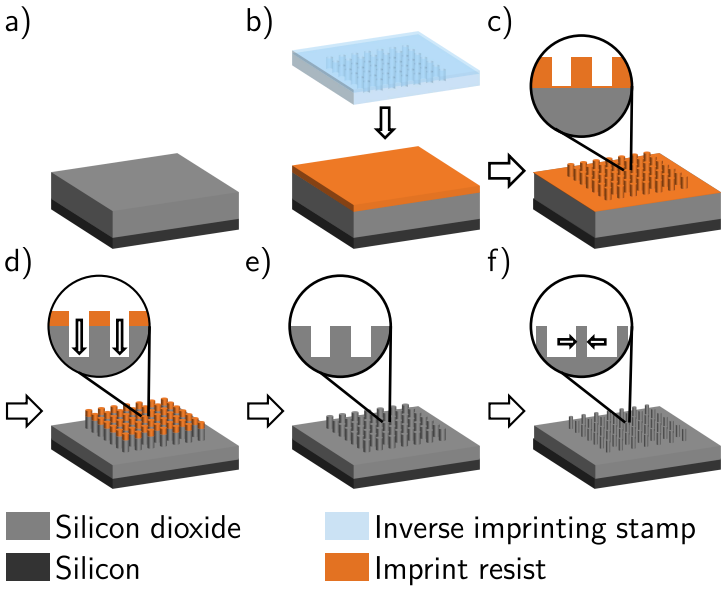

Figure 5.5: Schematic depiction of an imprinting stamp replication and tuning processes using resist nanopillars as a dry etching mask for an anisotropic RIE process and subsequent HF tuning. a) The silicon/chSiO2 substrate is cleaned in each DMSO, Acentone, and Isopropanol using an ultrasonic bath. b) The imprint resist (orange) is spin coated onto the SiO_2 surface before the inverse imprinting stamp is applied to the sample. c) The imprinting process produces cylindrical resist nanopillars. Also, the process leaves an inevitable residual layer on the substrate surface. d) Using the resist nanopillars as an etching mask, the pillars are transferred into the SiO_2 via an anisotropic dry etching step. e) After the transfer, the remaining imprint resist is removed. f) The diameter of the SiO_2 nanopillars are tuned via an isotropic wet etching step in an HF based solution.

we use a diluted and buffered HF solution to isotropically shrink the SiO_2 nanopillars in a controlled and reliable way. Figure 5.5f shows the final tuned SiO_2 stamp, which can now be used as a new original stamp for all our NIL processes.

5.2.1 Resist HF Tuning of 200 nm Stamps

Once more, we test the new resist HF tuning process on the original 200 nm stamp; the process parameters are listed in AppendixA.5. First, we want to investigate what etching times and performance we can achieve with the new method and if the new method solves the problems we had using the previous resist tuning process. Figure 5.6 shows SEM images of original 200 nm stamp, a reproduced SiO_2 stamp and SiO_2 stamps after 20 s, 60 s, and 100 s of HF tuning. Again, the top row shows an overview of the nanopillar array of each stamp, whereas the bottom row shows a zoom onto individual nanopillars. The original 200 nm stamp is the same as before. We can see the same defect-free array of nanopillars in Figure 5.6a and measure a side length of 201(2) nm.

Next, Figure 5.6b shows an overview and a zoomed-in SEM image of the reproduced SiO_2 stamp without any tuning. Again, we see no introduced systematic defects or missing nanopillars in the overview SEM image. Thus, using the imprint resist as an etching mask, the reproduction process creates no defects in the nanopillar array. However, we measure a side length of 230(8) nm for nanopillars of the reproduced stamp, which is significantly larger than the 201(2) nm of the original stamp. We attribute this increase to charging effects during dry etching of the SiO_2. As the insulating SiO_2 prevents a charge flow from the imprint resist to the substrate, charges accumulate in the imprint resist during the RIE process. As a result, the arising electrical fields deflect further incoming ions, and the effective area of the resist mask increases. Although we did not expect such a significant side length increase, it allows us to increase the feature sizes with the reproduction process. However, the bigger feature sizes increase the stamps' tuning times as the tuning process's starting point is shifted to higher side lengths.

Besides the increase in size, the deviation between the individual islands of the reproduced stamp increases. Thus, the overall uniformity of the reproduced stamps is decreased during the reproduction step. Additionally, the roughness of the surface of the nanopillar is increased after reproduction. We attribute the increase in side length deviation and surface roughness to an uneven etching of the imprint resist during the reproduction step. In the previous section, we also observed the tendency toward uneven etching of the imprint resist. Nevertheless, the square shape of the nanopillars is well preserved during the reproduction step.

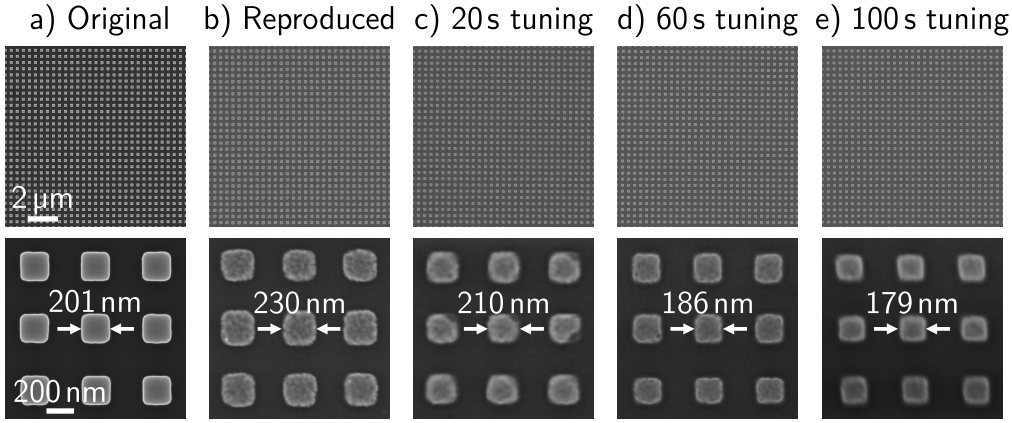

Figure 5.6: SEM images of a) the original 200 nm stamp, b) a reproduced SiO_2 stamp, c) a SiO_2 stamp after 20 s HF tuning, d) a SiO_2 stamp after 60 s HF tuning, and e) a SiO_2 stamp after 100 s HF tuning. The respective top image shows an overview SEM image of each stamp, and the respective bottom image shows a zoom of the structures of each stamp. The side lengths of the square pillars are 200(1) nm, 232(9) nm, 212(2) nm, 184(10) nm, and 176(9) nm for the original stamp, the reproduced stamp and the tuned stamps, respectively.

Focusing on the resist HF tuned stamps in Figure 5.6c–e, we can see no defects or missing nanopillars in the overview SEM images. Therefore, the HF tuning process of the SiO_2 nanopillars does not introduce systematic defects or missing pillars. For the side lengths of the tuned stamps, we measure 210(5) nm, 186(7) nm, and 179(7) nm for the HF tuning times of 20 s, 60 s, and 100 s, respectively. The side lengths of the nanopillars decrease with increasing tuning time. Hence, the HF tuning of the SiO_2 is successful. The tuning also preserves the square features of the nanopillars. The deviation of the side lengths of the tuned nanopillars is similar for all tuned SiO_2 stamps and comparable to the deviation of the reproduced SiO_2 stamp. Furthermore, the roughness of the nanopillar surface is similar after the tuning compared to the reproduced stamp. The constant side length deviation and surface roughness indicate a very isotropic etching process of the SiO_2 nanopillars in the HF solution.

The defective islands of the SiO_2 stamp after 60 s of tuning are not caused by the tuning process but stem from defects in the imprint resist pillars before the reproduction process. Despite those defects, the stamp was used

to test the process's feasibility and did not influence the tuning process.

Using the side length of the reproduced stamp as a starting point, we calculate lateral etch rates of $0.5\,\mathrm{nm\,s^{-1}}$, $0.37\,\mathrm{nm\,s^{-1}}$, and $0.26\,\mathrm{nm\,s^{-1}}$ for HF tuning times of 20 s, 60 s, and 100 s, respectively. The etch rate decreases significantly with increasing tuning time. We assume that the dry etching process during the reproduction step leaves a structurally altered or damaged SiO_2 on the surface of the nanopillars. This less stable layer is etched at a higher etch rate as the undamaged SiO_2 underneath. Thus, the lateral tuning rate is high initially and slows down when the damaged SiO_2 is removed. Therefore, we expect a saturation of the lateral tuning rates for even higher tuning times.

Pillar Height Analysis of the Tuned Stamps

To further investigate the resist HF tuning process, we again use AFM measurements to compare the topography of the original stamp with a resist HF tuned stamp in Figure 5.7. In Figure 5.7a, the blue line shows the AFM height profile of the original 200 nm stamp, and the black dashed line indicates its height at 93 nm. As seen before, the nanopillar has almost vertical sidewalls and low surface roughness.

In comparison, in Figure 5.7b, the blue line shows the AFM profile of the tuned stamp after 100 s of HF tuning. Again, the dashed line indicates the height of the original 200 nm stamp. The height of the tuned stamp of 50 nm is significantly smaller than the height of the original stamp. However, the height is the same as the height of the nanopillar tuned with the resist tuning process in Figure 5.3b, which makes sense as the imprint resist is used as a mask for the dry etching of the SiO_2 for both processes. Thus, the difference in height between the original and tuned stamp can be attributed to the poor selectivity between the imprint resist and the SiO_2 during dry etching.

Besides the shorter height of the nanopillar, the resist HF tuned stamp shows higher surface roughness than the original stamp. Furthermore, the sidewalls of the tuned stamp are not as vertical as the sidewalls of the original stamp. However, compared to the resist tuned stamp of the previous section in Figure 5.3b, the resist HF tuned stamp in Figure 5.7b has a smaller surface roughness and steeper sidewalls. Thus, the shift of the tuning process from the imprint resist to the SiO_2 makes the whole tuning process smoother and more reliable.

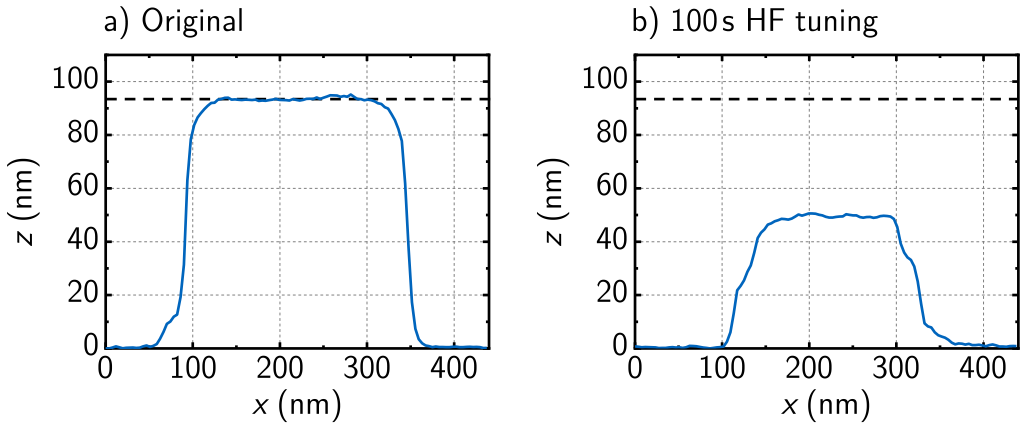

Figure 5.7: AFM height profiles of a) the original 200 nm stamp and b) a SiO_2 stamp after 100 s of HF tuning with the resist HF tuning process. The black dashed line indicates the height of the original 200 nm stamp in each graph.

Extended HF Tuning Times

Without the problem of uneven tuning, we expect to reach smaller feature sizes using the resist HF tuning process. To test this assumption, we fabricated additional tuned SiO_2 stamps with longer HF tuning times. Figure 5.8 shows SEM images of resist HF tuned SiO_2 stamps after 230 s, 285 s, 340 s, 400 s, and 455 s of HF tuning. The top row of images again shows an overview SEM image of the nanopillar array of each stamp, and the bottom row shows zoomed-in SEM images of the features of each stamp. Again, all overview images show no defects or missing nanopillars. Therefore, further tuning of the SiO_2 nanopillars does not influence the reliability of the resist HF tuning process.

Focusing on the zoomed-in SEM images, the square shape of the pillars is still preserved even with the longer tuning times. We measure side lengths of 139(4) nm, 128(5) nm, 114(4) nm, 91(4) nm, and 93(4) nm for the tuned SiO_2 stamps after tuning times of 230 s, 285 s, 340 s, 400 s, and 455 s, respectively. Using the side length of 230(8) nm of the reproduced stamp in Figure 5.6b as the reference point, we calculate respective lateral tuning rates of 0.20 nm s^{-1}, 0.18 nm s^{-1}, 0.17 nm s^{-1}, 0.17 nm s^{-1}, and 0.15 nm s^{-1} for the five stamps. Analyzing these tuning rates, we observe the predicted stabilization of the rates as the influence of the higher initial rate decreases with increasing

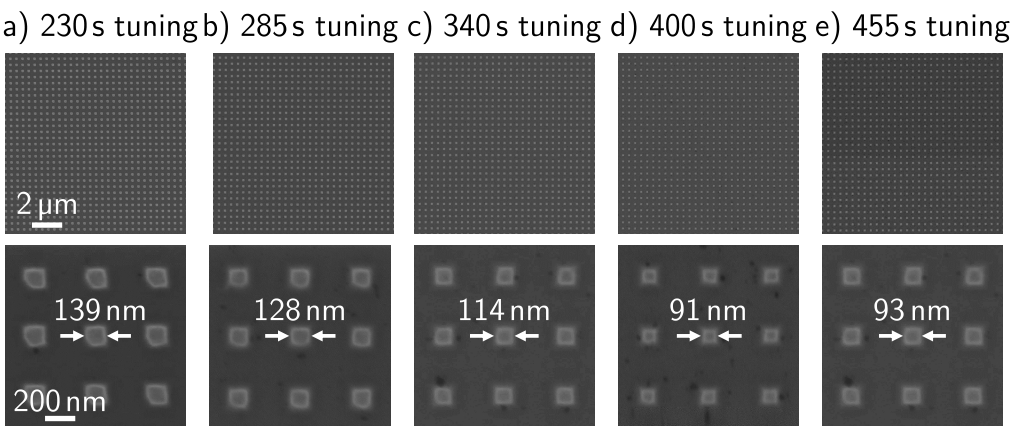

Figure 5.8: SEM images of a) a SiO_2 stamp after 230 s HF tuning, b) a SiO_2 stamp after 285 s HF tuning, c) a SiO_2 stamp after 340 s HF tuning, d) a SiO_2 stamp after 400 s HF tuning, and e) a SiO_2 stamp after 455 s HF tuning. The respective top image shows an overview SEM image of each stamp, and the respective bottom image shows a zoom of the structures of each stamp. The side length of the square pillars are 139(4) nm, 128(5) nm, 144(4) nm, 91(4) nm, and 93(4) nm for the tuned stamps, respectively.

tuning times.

With the new resist HF tuning process, we can reach feature sizes below 100 nm side length, which are needed for plasmonic applications in the visible light regime. Furthermore, the shift of the tuning process into the SiO_2 enables a smooth tuning even for longer tuning times, and the shape of the nanopillars is preserved during the whole process.

Fabrication of Nanoisland Arrays

Now that we found a stamp tuning method that allows the tuning of the original 200 nm stamp down to side lengths of around 100 nm, we want to fabricate metal nanoisland arrays with the tuned SiO_2 stamps. For that, we first perform our working stamp fabrication process described in Section 2.1.2 using the tuned stamps from Figure 5.8 as new original stamps. Next, we use these working stamps to perform our standard LO-NIL process described in Section 2.2.1 to fabricate gold nanoislands on a silicon substrate.

Figure 5.9 shows SEM images of the gold nanoisland arrays fabricated with

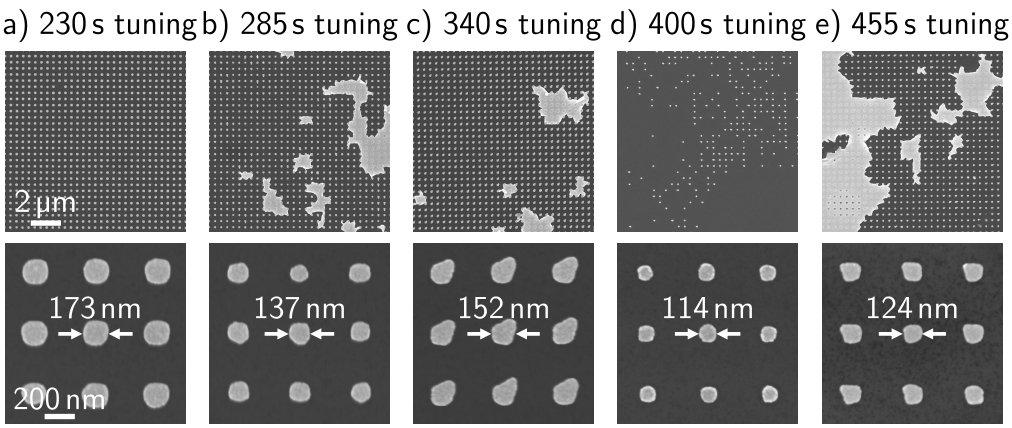

Figure 5.9: SEM images of gold nanoisland arrays fabricated with a) a SiO_2 stamp after 230 s HF tuning, b) a SiO_2 stamp after 285 s HF tuning, c) a SiO_2 stamp after 340 s HF tuning, d) a SiO_2 stamp after 400 s HF tuning, and e) a SiO_2 stamp after 455 s HF tuning. The top row shows an overview SEM image of each sample, and the bottom row shows a zoom onto the structures of each gold nanoisland array. The diameter of the gold nanoislands are 173(8) nm, 137(6) nm, 152(7) nm, 114(7) nm, and 124(5) nm for the tuned stamps, respectively.

the resist HF tuned stamps with HF tuning times of 230 s, 285 s, 340 s, 400 s, and 455 s. The top row of SEM images shows an overview of the nanoisland arrays, and the bottom row shows a zoomed-in SEM image of the individual nanoislands. The overview and zoom-in have the same magnification as their respective images of the tuned stamps in Figure 5.8.

Despite the defect-free tuned SiO_2 stamps, defects are visible in every overview images of the nanoisland arrays. The array fabricated with the stamp after 230 s of HF tuning in Figure 5.9a looks the most promising as we can only identify one missing island. However, the overview images in Figure 5.9b, 5.9c, and 5.9e show large arrays where the gold was not lifted off properly and in the overview image in Figure 5.9d more than 50 % of the nanoislands are missing.

Section 2.2.3 discussed common defects of nanoisland arrays of LO-NIL samples and their origins. There we discussed that a failed lift-off indicates a too-small imprint resist layer height due to too long residual layer etching. At the same time, missing islands indicate a too-short residual layer etching or too-short development of the lift-off resist. As the development is the

Table 5.2: Diameter comparison of stamp pillars and nanoislands for the resist HF tuning of the original 200 nm stamp

Tuning time	Stamp pillars	Nanoislands	Difference
230 s	139(4) nm	173(8) nm	34 nm
285 s	128(5) nm	137(6) nm	9 nm
340 s	114(4) nm	152(7) nm	38 nm
400 s	91(4) nm	114(7) nm	23 nm
455 s	93(4) nm	124(5) nm	31 nm

same for all nanoisland arrays in Figure 5.9, the problems most likely occur due to too long or too short residual layer etching. In Figure 5.9e, we can see that besides the large areas of not lift-off gold, one of the nanoislands in the lower right corner is also missing. As those defects originate from opposite causes, particularly too long or too short residual layer etching, we conclude there is no perfect etching time to prevent defects.

We attribute the defective samples to the shorter height of the nanopillars of the tuned stamps. In Figure 5.7, we saw that the height of the tuned stamps is just 50 nm compared to the height of the original 200 nm stamp of 93 nm. Thus, during the LO-NIL process, the imprint resist is only about half as thick as in our standard process. The reduced thickness cannot be compensated with shorter etching times, and therefore either a failed lift-off or missing nanoislands occur on the final samples.

The smaller pillar height of the tuned stamps also causes issues for the remaining nanoislands on the substrate. We measure side lengths of 173(8) nm, 137(6) nm, 152(7) nm, 114(7) nm, and 124(5) nm for the gold nanoisland arrays fabricated with the resist HF tuned stamps after HF tuning of 230 s, 285 s, 340 s, 400 s, and 455 s, respectively. The side lengths of the gold nanoisland arrays are compared with those of the respective tuned stamps in Table 5.2. The first and second column of the table shows the side lengths and their deviations for the features of the tuned stamp and their respective nanoisland array, respectively. The third column shows the side length difference between the stamp features and the nanoisland array. The side lengths of the stamp and sample differ significantly by tens of nanometers. However, in Section 2.2.1, we saw that our standard LO-NIL process has a

precision within a few nanometers.

Furthermore, the square shape of the nanopillars is not preserved for the gold nanoislands shown in Figure 5.9. On the other hand, the standard LO-NIL process is highly reliable in preserving the feature shapes from the stamp to the sample. Therefore, we attribute the poor quality of the gold nanoisland shapes to differences between our standard stamps and the tuned stamps. In particular, the reduced height of the imprint resist in the process influences the development and etching times, which leads to a poor result.

Therefore, the resist HF tuning process solves the problem of the uneven shrinkage of the nanopillars during the tuning process. However, we can still not use the tuned stamps to fabricate gold nanoisland arrays in the desired dimensions.

5.2.2 Resist HF Tuning of 350 nm Stamps

To confirm that the lower height of the nanopillars of the tuned stamps is the reason for the poor quality of the gold nanoisland arrays, we test the resist HF tuning process with the original 350 nm stamp; the process parameters are listed in AppendixA.5. Its height of 260 nm enables us to produce tuned stamps with higher features with an expected height of 130 nm. Figure 5.10 shows SEM images of the original 350 nm stamp and resist HF tuned SiO_2 stamps after 450 s, 500 s, 550 s, and 600 s of HF tuning. Again, the top row of SEM images shows an overview of the nanopillar arrays, and the bottom shows zoomed-in images of the individual nanopillars of each stamp.

The overview SEM image of the original 350 nm stamp in Figure 5.10a shows no defects or missing nanopillars. The nanopillars of the original stamp are periodically arranged in a cubic lattice and have a center-to-center distance of 700 nm. We see a white frame around the nanopillars in the zoomed-in SEM image of Figure 5.10a. The white frame arises from the not-vertical sidewalls of the stamp pillars discussed in Section 2.1.1. When we measure the side length of the stamp, we are not considering this frame in our calculations. For the original 350 nm stamp we measure a side length of 357(4) nm.

Now focusing on the tuned SiO_2 stamps, the overview SEM images show no defects or missing nanopillars, which confirms the reproducibility of the resist HF tuning process. The zoomed-in SEM images of Figure 5.10b–d show that the square shape of the nanopillars is preserved even for the high tuning

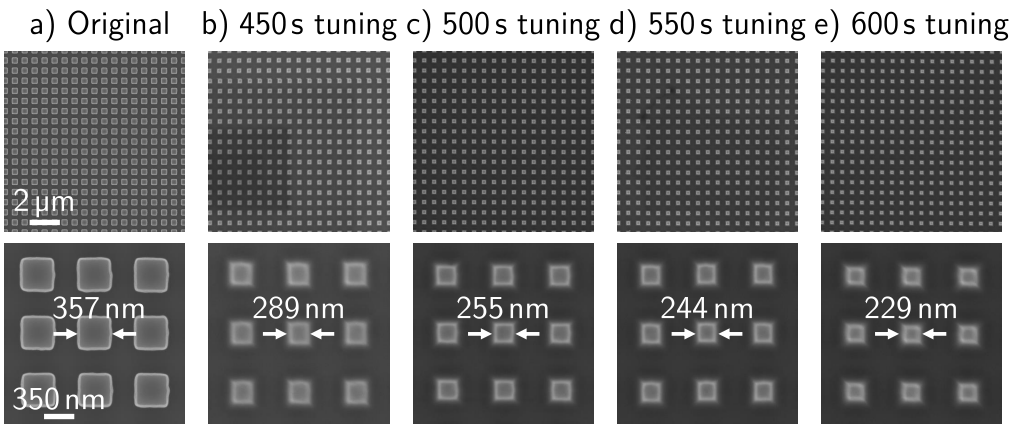

Figure 5.10: SEM images of a) the original 350 nm stamp, b) a SiO_2 stamp after 450 s HF tuning, c) a SiO_2 stamp after 500 s HF tuning, d) a SiO_2 stamp after 550 s HF tuning, and e) a SiO_2 stamp after 600 s HF tuning. The respective top image shows an overview SEM image of each stamp, and the respective bottom image shows a zoom of the structures of each stamp. The side lengths of the square pillars are 350(1) nm, 289(16) nm, 255(9) nm, 244(14) nm, and 229(10) nm for the original stamp and the tuned stamps, respectively.

times of up to 10 min. The high stability of the tuning process confirms the isotropic etching of SiO_2 with diluted HF solution as a suitable tuning process for our purposes. Before tuning, we measure side lengths of 467(7) nm for a reproduced 350 nm stamp. Thus, we experience the familiar side length increase during the reproduction process. After tuning, we measure side lengths of 289(16) nm, 255(9) nm, 244(14) nm, and 229(10) nm for the tuned stamps after 450 s, 500 s, 550 s, and 600 s of HF tuning, respectively. With the side length of the reproduced stamp as starting point, we calculate respective lateral tuning rates 0.19 nm s^{-1}, 0.21 nm s^{-1}, 0.20 nm s^{-1}, and 0.19 nm s^{-1} for the tuned 350 nm stamps.

Concentrating on the measured side lengths of the tuned SiO_2 stamps, the deviation of the side lengths is increased for the tuned 350 nm stamps compared to the tuned 200 nm stamps in Figure 5.6. We attribute the increase in the side length deviation and, therefore, a decrease in uniformity to the decreased uniformity of the original 350 nm. The lateral tuning rates are comparable to the rates measured for the tuned 200 nm stamps. Thus, the tuning rate is not dependent on the initial feature size of the stamps.

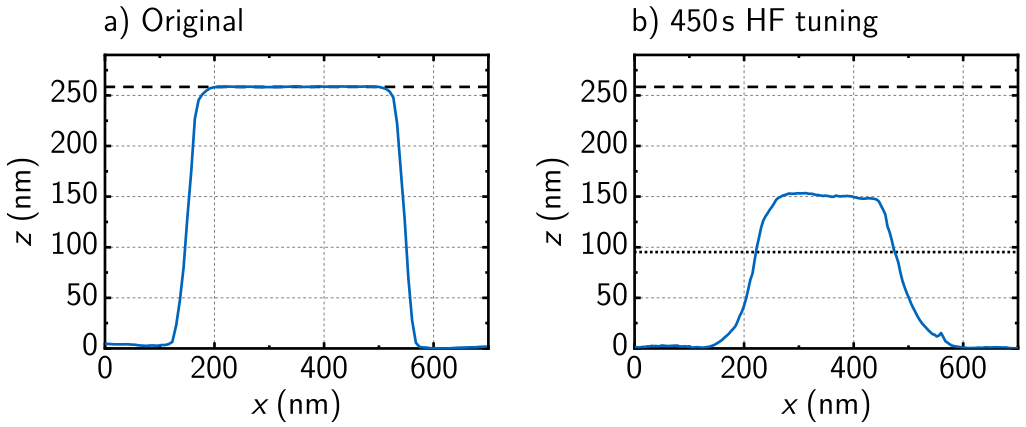

Figure 5.11: AFM height profiles of a) the original 350 nm stamp and b) a SiO_2 stamp after 450 s of HF tuning with the resist HF tuning process. The black dashed line indicates the height of the original 350 nm stamp in each graph, and the black dotted line in b) indicates the height of the original 200 nm stamp.

Pillar Height Analysis of the Tuned Stamps

We took AFM images to analyze the topography and confirm a sufficient height of the pillars of the tuned 350 nm stamps. Figure 5.11 shows AFM height profiles of the original 350 nm stamp and the SiO_2 stamp after 450 s of HF tuning. In Figure 5.11a, the blue line shows the height profile of a nanopillar of the original 350 nm stamp. Additionally, the black dashed line indicates the height of the nanopillar at 260 nm. The top of the nanopillar has a width of around 350 nm. However, the sidewalls of the nanopillar are not vertical, which leads to an increase in width going down the pillar. The increase in width explains the white frame in the SEM images.

In Figure 5.11b, the blue line shows the height profile of the tuned 350 nm stamp after 450 s of Hf tuning. Additionally, the black dashed line indicates the height of the original 350 nm stamp of 260 nm, and the black dotted line indicates the height of the original 200 nm stamp at 93 nm. With a height of 150 nm, the nanopillar of the tuned stamp is significantly smaller than the nanopillar of the original 350 nm stamp. This height difference can again be attributed to the poor selectivity of the imprint resist and the SiO_2 during the reproduction step of the resist HF tuning process. However, the 150 nm exceed the height of the original 200 nm stamp of 93 nm. Therefore, the

height of the nanopillars of the tuned 350 nm stamps should not be sufficient for the fabrication of gold nanoisland arrays using our standard LO-NIL process.

Fabrication of Nanoisland Arrays

With the height constraints arguably solved for the tuned 20 nm stamps, we fabricated nanoisland arrays from those stamps and evaluated the samples via SEM images; the process parameters are listed in AppendixA.5. Figure 5.12 shows SEM images of gold nanoisland arrays fabricated with the original 350 nm stamp and its tuned stamps after 450 s, 500 s, 550 s, and 600 s of HF tuning. The top row of SEM images shows an overview of the gold nanoisland arrays of the samples, and the bottom row shows zoomed-in SEM images of the gold nanoislands of each sample.

In the overview image of Figure 5.12a, the nanoisland array of the sample fabricated with the original 350 nm stamp has no defects or missing islands. The zoomed-in SEM image shows square gold nanoislands. We measure a side length of 390(7) nm for the gold nanoislands fabricated with the original stamp. We would not expect such a significant increase in side length from the stamp to the sample to be caused by the LO-NIL process. However, we saw before that the original 350 nm stamp nanopillars have no vertical but slightly angled sidewalls causing the increased side lengths. Section 2.2.1 discusses the origin of the side length increase in more detail.

Now focusing on the gold nanoisland arrays fabricated with the tuned stamps, the overview SEM images in Figure 5.12b–e show no defects or missing nanoislands. The problems with missing nanoislands or bad lift-off we had with the tuned 200 nm stamps are not occurring when using the tuned 350 nm stamps. Therefore, the higher nanopillars of the tuned 350 nm stamps allow a smooth LO-NIL process and solve the issues we had with the tuned 200 nm stamps.

However, when we look at the zoomed-in images in Figure 5.12b–e, we see that the shapes of the gold nanoislands are not square for three of the four samples. All nanoislands of the defective samples are deformed in one direction. We already saw this kind of systematic defect in Section 2.2.3, where we discussed common defects of the LO-NIL process. There, we attributed the defect to the deformation of the imprint resist during the mechanical working stamp removal, worsened by an expired imprint resist. As the sys-

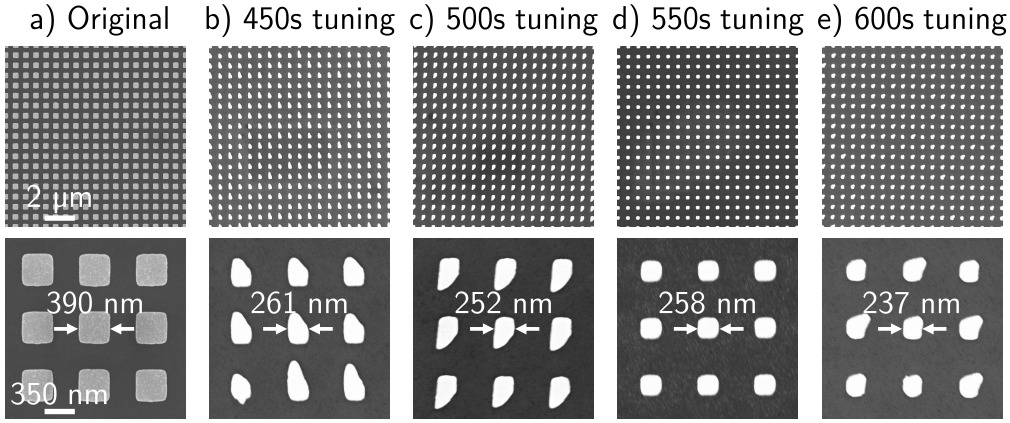

Figure 5.12: SEM images of gold nanoisland arrays fabricated with a) the original 350 nm stamp, b) a SiO_2 stamp after 450 s HF tuning, c) a SiO_2 stamp after 500 s HF tuning, d) a SiO_2 stamp after 550 s HF tuning, and e) a SiO_2 stamp after 600 s HF tuning. The top row shows an overview SEM image of each sample, and the bottom row shows a zoom onto the structures of each gold nanoisland array. The diameter of the gold nanoislands are 350(8) nm, 259(24) nm, 267(8) nm, 251(9) nm, and 271(14) nm for the tuned stamps, respectively.

tematic deformation is not dependent on the stamp used during the LO-NIL process, we can neglect it to evaluate the resist HF tuning process using the 350 nm stamps. However, we must account for the islands' deformation influencing the measured side lengths of the nanoislands. To minimize the influence of the deformation on the measured side lengths, we measure the side length of deformed nanoislands only in the not-deformed directions.

For the gold nanoislands fabricated with the stamps after 450 s, 500 s, 550 s, and 600 s of HF tuning, we measure a side length of 271(14) nm, 252(4) nm, 258(7) nm, and 237(4) nm, respectively. Table 5.3 shows the side lengths of the tuned 350 nm stamps, their respective samples, and the difference in side length between stamp and sample. We already discussed the origin of the significant difference in the side lengths of the original 350 nm stamp and its respective nanoisland array. For the tuned stamps, we expect smaller differences. Indeed, all side length differences between the tuned stamps and their samples are smaller than the difference between the original stamp and its sample. However, for the first two tuned stamps after 450 s and 500 s of tuning, the side lengths of the samples are smaller compared to their stamps,

Table 5.3: Diameter comparison of stamp pillars and nanoislands for the resist HF tuning of the original 350 nm stamp

Tuning time	Stamp pillars	Nanoislands	Difference
reproduced	357(4) nm	390(7) nm	33 nm
450 s	289(16) nm	271(14) nm	18 nm
500 s	255(9) nm	252(4) nm	3 nm
550 s	244(14) nm	258(7) nm	14 nm
600 s	229(10) nm	237(4) nm	8 nm

whereas for the second two tuned stamps after 550 s and 600 s the side lengths of the samples are larger compared to their stamps. As the side length differences vary in sign, we cannot attribute them to a systematic increase or decrease due to the use of the tuned SiO_2 stamps, as in this case, the sign of the side length difference would be the same for all stamps. We rather assume a combination of a possible systematic influence of the tuned stamps and an influence of the deformations caused by the expired imprint resist. Thus, making a quantitative statement about the influence of the tuned SiO_2 stamps on the side lengths of the gold nanoisland arrays fabricated with our LO-NIL process is difficult. However, we solved the issues of missing nanoislands or poor lift-off by increasing the height of the nanopillars of the tuned SiO_2 stamps.

The goal is still to have size-tunable features to perform plasmonic experiments in the visible light regime. Therefore, we need to tune the size of the nanoislands below 100 nm. Using the original 350 nm stamp as the starting point for the tuning, reliably reaching nanopillar side lengths below 100 nm is unrealistic. Due to the long etching times needed for the tuning, minor deviations during tuning would lead to significant deviations in the resulting stamps. Furthermore, with a pitch of 700 nm of the original 350 nm stamp, we would waste much space on the sample by tuning the stamp features below 100 nm. To reliably and effectively fabricate nanoisland arrays for our experiments, we have to find a method to tune the original 200 nm and 75 nm stamps. Therefore, we must improve the selectivity of our etching mask and SiO_2 to achieve larger heights of the nanopillars of the tuned stamps.

5.3 The Chromium HF Tuning Process

We no longer use the imprint resist as etching the mask to achieve a higher selectivity for the etching of SiO_2. Instead, we developed a reproduction and tuning method using a chromium hard mask instead of the imprint resist for the RIE process during reproduction. The chromium hard mask is fabricated using the standard LO-NIL process. After reproducing the stamp, the tuning process is equal to the process used in the resist HF tuning process using an HF-based solution. The new chromium HF tuning process and subsequent application are already published in [55] and republished in this chapter's remaining sections. The Figures are updated to fit the format of this work and reprinted with permission. The text is updated to fit the format of this thesis, and information from the supplementary material is included.

The chromium HF tuning method is schematically depicted in Figure 5.13. We start by fabricating the chromium hard mask using our LO-NIL process. For completeness of this section, the LO-NIL process is again explained as part of the chromium HF tuning method. For our standard double resist layer NIL process, we first spin coat a lift-off resist and an imprint resist on the silicon-SiO_2 substrate. Figure 5.13a shows the substrate after spin coating of the two resists.

Next, we apply a working stamp with the desired features onto the sample and transfer the stamp-sample stack into the imprinter. In the imprinter, the sample is heated above the imprint resists glass transition temperature. In the process, the thermo-viscous imprint resist becomes viscous. Now, the working stamp is pressed into the imprint resist. During this process, the imprint resist fills the features of the working stamp. As a result, the stamp features are transferred into the imprint resist. Before the demolding of the stamp, the sample is cooled to room temperature to harden the imprint resist. Then, the working stamp is mechanically removed from the imprint resist. Figure 5.13b illustrates the sample after the imprinting process; here, the inset shows a cross section through the sample.

Now, an inverted pattern of the working stamp is apparent in the imprint resist. However, the stamp always leaves a so-called residual layer in the imprint resist, a thin layer of resist on top of the underlying resist or substrate. The arrow indicates the residual layer in the inset of Figure 5.13b. The residual layer must be removed in a RIE step to expose the lift-off resist for further processing. The inset in Figure 5.13c shows the sample after remov-

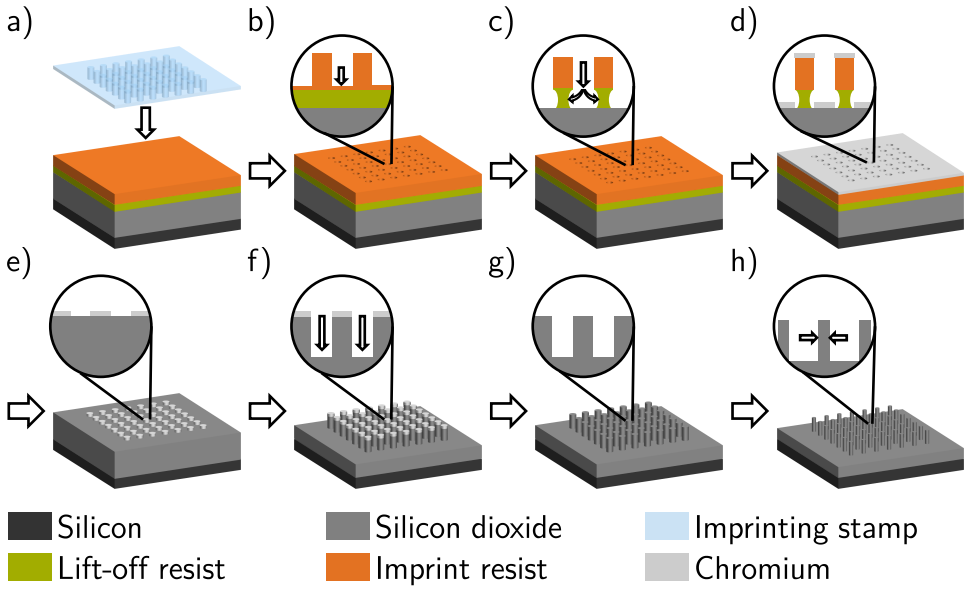

Figure 5.13: Schematic depiction of the imprinting stamp replication and tuning process consisting of the three process phases: a)-e) double resist LO-NIL of chromium nanoislands, e)-g) dry etching to form a SiO_2 replica stamp, and g)-h) HF tuning of the stamp features: a) The lift-off resist (green) and the imprint resist (orange) are spin coated onto the SiO_2 surface before the imprinting stamp is applied to the sample. b) The actual imprinting process transfers the features of the imprinting stamp into the imprint resist. The inset shows the inevitable residual layer of the imprint resist. c) The residual layer is removed via an anisotropic dry etching step, followed by an isotropic wet etching step of the lift-off resist to expose the SiO_2 surface and to create an artificial undercut. d) Subsequently, chromium is evaporated onto the sample. e) After lift-off, the chromium nano island array remains on the SiO_2 surface. f) In the following dry etching step, the chromium nanoislands are used as a hard mask to form pillars in the SiO_2 layer. g) The chromium discs are removed. h) The size of the pillars of the SiO_2 replica stamp are isotropically tuned in an HF acid-based solution. Reprinted with permission from [55].

ing the residual layer, and the following developing step of the lift-off resist. We isotropically etch the exposed lift-off resist in a wet chemical development process. We hereby expose the SiO_2 surface for later metal evaporation and create an artificial undercut in the lift-off resist. This undercut ensures

a smooth metal lift-off after evaporation.

In the next step, we evaporate chromium onto the sample. Figure 5.13d depicts the sample after the evaporation step. The artificial undercut prevents the deposition of chromium on the sidewalls of the lift-off resist, as seen in the inset of Figure 5.13d. Therefore, no metal bridges can form between the chromium on the SiO_2 surface and the chromium on top of the imprint resist. Hence, a smooth lift-off of the resists and the chromium on top is guaranteed.

In a subsequent lift-off step, we remove the excess chromium on top of the resists together with both resists. Figure 5.13e shows the sample after the lift-off process. The chromium nanoislands on top of the SiO_2 surface have the same diameters as the pillars of the original stamp and are inert to RIE gases used to etch SiO_2. Therefore, they are now used as a hard mask for an anisotropic RIE process to form pillars in the SiO_2 and reproduce the pattern of the original imprinting stamp, as depicted in Figure 5.13f.

Subsequently, the chromium is selectively removed from the top of the pillars using chromium etchant. Figure 5.13g shows the SiO_2 reproduced stamp after the chromium removal. This reproduced stamp can be handled like the original for all our NIL processes.

As seen before, The advantage of SiO_2 as the stamp material of the reproduced stamp compared to the original silicon stamp is that it can be isotropically etched by an HF based solution in a controlled way. A slow etch rate of $0.2\,\mathrm{nm\,s^{-1}}$ allows us to control the size of the tuned pillars precisely and guarantees the conservation of the pillar's shape during the tuning process. Thus, we can tune the diameter of the SiO_2 pillars without influencing their form. Therefore, the final dimensions of the pillars solely depend on the etching time in the HF solution. The final tuned SiO_2 stamp is illustrated in Figure 5.13h. Finally, we can use the tuned stamp for all our imprinting processes, similarly to the original stamp.

5.3.1 Chromium HF Tuning of 200 nm Stamp

Previously, we could not fabricate metal nanoisland arrays from resist HF tuned 200 nm stamps due to the height constraints of the stamps. Therefore, we first use the new chromium HF tuning method to tune the original 200 nm stamp to analyze whether the new method resolves these constraints; the process parameters are listed in AppendixA.5. Figure 5.14 shows SEM

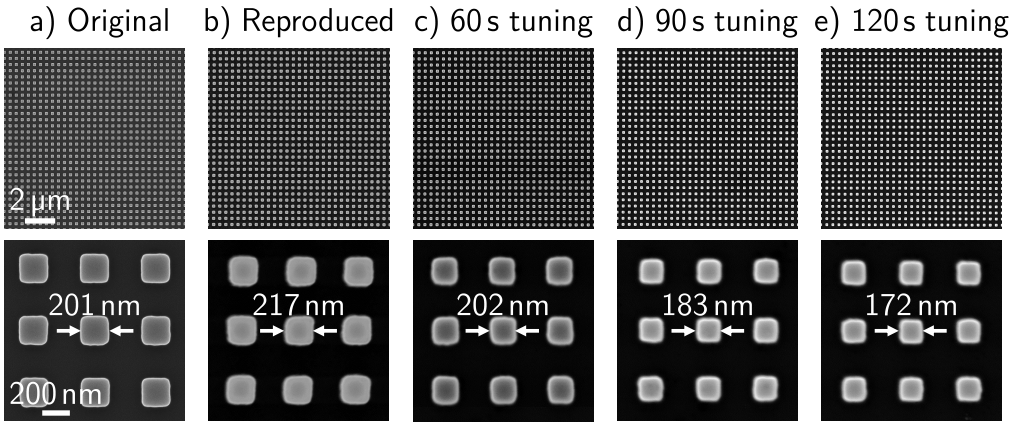

Figure 5.14: SEM images from the 200 nm stamp series of a) a reproduced SiO_2 stamp, b) a SiO_2 stamp after 60 s HF tuning, c) a SiO_2 stamp after 90 s HF tuning, and d) a SiO_2 stamp after 120 s HF tuning. Adapted with permission from [55].

images of the original 200 nm stamp, a reproduced SiO_2 stamp and tuned SiO_2 stamps fabricated with the chromium HF tuning method after 60 s, 90 s, and 120 s of HF tuning. The top row in Figure 5.14 shows an overview of each stamp, while the bottom images show zoomed-in SEM images of each stamp's features.

Figure 5.14a shows the SEM images of the original 200 nm stamp. The square features of the stamp are periodically arranged in a cubic lattice with a center-to-center distance of 440 nm. The overview image shows no defects or missing nanopillars in the lattice. We measure a side length of 201(2) nm for the original. Therefore, the uniformity of the pillars of the original 200 nm stamp is within a couple of nanometers.

Figure 5.14b shows a reproduced SiO_2 200 nm stamp before HF tuning. The overview SEM image on the top shows a defect-free stamp, and the measured side length of 217(3) nm is indicated in the zoomed-in image at the bottom. From the overview image, we can state that the reproduction process is not introducing any systematic defects to the stamp. However, the measured side length is substantially larger than the side length of the original stamp. Thus, the reproduction process increases the lateral dimensions of the stamp. However, the increase in side length is smaller than the increase we saw for the reproduced stamps in Figure 5.6b with the resist HF

tuning process. There, we attributed the increase in side length during evaporation to accumulating charges in the imprint resist and the SiO_2 during reproduction. Using the chromium HF tuning method, the charging effects occur closer to the surface of the SiO_2 as the chromium is thinner than the imprint resist before. Additionally, the conductivity of the chromium can help to mitigate charging effects. Hence, the effect on the dry etching process is decreased, decreasing the increase in side length during reproduction. Despite the increase in side length, the square shape of the stamp pillars is preserved after the reproduction process. Furthermore, the surface roughness of the reproduced stamp using the chromium HF tuning is decreased compared to the reproduced stamp using the resist HF tuning process because the chromium is not etched during the dry etching of the SiO_2 preserving the surface of the SiO_2. The high stability of the chromium hard mask during the etching process also leads to a smaller deviation of the side length of the nanopillars and, therefore, to a more uniform reproduced stamp.

After the successful reproduction process, we analyze the stamps after the HF tuning step. Figures 5.14c, 5.14d, and 5.14e show SiO_2 stamps after 60 s, 90 s, and 120 s of HF tuning, respectively. The respective overview SEM images show no defects for all three stamps. Therefore, the HF tuning process is not introducing major defects to the stamps. We measure a side length of 202(6) nm, 183(6) nm, and 172(4) nm for the 60 s, 90 s, and 120 s stamps, respectively. From the measured side length, we calculate lateral etch rates of $0.13\,\mathrm{nm\,s^{-1}}$, $0.19\,\mathrm{nm\,s^{-1}}$, and $0.19\,\mathrm{nm\,s^{-1}}$, respectively.

The tuning process increases the deviation of the nanopillars slightly. However, the precision of the tuned stamps is still within several nanometers. Therefore, the decrease in uniformity has no significant influence on our processes and applications. As expected, the tuning rates are similar to those measured for the resist HF tuning process. However, we do not see an increased lateral tuning rate for shorter tuning times. We attribute the absence of the high tuning rates at the beginning of the tuning process to the smoother reproduction process using the chromium nanoislands as an etching mask instead of the imprint resist. Additionally, the zoomed-in SEM images show that the square shape of the stamp nanopillars is well preserved during the tuning process. Overall, the tuning process is not changing the shape or surface roughness of the nanopillars, and the resulting stamps fabricated with the chromium HF tuning method are improved compared to the stamps fabricated with the resist HF tuning process.

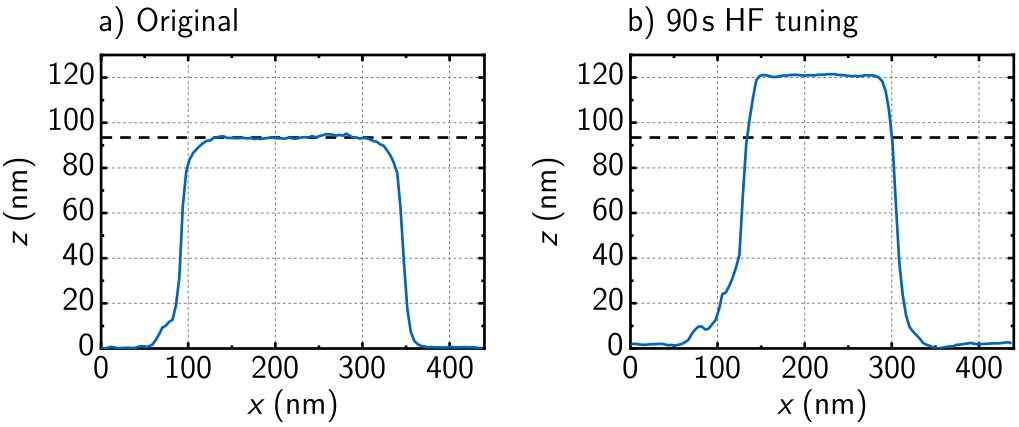

Figure 5.15: AFM height profiles of a) the original 200 nm stamp and b) a SiO_2 stamp after 100 s of HF tuning with the chromium HF tuning method. The black dashed line indicates the height of the original 200 nm stamp in each graph.

Pillar Height Analysis of the Tuned Stamps

In Figure 5.15, we compare the height of the 200 nm original stamp and a tuned stamp using the chromium HF tuning method. In Figure 5.15a, the blue line shows the height profile of the 200 nm original stamp. The dashed line indicates the height of the stamp pillar of 93 nm. Compared to that, in Figure 5.15b, the blue line shows the height profile of a reproduced and tuned Si_{02} stamp after 90 s of HF tuning. Again, the dashed line indicates the pillar height of the original 200 nm stamp. With a height of 121 nm, the pillars of the tuned stamp exceed the height of the original 200 nm stamp. Thus, the new chromium HF tuning method solves the pillar height limitations of the tuned stamps. Therefore, we found a tuning method that allows us a reliable fabrication of size-tuned imprinting stamps, which can be used in our existing NIL processes. Hence, we can now turn toward tuning the original 75 nm stamp, which has the most favorable characteristics for application in plasmonic experiments.

5.3.2 Chromium HF Tuning of 75 nm Stamps

The high selectivity between the chromium hard mask and the SiO_2 during the RIE etching step of the reproduction process allows us to select the pillar height of the reproduced stamp depending on the RIE etching time. Therefore, we solved the problems arising from the low pillar height after reproducing the stamps using the previous tuning methods. Thus, we developed a reliable and reproducible method to tune the feature sizes of our original imprinting stamps.

The tuning process aims to tune the imprinted features for plasmonic applications in the visible light regime. Therefore, we want to tune the feature sizes of the original 75 nm stamp, as the metal arrays produced with this stamp show a plasmonic resonance in the visible regime [55], [90], [91]. Due to the smaller features, the fabrication of metal nanoisland arrays with the 75 nm original stamp is more delicate than the fabrication with the larger stamps. Thus, we expect also the chromium HF tuning process to be more delicate for the original 75 nm stamp. Therefore, we conducted an in-depth analysis of the chromium HF tuning process of the original 75 nm stamp using the chromium HF tuning method described above to produce SiO_2 imprinting stamps with different feature sizes from the original 75 nm stamp; the process parameters are listed in AppendixA.5. Subsequently, we fabricate gold nanoisland arrays using these reproduced and tuned stamps.

Review of the Reproduction and Tuning Process

We took SEM images of the original stamp and SiO_2 stamps at different steps during the fabrication process to review the chromium HF tuning. Figure 5.16a–d shows an SEM image of the original stamp, chromium nanoislands fabricated with the original stamp, a reproduced stamp, and a HF tuned stamp, respectively. To further evaluate the shapes of the pillars of the original, the reproduced, and the tuned stamp, we took additional SEM images with a tilt of 45° and measured AFM height profiles of these stamps, which are shown in the second and third row, respectively.

To evaluate the diameter of the features of our samples, we determine the diameter of several tens of individual features from the SEM images equal to the 200 nm stamps above and calculate their mean value and standard deviation, which is given in parenthesis after each value. We measure a

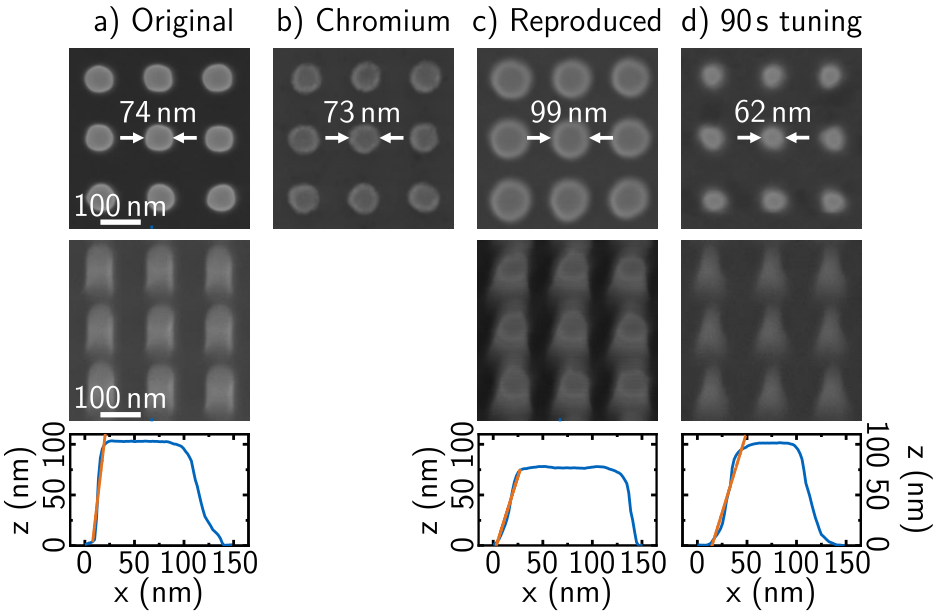

Figure 5.16: SEM images of the stamp and replica at different times during the replication and tuning process: a) The original stamp, b) a chromium nanoisland array after LO-NIL, c) a replicated stamp after dry etching and removal of the chromium, d) and a tuned stamp after 90 s of HF tuning. For each stamp, the top row of SEM images shows a top view at each stage. The bottom row of SEM images presents a 45° tilted SEM image of the stamps. Below the SEM images, an AFM height profile of a pillar of the respective stamp is depicted. The orange line in each AFM profile shows a linear fit to the sidewall of the respective pillar. Adapted with permission from [55].

diameter of 74(1) nm and 73(2) nm for the original stamp and the chromium islands, respectively. Thus, the dimensions of the stamp are well preserved during the LO-NIL process, confirming the chromium islands as an optimal hard mask for the subsequent SiO_2 etching.

With a measured diameter of 99(3) nm, the pillars of the reproduced stamp are larger compared to the pillars of the original stamp. The same behavior was also observed with the 200 nm stamps. As the chromium nanoislands have no increased diameter, the increase in pillar diameter occurs during reproduction. Furthermore, let us compare the tilted SEM images of the original stamp with the reproduced stamp. The sidewalls of the pillars of the

original stamp have a high, almost vertical slope, whereas the sidewalls of the pillars of the reproduced stamp have a decreased slope. To further analyze the slope of the pillars, we fitted a linear fit to the sidewalls of the original and reproduced stamp in the AFM height profile. The linear fits, indicated by the orange lines in the height profiles, give average slopes of 8.4 and 3.1 for the sidewalls of the original and the reproduced stamp, respectively. Therefore, the slope of the sidewalls decreases during the reproduction process.

We attribute the increase in diameter and the decrease of the slope of the sidewalls to charging effects during the dry etching of the SiO_2 pillars. SiO_2 is an insulating material. Therefore, the charges in the chromium discs and the underlying SiO_2, introduced by the ions in the plasma, cannot be immediately neutralized. Thus, an electrical field originates from the charges in the chromium discs. This electric field deflects further incoming ions away from the chromium discs, which leads to the increase in SiO_2 pillar diameter during the etching process as more charges accumulate. This effect leads to a conic shape of the pillars as their diameter increases with increasing etch depth. Nevertheless, the circular shape of the pillars is not affected during the reproduction process. Furthermore, the increase in diameter allows us the production of SiO_2 nanoimprinting stamps with a larger diameter, increasing our method's versatility.

Figure 5.16d presents an SEM image of a stamp after an HF tuning of 90 s. After the tuning process, the diameter of the pillars of the stamp decreases to 62(2) nm. Again, a conic shape of the pillars is visible in the tilted SEM image, and the linear fit to the sidewalls in the AFM height profile gives a slope of 3.2 Thus, the tuning process does not influence the slope of the sidewalls. Note that the different heights of the pillars of the reproduced and the tuned stamp originate from different etching times during the reproduction process and are unrelated to the tuning process. Overall, the whole chromium HF tuning process enables the pillar diameter tuning without changing the pillars' underlying circular shape. Furthermore, adding the preservation of the square shapes of the 200 nm stamps shown above, the tuning method preserves straight edges, corners, and circular features, allowing our chromium HF tuning method to be applied to more complex geometries for future applications.

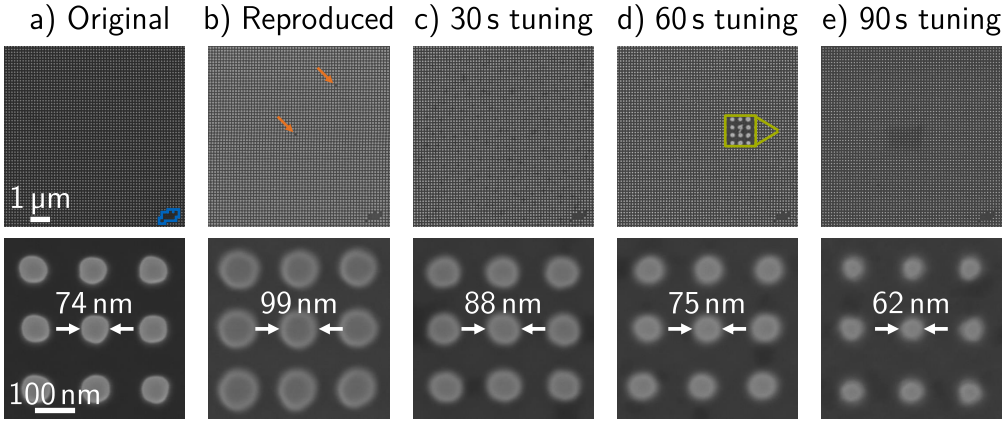

Figure 5.17: SEM images of a) the original stamp, b) a reproduced SiO_2 stamp, c) a SiO_2 stamp after 30 s HF tuning, d) a SiO_2 stamp after 60 s HF tuning, and e) a SiO_2 stamp after 90 s HF tuning. The respective top image shows an overview SEM image of each stamp at the same position on each stamp. The defect of the commercial stamp indicated by the blue frame is passed on to all other stamps. The bottom row shows a zoom onto the structures of each stamp. The diameters of the pillars are 74(1) nm, 99(3) nm, 88(3) nm, 75(3) nm, and 62(2) nm for the original stamp, the reproduced stamp and the tuned stamps, respectively. Reprinted with permission from [55].

Tuning 75 nm Imprinting Stamps to Different Sizes

In the previous section, we validated the chromium HF tuning method for the original 75 nm stamp; now, we will compare stamps with different HF tuning times to the original stamp. Figure 5.17 shows SEM images of the original 75 nm stamp, a reproduced stamp, and tuned stamps after 30 s, 60 s, and 90 s HF tuning. Here, the image at the top gives an overview of the features of the respective stamp, and the bottom image shows a zoom-in on the features to evaluate the diameter of the features of the stamp.

To better compare the SEM images of different stamps, we took the overview SEM image at a position where all stamps inherited a defect from the original stamp. This defect can be seen in the bottom right corner of the top image in Figure 5.17a and is indicated by a blue frame. All overview SEM images are taken at the same position on each stamp marked by this defect. Aside from the defect in the corner, no defects are visible in the

overview of the original stamp. The pillars of the original stamp are arranged periodically in a cubic lattice with a pitch of 150 nm. The bottom image in Figure 5.17a shows a zoom-in on the stamp features. The features have a measured diameter of 74(1) nm. Thus, the deviation of the individual pillars within the array is within nanometer precision. Using this original stamp, we performed the chromium HF tuning process described above to produce the SiO_2 stamps that are discussed in the following.

Figure 5.17b shows SEM images of a reproduced stamp. Besides the inherited defect in the lower right corner, we recognize two point defects in the top overview image marked by the orange arrows, where a single pillar is missing at each site. However, we do not observe a systematic increase of defects in the SiO_2 stamps due to the reproduction method. To quantify the quality of our reproduced and tuned SiO_2 stamps, we introduce the process yield as the quotient between the number of functional pillars of the respective SiO_2 stamp and the number of pillars of the original stamp. We use the overview images of Figure 5.17 consisting of $\tilde{4}000$ pillars for the yield calculation. The yield for the reproduced stamp is 99.9 %. For the pillars of the reproduced stamp, we measure a diameter of 99(3) nm. Therefore, the further HF tuning of the reproduced stamps starts at this pillar diameter. Besides the increased diameter, the pillars in the SEM image of the reproduced stamp are blurrier than those of the original stamp. The increased blurriness of the images of the SiO_2 stamp arises from the worse conductance of SiO_2 compared to silicon. Therefore, the electrons of the SEM are accumulating in the SiO_2, which influences the image quality because the accumulated electrons deflect incoming and scattered electrons before they can hit the detector.

Next, we compare SiO_2 stamps after different HF tuning times. Figure 5.17c, 5.17d, and 5.17e show SEM images of three reproduced SiO_2 stamps after 30 s, 60 s, and 90 s of HF tuning, respectively. Again, the top images show overviews of the stamps with the inherited defect from the original stamp in the lower right corner of each image. For the 30 s and 90 s tuned stamps, no further defects besides the inherited defect are visible in the overview SEM images. Therefore, the process yield for the two SiO_2 stamps is 100.0 %.

However, we recognize interconnections between some nanoislands in the SEM image of the 60 s tuned stamp. One of these interconnections is highlighted in the green framed zoom in Figure 5.17d. We attribute these interconnections to a defect during the chromium evaporation process. Excess

chromium on the silicon surface leads to bridges between neighboring islands. Despite the defects, the yield of the 60 s tuned stamp is still at 96.9 %.

The SEM images below the overview show a closer look at the tuned SiO_2 pillars of the respective stamps. We measure pillar diameters of 88(3) nm, 75(3) nm, and 62(2) nm, after 30 s, 60 s, and 90 s of HF tuning, respectively. From the decrease in diameter, we calculate lateral etch rates of $0.18\,\mathrm{nm\,s^{-1}}$, $0.20\,\mathrm{nm\,s^{-1}}$, and $0.21\,\mathrm{nm\,s^{-1}}$, respectively. The constant lateral etch rate allows us to adjust the pillar diameters with a precision of a few nanometers.

Reproducibility of the Chromium HF Tuning Process

To investigate the reproducibility of the Chromium HF tuning method, we produced additional SiO_2 stamps with equal tuning times. As for the previously tuned stamps, we took SEM images at different positions on the stamps and calculated the stamp pillars' diameter and standard deviation. Table 5.4 shows the calculated diameter and its deviation of the pillars of four reproduced stamps, three HF tuned stamps after 30 s seconds, and four HF tuned stamps after each 60 s and 90 s seconds. The diameter difference between stamps of the same tuning time is within a few nanometers. Therefore, the reproducibility of the process is within a few nanometers.

Table 5.4: Diameters of the pillars of different imprinting stamps after chromium HF tuning of the original 75 nm stamp

	REP	**30HF**	**60HF**	**90HF**
Stamp 1	99(3) nm	88(3) nm	75(3) nm	62(2) nm
Stamp 2	99(3) nm	90(3) nm	74(2) nm	61(5) nm
Stamp 3	104(3) nm	90(3) nm	76(2) nm	67(3) nm
Stamp 4	104(3) nm		81(3) nm	65(2) nm

Table 5.5: Diameters of the pillars in different spots on the imprinting stamps after chromium HF tuning of the original 75 nm stamp

	ORG	REP	30HF	60HF	90HF
Corner1	75(1) nm	101(2) nm	93(2) nm	76(2) nm	65(2) nm
Corner2	74(1) nm	97(3) nm	86(3) nm	74(2) nm	60(1) nm
Corner3	75(1) nm	101(1) nm	86(2) nm	78(2) nm	62(2) nm
Corner4	73(1) nm	99(2) nm	90(2) nm	72(3) nm	63(2) nm
Center	75(1) nm	97(2) nm	87(2) nm	75(5) nm	62(2) nm
Overall	74(1) nm	99(3) nm	88(3) nm	75(3) nm	62(2) nm

Uniformity of the Chromium HF Tuning Process

Furthermore, we also investigate the uniformity of the pillar sizes over the patterned area after using the chromium HF tuning method. For that, we took SEM images at different positions on each imprinting stamp. In particular, we took SEM images at each of the four corners and in the center of the patterned area. Table 5.5 shows the calculated diameters and their standard deviations of the pillars of the original stamp, a reproduced stamp, and HF tuned stamps after 30 s, 60 s, and 90 s at each position and their overall diameter. The difference in the measured diameters at each position of all stamps is within a few nanometers. However, this difference slightly increased from the original to the reproduced and tuned stamps. We attribute the uniformity decrease to the reproduction process. The charging effects occurring during the dry etching of the SiO_2 influence the anisotropy of the process. Therefore, the uniformity of the stamp pillars. Nevertheless, we do not expect an influence on the plasmonic properties of the later produced metal nanoisland arrays, as the decrease in uniformity is within a few nanometers.

Lower Size Limit for the Tuning Process

Simulations show a decreased plasmonic response for nanoisland arrays with island diameters below 50 nm because the distance between the individual islands increases. Therefore, HF tuning times of up to 90 s are sufficient for our plasmonic applications. However, we fabricated additional stamps

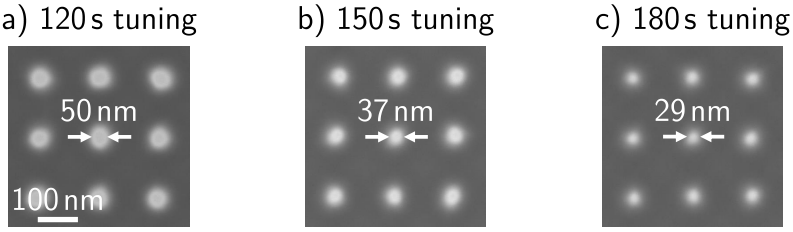

Figure 5.18: SEM images of a) a SiO_2 stamp after 120 s HF tuning, b) a SiO_2 stamp after 150 s HF tuning, and c) a SiO_2 stamp after 180 s HF tuning. The diameter of the pillars are 50(3) nm, 37(3) nm, and 29(2) nm for the tuned stamps, respectively. Adapted with permission from [55].

with longer HF tuning times to investigate the limits of our tuning process. Figure 5.18 shows SEM images of SiO_2 stamps after 120 s, 150 s, and 180 s HF tuning. The calculated diameters are 50(3) nm, 37(3) nm, and 29(2) nm for the shown stamps, respectively. We were not able to resolve smaller structures using our SEM. However, in theory, the limitation of the HF tuning process is the mechanical stability of the SiO_2 at the desired aspect ratio of the stamp pillars. For this work, we can state the feasibility of sub-30 nm stamp features.

Fabrication of Nanoisland Arrays

We successfully tuned the original 75 nm stamp. Now, we fabricate metal nanoisland arrays using the original, reproduced, and tuned stamps for the process; the process parameters are listed in AppendixA.5. The metal nanoislands consist of 17 nm gold on top a 3 nm titanium adhesion layer. SEM images of these gold nanoisland arrays are shown in Figure 5.19. Figure 5.19a–e show each SEM images of a gold nanoisland array fabricated with the respective stamps shown in Figure 5.17; an overview at the top and a zoomed-in image at the bottom. Beyond the SEM images, an AFM height profile of the respective array is presented. The SEM images in Figure 5.19 show that it was possible to fabricate gold nanoisland arrays with all reproduced and tuned stamps, and the AFM profiles show that all gold nanoisland arrays have the same height of 20(1) nm.

In the top SEM image of the nanoisland array fabricated with the original stamp (ORG array), we again recognize the defect inherited from the origi-

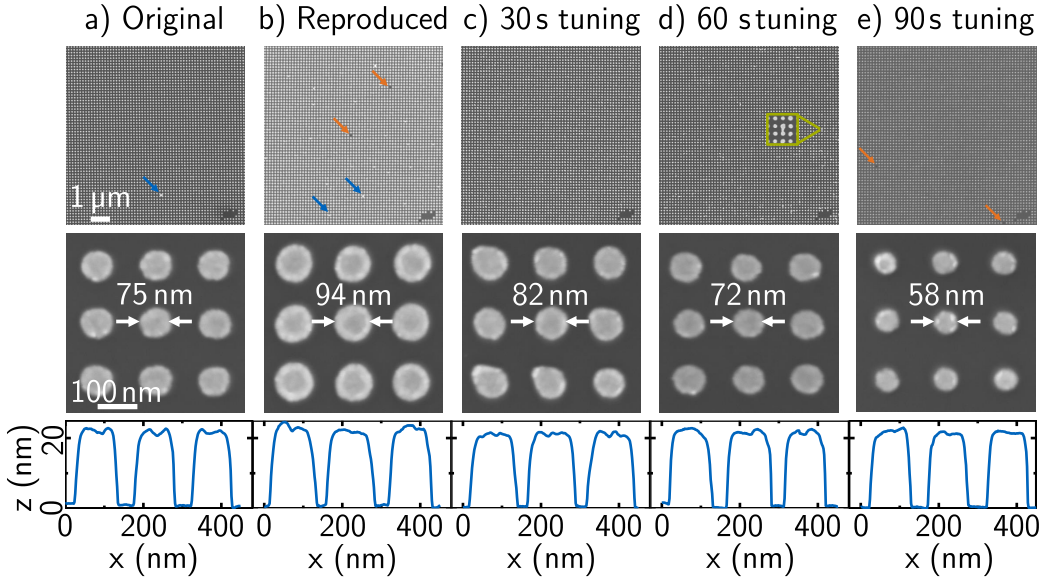

Figure 5.19: SEM images of gold nanoisland arrays fabricated with a) the original stamp, b) a reproduced SiO_2 stamp, c) a SiO_2 stamp after 30 s HF tuning, d) a SiO_2 stamp after 60 s HF tuning, and e) a SiO_2 stamp after 90 s HF tuning. The top row shows an overview SEM image of each sample at the same position on each array. The defect of the original stamp is visible in all nanoisland arrays. The second row shows a zoom onto the structures of each gold nanoisland array. The diameters of the gold nanoislands are 75(1) nm, 94(3) nm, 82(3) nm, 72(4) nm, and 58(3) nm for the original stamp, the reproduced stamp, and the tuned stamps, respectively. At the bottom, AFM height profiles are shown for each nanoisland array. The height of all nanoislands is 20(1) nm. Reprinted with permission from [55].

nal stamp in the bottom right corner. Besides the inherited defect, a defect marked by a blue arrow is visible in the array; here, four nanoislands interconnect. This kind of defect originates from a collapse of four neighboring pillars in the working stamp. However, the LO-NIL process is not introducing systematic errors into the array. Again, we define a process yield, calculated from the overview images of Figure 5.19. The yield for the LO-NIL process is the quotient between the number of functional gold nanoislands in an array divided by the number of pillars of the original stamp. The ORG array has a process yield of 99.9 %. The bottom image in Figure 5.19a shows a zoom on

the individual nanoislands of the ORG array. The nanoislands of the ORG array have a diameter of 75(1) nm; thus, the LO-NIL process converts the dimensions from the original stamp to the nanoisland array within nanometer precision.

Next, we focus on the nanoisland array produced with the reproduced SiO_2 stamp (REP array). In the overview image at the top of Figure 5.19b, we find two different types of defects besides the inherited defect from the original stamp. The first type is a point defect where single nanoislands are missing, marked by orange arrows. These defects are inherited from the reproduced stamp in Figure 5.17b. The second type, examples marked by the blue arrows, is an interconnection between two or four nanoislands like the defect in the ORG array. However, the LO-NIL process also worked for the reproduced stamp with a process yield of 99.2 %. The zoom at the bottom of Figure 5.19b shows a closer look at the metal nanoislands. The fabricated gold nanoislands of the REP array have a measured diameter of 94(3) nm.

Figure 5.19c, 5.19d, and 5.19e show the SEM images of the nanoislands produced with the 30 s HF tuned stamp (30HF array), the 60 s HF tuned stamp (60HF array), and the 90 s HF tuned stamp (90HF array), respectively. The inherited defect from the original stamp is visible in each overview SEM image. In the overview image of the 30HF array in Figure 5.19c, no other defects are present; hence, the process yield is 100.0 %. The zoom shows circular nanoislands with a measured diameter of 82(3) nm for the 30HF array.

We recognize interconnections between some islands in the overview SEM image of the 60HF array in Figure 5.19d. These interconnection defects are inherited from the interconnection defects of the 60 s tuned stamp shown in Figure 5.17d. The green framed zoom shows the defect at the same position as in Figure 5.17d for the 60 s tuned stamp. Despite these minor defects, the LO-NIL process produced a regular nanoisland array of circular discs with a process yield of 98.5 %. The yield of the 60HF array increased compared with the 60 s tuned stamp; hence, some defects from the stamp are mitigated during the LO-NIL process. The nanoislands of the 60HF array have a diameter of 72(4) nm.

Last, we investigate the 90HF array. In the overview SEM image of Figure 5.19e, we recognize two point defects besides the inherited defect. These two point defects are not visible in the images of the tuned stamp in Fig-

Table 5.6: Diameter comparison of stamp pillars and nanoislands for the chromium HF tuning of the original 75 nm stamp

	Stamp pillars	Nanoislands	Difference
ORG	74(1) nm	75(1) nm	1(1) nm
REP	99(3) nm	94(3) nm	5(4) nm
30HF	88(3) nm	82(3) nm	6(4) nm
60HF	75(3) nm	72(4) nm	3(5) nm
90HF	62(2) nm	58(3) nm	4(3) nm

ure 5.17e. Therefore, the defects are introduced during working stamp fabrication or the LO-NIL process. The yield of the 90HF array is 99.9 %.

In conclusion, we can state that although the reproduction process and the LO-NIL process can introduce point defects into the nanoarrays, the yield of the final gold nanoislands is hardly influenced by the processes. The zoom on the gold nanoislands of the 90HF array at the bottom of Figure 5.19e shows circular nanoislands with a diameter of 58(3) nm.

All measured diameters of the stamps and the fabricated arrays and the difference in measured diameter between both are depicted in Table 5.6. The diameter of the pillars of the reproduced and tuned stamps is always larger than the diameter of the nanoislands of their respective gold nanoisland array. However, the difference in diameter between the gold nanoislands and their respective imprinting stamp pillars stays constant during the tuning process. As the diameter of the gold nanoislands of the ORG array matches the diameter of the pillars of the original stamp, the difference in diameter for the SiO_2 stamps and their respective nanoisland arrays stems not from the LO-NIL process itself. We instead attribute the difference in measured diameter to a measuring error regarding the diameter of the pillars of the SiO_2 stamps. In particular, the decreased slope of the sidewalls of the reproduced stamps and the charging effects in the SiO_2 during the SEM imaging lead to an overestimation of the diameter of the pillars of the SiO_2 stamps. In the second column of Table 5.6, the deviation in diameter between individual nanoislands of the same array also stays constant during the tuning process. Thus, the tuning process does not influence the uniformity of the gold nanoisland arrays.

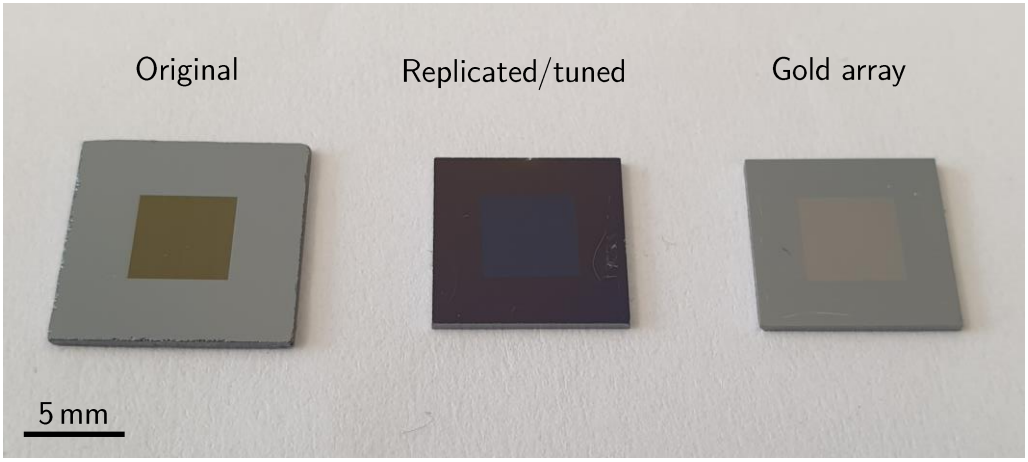

Figure 5.20: Picture of the original stamp, a replicated and tuned stamp, and a gold nanoisland array fabricated with the tuned stamp. The patterned array for all stamps and samples is $5 \times 5\,\mathrm{mm}^2$.

Image of Stamp and Sample

Figure 5.20 shows a picture of the original stamp, a replicated and tuned stamp, and a gold nanoisland array fabricated with the tuned stamp. Each stamp and sample comprises about 10^{11} individual pillars or nanoislands. We successfully tuned the feature sizes of the original 75 nm stamp and fabricated gold nanoisland arrays with the tuned stamps. With the chromium HF tuning method, we developed a reliable and precise process to tune the feature sizes of all our imprinting stamps isotropically. The method universally applies to all imprinting stamps used in our LO-NIL process. Especially the reproduction and tuning of the original 75 nm stamp allow us to improve applications using light-matter interactions in the visible light regime.

5.4 Application: Shifting the Plasmonic Resonance Frequency of Gold Nanoisland Arrays

The 75 nm circular features show light-matter interactions in the visible light regime and are, therefore, especially interesting for solar applications. To optimally harvest the energy from the incoming sunlight, the plasmonic resonance of the harvesting device should be at the wavelength of maximum sun intensity. Hence, to optimally use our gold nanoisland arrays, we want to tune the plasmonic resonance of our samples to around 500 nm.

A nanoisland's plasmonic resonance wavelength depends on its diameter [28], [55], [90]–[92]. Therefore, we can tune the plasmonic resonance of our gold nanoisland arrays by tuning the diameter of the nanoislands using the chromium HF tuning method.

5.4.1 Theoretical Concepts of the Localized Plasmon Resonance

Before we show our experimental data on the influence of the diameter of the nanoisland on the plasmonic properties of the gold nanoisland arrays, we give a short overview of the fundamentals of the involved physics of plasmons. We focus on the physics behind localized surface plasmons. This theory section was not part of the original paper [55] and is added to understand the application better.

Types of Plamons

In general, plasmons are the collective oscillations of free electrons in a metal [92]. Depending on the structural dimensions of the metal, we distinguish two forms of plasmons. In extended metal films, surface plasmon polaritons (SPP) can form when the electromagnetic field of an incoming photon couples to the free electron gas of the metal film. These SPPs can propagate along the metal surface [92].

In nanoparticles, the electromagnetic field of incoming photons can couple to the whole ensemble of free electrons in the nanoparticle. Such an excitation is called localized surface plasmon (LSP) [92]. In the following, we focus

on such LSPs as they are predominant in our nanoisland arrays.

Light-Matter Interactions of Metals

To better understand the coupling between the incoming light and the metal nanoparticles, we first look at the electric properties of metals. The electric response of a material is characterized by the material-specific dielectric function ϵ. In general, ϵ is a complex function dependent on the frequency ω of the interacting light [92]:

$$\epsilon(\omega) = \epsilon_1 + i\epsilon_2 \ . \tag{5.1}$$

For our purposes, we can assume that the dielectric function of a metal is approximately equal to the dielectric function of a free electron gas. The Drude model [93] of the optical response of metals gives the dielectric function of the free electron gas as

$$\epsilon(\omega) = 1 - \frac{\omega_\mathrm{p}^2}{\omega^2 + i\gamma\omega} \tag{5.2}$$

with the plasma frequency $\omega_\mathrm{p} = {}^{ne^2}/_{\epsilon_0 m}$ and γ the collision frequency of electrons in the free gas [92]. The collision of electrons drains energy from the system and leads to a damping of the electric response. Comparing Equation (5.1) and Equation (5.2) and using $\gamma = {}^1/_\tau$ with τ being the relaxation time of the free electron gas, we get

$$\epsilon_1(\omega) = 1 - \frac{\omega_\mathrm{p}^2\tau^2}{1 + \omega^2\tau^2} \tag{5.3}$$

and

$$\epsilon_2(\omega) = \frac{\omega_\mathrm{p}^2\tau}{\omega(1 + \omega^2\tau^2)} \tag{5.4}$$

for the real and imaginary parts of the dielectric function of metals regarding the Drude model. To excite plasmons on a metal-insulator interface, the real part of the dielectric function ϵ_1 must be negative, and the imaginary part ϵ_2 must be positive [92]. The condition is met for $\omega \ll \omega_\mathrm{p}$ where metals have their typical metallic character [92]. In this regime, metals are highly reflective. Typically, metals have their plasma frequencies in the UV light regime, reflecting the visible light [94]. Therefore, gold and silver are suitable materials for plasmonic applications in the visible regime [95].

Plasmonic Response of Gold Nanoislands

To evaluate the plasmonic response of our gold nanoislands, we first look at a gold nanosphere and extrapolate the results from there. We assume a gold nanosphere with diameter a in a quasi-static approximation, where $a \ll \lambda$, with λ being the wavelength of the incoming light. In this quasi-static approach, we can assume that the electric field of the light E_0 changes over time but is spatially constant over the dimensions of our nanosphere. This external electric field E_0 induces an electric dipole moment $\boldsymbol{p}$ in the nanosphere, whose magnitude is proportional to E_0 [92]:

$$\boldsymbol{p} = 4\pi\epsilon_0\epsilon_\mathrm{m}a^3\frac{\epsilon-\epsilon_\mathrm{m}}{\epsilon+2\epsilon_\mathrm{m}}\boldsymbol{E}_0 \ , \tag{5.5}$$

where ϵ_m is the dielectric constant of the surrounding medium, and ϵ is the dielectric constant of the sphere material. We introduce the polarizability α of the sphere via $\boldsymbol{p} = \epsilon_0\epsilon_\mathrm{m}\alpha\boldsymbol{E}_0$ and get

$$\alpha = 4\pi a^3\frac{\epsilon-\epsilon_\mathrm{m}}{\epsilon+2\epsilon_\mathrm{m}} \tag{5.6}$$

for the polarizability of a small sphere in the quasi-static approach.

We get a resonant enhancement of the polarizability under the condition that $\epsilon + 2\epsilon_\mathrm{m}$ is minimized. Which can be realized if $\mathrm{Im}\left[\epsilon(\omega)\right]$ is small and $\mathrm{Re}\left[\epsilon(\omega)\right]$ is negative. We saw before that both conditions are valid for metals if $\omega \ll \omega_\mathrm{p}$, which is valid for gold in the visible light regime [95]. In this case, the resonance condition simplifies to

$$\mathrm{Re}\left[\epsilon(\omega)\right] = -2\epsilon_\mathrm{m} \ . \tag{5.7}$$

This condition for resonant enhancement of α is the well-known Fröhlich condition [92]. The Fröhlich condition expresses a strong dependence of the resonance frequency on the dielectric environment ϵ_m of the nanosphere. However, in this quasi-static approach, we see no dependence of the resonance frequency on the dimensions of the nanosphere.

The quasi-static approach is strictly valid only for infinitesimal small particles. For larger particles, the electric field's changing phase over the particle's volume must be considered to evaluate their plasmonic response. The theory to evaluate such plasmonic response was first introduced by Gustav Mie

in 1908 and is now known as Mie theory [82]. Mie is introducing a set of normal modes described by vector harmonics to describe the complete scattering of a gold nanosphere. For this work, it is sufficient to focus only on the first-order perturbations to the quasi-static approach arising from Mie theory rather than reviewing all calculations. We refer to [83], [96] for a complete discussion of Mie's theories.

Taking first-order perturbations of Mie theory into account, we can rewrite the polarizability of a sphere with volume V as

$$\alpha_{\text{sphere}} = \frac{1 - \left(\frac{1}{10}\right)(\epsilon + \epsilon_{\text{m}})\, x^2 + O\left(x^4\right)}{\left(\frac{1}{3} + \frac{\epsilon \text{m}}{\epsilon - \epsilon \text{m}}\right) - \frac{1}{30}(\epsilon + 10\epsilon_{\text{m}})\, x^2 - i\frac{4\pi^2 \epsilon_{\text{m}}^{2/3}}{3}\frac{V}{\lambda^3} + O\left(x^4\right)}\,, \tag{5.8}$$

where $x = {}^{\pi a}/_{\lambda}$ is the size parameter, which links the sphere's radius to the vacuum wavelength. Compared to the quasi-static solution, three new terms appeared; one in the numerator and two in the denominator. In the following, we will state the physical meaning of all three terms.

The new term in the numerator quadratic in x introduces the effect of retardation of the exciting field over the volume of the sphere. The additional term leads to a shift in the plasmonic resonance [92]. The first new term in the denominator quadratic in x introduces the retardation of the depolarization field [97] inside the particle and also shifts the plasmon resonance.

Overall, the shift for noble metals under the Drude model is towards lower energies and, thus, higher wavelengths for increasing x. As x increases, the particle size increases. Thus, the plasmon resonance red shifts with increasing particle size. The new imaginary term in the denominator accounts for radiation damping and does not influence the resonance frequency [98].

Despite geometrical differences between the analyzed nanosphere and our nanoislands, the overall dependences are the same for both geometries [90]–[92]. Therefore, we expect a blue shift of the plasmonic resonance frequency with decreasing diameters of our gold nanoislands.

Coupling Effects between Multiple Nanoislands

So far, we have only looked at the plasmonic response of single particles. As our samples consist of an array of nanoislands, it is worth looking briefly at the coupling effects of multiple particles and their influence on the system's plasmonic resonance. For simplicity, we first look at a one-dimensional line of

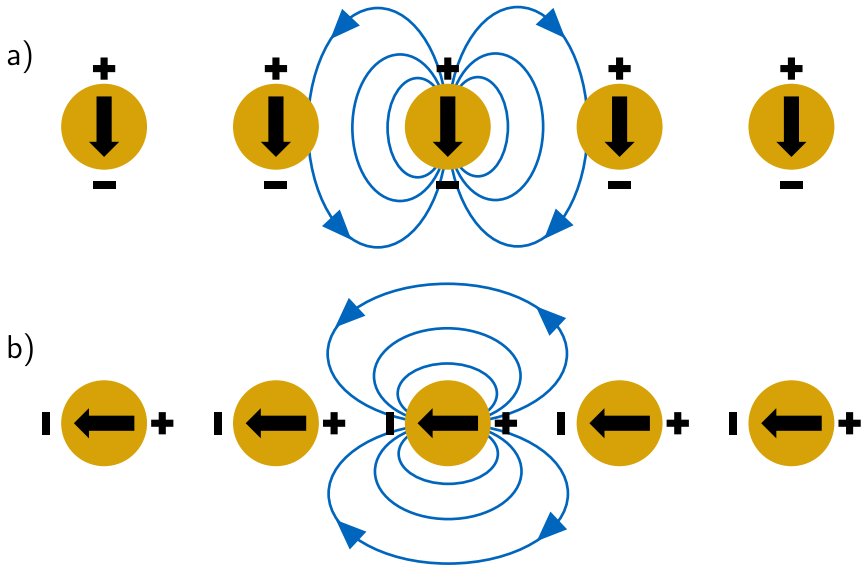

Figure 5.21: Schematic depiction of the near-field coupling of a line of adjacent nanoislands. Depending on the polarization of the exciting light, two configurations are possible; a) longitudinal polarized excitation and b) transverse polarized excitation.

adjacent nanoparticles focusing on the near-field coupling of particles where $d \ll \lambda$, with d the distance between particles and λ the vacuum wavelength.

Two configurations of near-field coupling are possible depending on the polarization of the exciting light. Figures 5.21a and 5.21b show the longitudinal and transversal polarized light configurations, respectively. The plasmonic electric fields of the nanoislands are either weakened for transverse or enhanced for longitudinal polarization of the exciting light [99]. Thus, the restoring force acting on the electrons of each particle is either decreased or increased, leading to a red shift of the plasmon resonance for transverse modes and a blue shift for longitudinal modes.

In our system, we illuminate the 2D nanoisland arrays from the top with unpolarized light. Therefore, a statement on the configuration of our system is difficult. We assume a combination of the two configurations averaged over the whole sample for our unpolarized setup. To further investigate the polarization dependence of the plasmonic resonance of our sample, we must conduct experiments using polarized light. Due to the plasmonic coupling of

neighboring islands in the longitudinal configuration, enhancing the electric field is particularly interesting for applications with high electric fields, such as plasmon-assisted catalysis.

5.4.2 The Influence of the Nanoisland Diameter on the Plasmon Resonance

It is especially interesting to analyze the plasmonic properties of the nanoimprinted metal nanoisland arrays for our experiments. Therefore, we conduct UV-VIS transmittance experiments to investigate the influence of the tuned diameters on the plasmonic resonance of the gold nanoisland arrays. Therefore, we fabricate gold nanoisland arrays with the tuned stamps from the previous section on fused silica, which is transparent in the UV-VIS regime and measured transmittance spectra.

For the UV-VIS measurement, we use a deuterium halogen light source AVA AvaLight-DH-S-BAL and an AvaSpec-2048 spectrometer from Avantes, Netherlands. Figure 5.22a displays transmittance spectra of five gold nanoisland arrays fabricated with the stamps from the previous section. The green dots show the transmittance spectrum of the ORG array, and the blue dots show the transmittance spectrum of the REP array, the 30HF array, the 60HF array, and the 90HF array from dark to light blue, respectively. The transmittance spectrum of each measurement is normalized to the transmittance of the UV-VIS setup without a sample. In each plot, the orange line illustrates a Breit-Wigner fit to the respective spectrum. The fits are conducted to extract the plasmonic resonance wavelength from each measurement. The centers of the plasmonic resonance peeks lie at 609 nm, 637 nm, 609 nm,, 595 nm, and 580 nm for the ORG array, the REP array, the 30HF array, the 60HF array, and the 90HF array, respectively. As expected, the plasmonic resonance peak is blueshifted with decreasing gold nanoisland diameter as the localized plasmon resonance is confined to a smaller structure [28], [90], [91]. The overall normalized transmittance increases with decreasing nanoisland diameter. The increase in transmittance can be explained by the decrease of overall gold on the sample surface with decreasing diameter of the gold nanoislands as the pitch stays constant.

We conducted simulations of our system to compare our measurements with the theory. The simulations of the transmittance of our system are per-

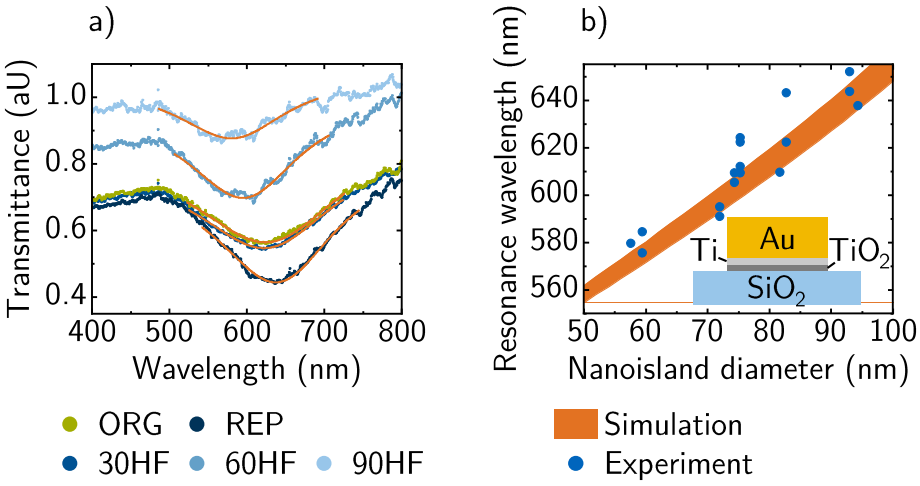

Figure 5.22: a) Transmittance spectra of the fabricated gold nanoisland arrays on fused silica. The green dots show the transmittance of the ORG array. The blue lines show the transmittance of the REP array, the 30HF array, the 60HF array, and the 90HF array from dark to light blue, respectively. The orange lines show a Breit-Wigner fit to each spectrum. b) Comparison of the measured and simulated plasmonic resonance wavelength. The blue dots represent the measured plasmonic resonance wavelength of our gold nanoisland arrays, and the orange area represents the simulated plasmonic resonance wavelength for gold nanoisland arrays with a feature height of 20(1) nm. The orange area is obtained as the area between the simulations of a nanoisland array with 19 nm and 21 nm feature height. The inset shows a scheme of the simulated structures. Reprinted with permission from [55].

formed with COMSOL Multiphysics using the Electromagnetic Waves Module. Figure 5.22b compares gold nanoisland arrays' experimentally measured resonance wavelengths with the simulated plasmonic resonances. The blue circles represent the experimentally measured plasmonic resonance wavelengths of our samples plotted against the measured diameter of the nanoislands. The orange area shows the simulated plasmonic resonance wavelengths of gold nanoisland arrays on fused silica as a function of different nanoisland diameters for nanoisland heights of 20(1) nm. Hereby, the orange area arises from the area between the simulated transmittance spectrum of

a nanoisland array with a feature height of 19 nm and an array with feature height of 21 nm. The simulations calculate the transmittance of a periodic array of gold nanoislands on fused silica. A scheme of the simulated stack is depicted in the inset of Figure 5.22b. Our gold nanoislands on fused silica are represented by an SiO_2 substrate, a 3 nm titanium adhesion layer, which is half oxidized to TiO_2, and a gold layer of 17(1) nm. As with the experimental data, the plasmonic resonance wavelength of the simulated arrays is extracted from simulated transmittance curves by fitting a Breit-Wigner function to the data.

Focusing on the measured plasmonic resonance wavelengths, slight deviations in resonance wavelength between samples with the same measured diameter are present. We attribute the different resonance wavelengths to deviations in the evaporated metal height and different ratios of titanium and titanium oxide in the respective samples, which influence the plasmonic resonance of the nanoislands. The measured plasmonic resonance wavelengths follow the simulated area for all nanoisland sizes. Thus, we can now tune the plasmonic response of our samples according to each experiment and application. For example, suppose an experiment requires a specific plasmonic resonance wavelength. In that case, we perform a simulation to find the optimal dimensions for our nanoislands and then use the chromium HF tuning process to tailor a nanoimprinting stamp according to these simulations.

Chapter 6

Combining Nanoimprint and Optical Lithography

The previous chapter showed the possibility of tuning the sizes of imprinted nanoisland arrays below 30 nm, marking the lower size limit of our nanostructures. However, imprinting large structures of multiple hundred micrometers is not feasible with our NIL processes. Section 2.3.3 showed that the imprinting time increases quadratically with increasing stamp features. Therefore, the limitations of nanoimprinting techniques for increasing structure sizes depend on the imprinting process's physics. Instead, optical lithography (OL) becomes a viable alternative for larger structures, especially when the desired feature sizes exceed the diffraction limit of the OL process.

Therefore, we implemented a method to intercorporate an OL process and our nanoimprinting methods, combining both methods' advantages to fabricate sub-30 nm features and structures of multiple hundreds of micrometers on one sample. We utilize a µMLA (maskless aligner) from Heidelberg Instruments, Germany, for the OL process.

6.1 The Maskless Optical Lithography Process

Our OL process utilizing the MLA (MLA-OL) is designed for spin wave excitation and manipulation experiments. Thus, the process is explained by showing the materials and device structures needed for spin wave excitation devices. However, the MLA-OL process applies to all sorts of patterns and materials. Figure 6.1 schematically depicts the MLA-OL process exemplary for fabricating aluminum coplanar waveguides (CPWs) on yttrium iron garnet (YIG) supported by a gadolinium gallium garnet (GGG) substrate.

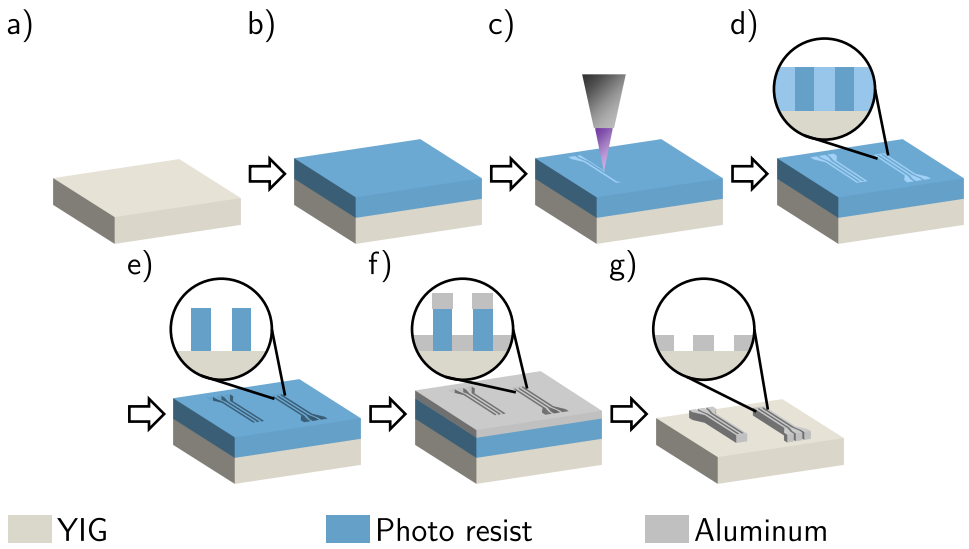

Figure 6.1: Schematic depiction of the MLA-OL process fabricating aluminum CPWs on YIG: a) The YIG substrate is cleaned in each Acetone and Isopropanol using an ultrasonic bath to remove unwanted contaminants. b) After cleaning, a photoresist is spin coated onto the substrate. c) The MLA uses a projection technique to sequentially UV expose the photoresist. d) After the process, the resist is exposed according to our predefined pattern. e) Now, the sample is developed to remove the UV-exposed parts of the photoresist. The inset shows the exposed YIG surface. f) Afterward, a layer of aluminum is evaporated on top of the sample. g) Finally, the aluminum CPWs are left on the YIG.

Such waveguides function as spin wave sources and detectors in spin wave devices [100]–[102].

First, the substrate is cleaned in each DMSO, Acetone, and Isopropanol using an ultrasonic bath. Figure 6.1a shows the cleaned substrate. After cleaning, a photoresist is applied to the substrate via spin coating. The photoresist is an optically active polymer specially designed for photolithographic applications. Figure 6.1b shows the substrate with applied photoresist. Now, the desired pattern is written into the photoresist using UV light. The UV light breaks the bonds of the exposed polymer and, therefore, locally alters the chemical properties of the resist layer, which changes the solubility of the resist. There are two different types of photoresists: positive and

negative. The solubility of the exposed resist is increased for positive resists, while for negative resists, it is decreased [103]. We use a positive photoresist for the MLA-OL process, but the process also applies to negative resists.

The MLA uses a projection technique comparable to a light projector to expose individual writing fields of a couple of hundred micrometers. Via the motion of small mirrors, individual pixels within the writing field are either exposed or left unexposed. The exposure dose is controlled by increasing or decreasing the exposure time for each writing field. After exposing a writing field, the sample is moved to the next writing field until the whole sample is covered. The projection technique allows an easy adaptation of the sample features, as any arbitrary form can be written, and the pattern can be changed for each sample. Figure 6.1c schematically depicts the sample in the MLA during the writing process. After exposure, the desired pattern is transferred into the resist as a chemically altered photoresist, as shown in Figure 6.1d. The inset indicates the different regions of increased solubility in light blue.

The changed solubility is used in the subsequent development step to remove the exposed photoresist with a suitable developer in a wet chemical etching step. Figure 6.1e shows the sample after the development step. The exposed parts of the resist are now removed, and the underlying substrate is uncovered. In comparison, in an OL process utilizing a negative photoresist, the not-exposed areas of the resist would be removed. Next, aluminum is evaporated onto the sample shown in Figure 6.1f. Last, the excess aluminum and remaining photoresist are removed using a suitable remover, which solves the remaining resist in a slow and controlled manner. The removal is performed in an ultrasonic bath to promote the lift-off process. The final sample is depicted in Figure 6.1g.

6.1.1 Size Limitations of the Maskless Aligner

To test the limitations of the MLA-OL process, we fabricated test structures with CPWs and squares with different side lengths; the process parameters are listed in Appendix A.6. Figure 6.2 shows optical microscopy images of such test samples after development in a) and after lift-off in b). The individual waveguides have line widths and gaps of 4 µm. Thus, the CPW structure has a total width of 20 µm. The squares have a side length of 4 µm, 3 µm, and 2 µm from the bottom to the top, respectively.

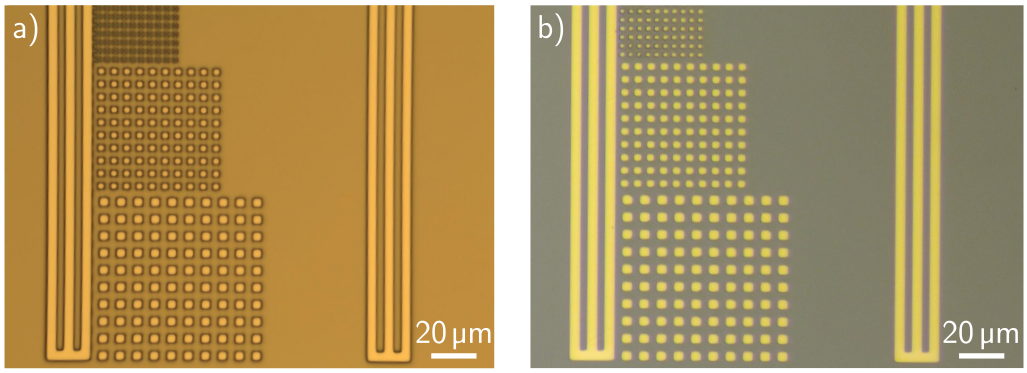

Figure 6.2: Optical microscope images of a test structure consisting of two CPWs and arrays of squares with side lengths of 4 µm, 3 µm, and 2 µm: a) after MLA exposure and development, and b) after evaporation of gold and lift-off.

In Figure 6.2a all features except the 2 µm squares are resolved properly. Due to diffraction limitations, the 2 µm squares in the resist are hard to resolve with the optical microscope. Nevertheless, the test features are transferred into the resist without systematic defects: the sizes are well preserved, and the square shape is recognizable. However, the corners of all features are rounded during the process, preventing the fabrication of perfectly sharp corners.

Figure 6.2b shows the test sample after the evaporation of gold and the subsequent lift-off. No features are missing, and no excess gold is visible on the sample. Thus, the lift-off was successful even for the smallest structures. However, the shapes of the 2 µm squares are not perfectly preserved during the process. To reliably fabricate structures down to 2 µm, the MLA process has to be adjusted for such small sizes. In particular, the development time or exposure dose must be increased as their optimal values vary for different feature sizes. Therefore, it can be hard to fabricate features with different sizes in the same process reliably with high precision. Unfortunately, we could not reliably fabricate structures smaller than 2 µm. Overall, the MLA-OL process complements the NIL processes for structure sizes above 2 µm, where imprinting techniques struggle due to increased imprinting times.

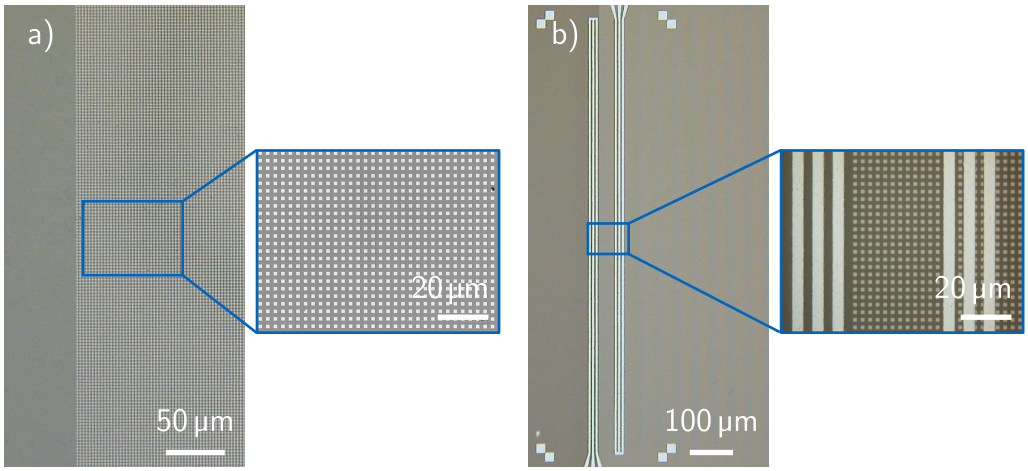

Figure 6.3: Optical microscopy images of a) a CoPT nanomagnet array fabricated with LO-NIL and b) the same array with added CPWs fabricated with MLA-OL.

6.1.2 Optical Lithography on Top of an Imprinted Nanoisland Array

To show the combination of LO-NIL and MLA-OL, we fabricate CPWs on top of a CoPt nanoisland array on a YIG-GGG substrate; the process parameters are listed in Appendix A.6. Figure 6.3 shows optical microscopy images of the nanoisland array before and after adding the CPWs. To fabricate the nanostructures, we first use the LO-NIL process described in Section 2.2.1 to fabricate a titanium nanoisland array on top of a CoPt layer. Then, the titanium islands are used as the hard mask for the dry etching of the CoPt. Figure 6.3a shows the fabricated nanoisland array from the 1400 nm stamp. The zoom shows the regular and defect-free nanoisland array.

The YIG substrate with the CoPt nanoislands array is used as the substrate for the MLA-OL process. As the height of the nanoislands is small compared to the desired resist thickness, their influence during spin-coating is negligible. The exposure dose and development time are adjusted to the new substrate, as the reflectance of the surface influences the MLA writing results. Figure 6.3b shows the sample after the fabrication of the waveguides. The waveguides are aligned parallel to the nanoisland array, where one waveguide lies alongside the array and the other on top of the array

shown in the zoom of Figure 6.3b. The MLA-OL process does not affect the CoPt nanoislands; no defects or alterations in the nanoisland array are visible in microscope images. Fabricating microscopic structures on or around our imprinted nanostructures and aligning them with sub-micron precision using MLA-OL opens up new applications at the interface between micro- and nanotechnology, like the spin wave application introduced in the next section.

6.2 Application: Spin Wave Manipulation with Nanomagnets

The MLA-OL process was developed to combine micron-sized CPWs for spin wave excitation with magnetic nanoisland arrays for spin wave manipulation. The nanomagnets influence the spin wave propagation in the medium below the array depending on the magnetization of the nanoislands. The ability to influence spin waves is essential for developing future spin-wave applications like neuromorphic computing devices in spin-wave computation [104]. The CPWs act as spin wave sources and detectors in such devices and must be incorporated into the nanoisland arrays. The application of LO-NIL and MLA-OL for magnonic devices is conducted in close cooperation with the group of György Csaba from Pázmány Péter Catholic University in Budapest. Our partners in Budapest developed the theoretical concepts behind the applications, which are the basis for the device fabrication and experimental characterization in our group. Ádám Papp from Pázmány Péter Catholic University in Budapest provided the simulations, and Martina Kiechle from our group at the Technical University of Munich conducted the spin wave measurements for this section.

6.2.1 Fundamentals of Spin Waves

To understand the fundamental physics behind the manipulation of spin waves with permanent nanomagnets, we briefly introduce the origin of spin waves and the influence of nanomagnets on spin waves. The spin wave propagation material, as well as the nanomagnets, are magnetic materials. Such materials contain atoms with an atomic net magnetic moment $\boldsymbol{\mu}$. We can consider such a material as a lattice with magnetic dipoles with a specific

orientation and amplitude at each lattice site [105]. For macroscopic objects with dimensions much larger than the interatomic distance, we can use the semi-classical approximation to define a continuous vector field instead of accounting for every magnetic dipole. The continuous vector field is called the magnetization $\boldsymbol{M}$ and is defined by the magnetic dipole moment per unit volume [106]:

$$\boldsymbol{M} = \frac{\sum_{\mathrm{i}} \boldsymbol{\mu}_{\mathrm{i}}}{\delta V} \ . \tag{6.1}$$

Magnetization Dynamics

Magnetization dynamics describe the change of the orientation of $\boldsymbol{M}$ over time. The magnetization's orientation depends on the magnetic field $\boldsymbol{H}$ acting on the magnetic material. In general, the magnetic energy E_{m} is minimized [106]; E_{m} is calculated with the following equation:

$$E_{\mathrm{m}} = -\mu_0 \boldsymbol{M} \cdot \boldsymbol{H} \ . \tag{6.2}$$

In equilibrium, the magnetization preferably aligns parallel to the acting magnetic field to minimize E_{m}. However, a precessional motion around $\boldsymbol{H}$ can be observed if the magnetization is forced out of equilibrium. The magnetization dynamics in the presence of one or more effective magnetic fields acting on the material are described by the Landau-Lifshitz-Gilbert (LLG) equation [107], [108]:

$$\frac{d\boldsymbol{M}}{dt} = -\gamma\mu_0 \left(\boldsymbol{M} \times \boldsymbol{H}_{\mathrm{eff}}\right) + \frac{\alpha}{M_{\mathrm{s}}} \left(\boldsymbol{M} \times \frac{d\boldsymbol{M}}{dt}\right) \ , \tag{6.3}$$

where γ is the gyromagnetic ratio, μ_0 is the vacuum permeability, α is the Gilbert damping constant, M_{s} is the saturation magnetization, and $\boldsymbol{H}_{\mathrm{eff}}$ combines all magnetic fields acting onto $\boldsymbol{M}$ [105]. The first term of the LLG describes the precession of the magnetization around the effective magnetic field. In contrast, the second part describes the attenuation of the precession and the energy loss of the magnetic excitation [105]. The Gilbert damping constant α is a phenomenological description of the superposition of all damping terms. Overall, combining both terms results in a spiral motion of the magnetization around the effective magnetic field until the magnetization and the effective magnetic field align again. The spiral motion of the magnetization is depicted in Figure 6.4.

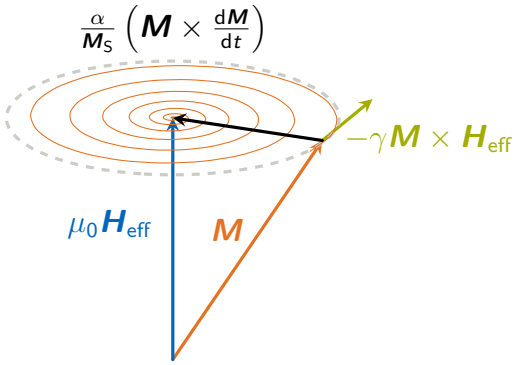

Figure 6.4: Visualization of the magnetization dynamics of a magnetization $\boldsymbol{M}$ around an effective magnetic field $\boldsymbol{H}_{\text{eff}}$. The two components of the LLG are illustrated separately. The spiral indicates the time evolution of the precession of magnetization. Reprinted with permission from [109]

In the following, we name and describe the most prominent interactions that make up the effective magnetic field $\boldsymbol{H}_{\text{eff}}$: A external magnetic field $\boldsymbol{H}_{\text{ext}}$ can be applied to the sample. Additionally, the magnetization generates the dipolar magnetic field $\boldsymbol{H}_{\text{dip}}$ called the demagnetization field inside the magnet and stray field outside of the magnet [110]. The dipolar magnetic field is strongly dependent on the shape of the magnet [106], [111]. Furthermore, the crystal structure of the magnet can lead to magnetic anisotropies, which result in a magnetocrystalline magnetic field $\boldsymbol{H}_{\text{cry}}$ [112]. The exchange interaction between neighboring magnetic dipoles leads to the exchange field $\boldsymbol{H}_{\text{ex}}$ [105]. For the discussion of further interactions in magnetic materials like Dzyaloshinskii-Moriya or magnetoelastic interactions, we refer to [106], [111], [112]. The corresponding magnetic field of each interaction is summed up to the effective magnetic field acting on the magnetization of the magnetic material.:

$$\boldsymbol{H}_{\text{eff}} = \boldsymbol{H}_{\text{ext}} + \boldsymbol{H}_{\text{dip}} + \boldsymbol{H}_{\text{cry}} + \boldsymbol{H}_{\text{ex}} + \dots \ . \tag{6.4}$$

Knowing the dynamics of the macroscopic magnetization of the magnetic material, we now want to focus back on the individual magnetic moments $\boldsymbol{\mu}$ of the magnetic materials. As the magnetization of the material is the sum of all individual dipole moments of the magnet, the findings for the magnetization dynamics can be equally applied to each magnetic dipole or spin in the lattice. A distinction is made between uniform and nonuniform excitation of

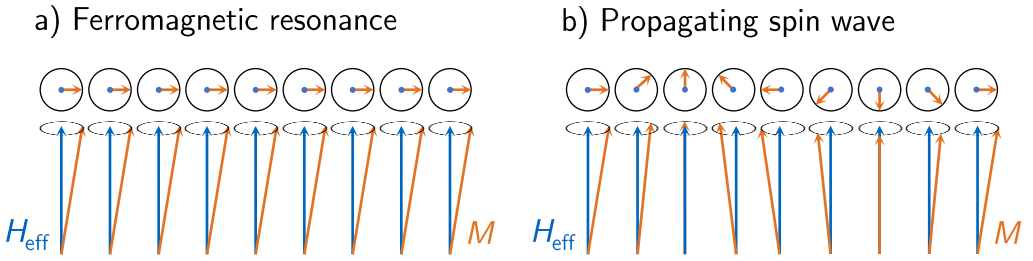

Figure 6.5: Schematical visualization of the spin precession of a) the FMR mode, and b) a spin wave mode. For the FMR mode, all spins precess in phase, while for the spin wave, the phase constantly changes between neighboring spins leading to a propagating excitation.

the spins over the entire magnetic volume. At uniform excitation, all spins precess in phase. This uniform excitation is called ferromagnetic resonance (FMR). Figure 6.5a depicts the ferromagnetic resonance excitation, where the magnetization indicated by the orange arrows precesses around the effective magnetic field indicated by the blue arrows with the same phase for all spins. At nonuniform excitation, the phase of the precession changes from spin to spin, and wave-like excitations of the magnetizations are possible, called spin waves. Figure 6.5b schematically shows a spin wave excitation. Here, the phase of the magnetization periodically changes from spin to spin to form a spin wave.

Forward Volume Spin Waves

The type of excited spin waves is dependent on the sample geometry, the direction of the effective field $\boldsymbol{H}_{\text{eff}}$, and the spin wave propagation direction [105]. In this work, we only use geometries that allow for the excitation of forward-volume (FV) spin waves. The terminology is a combination of forward, which indicates that the group and the phase velocity of the spin wave are in the same direction and volume for volume spin waves. Volume spin waves propagate in the bulk volume of the magnetic film in contrast to surface spin waves, which would only propagate on the film's surface. In the FV geometry, $\boldsymbol{H}_{\text{eff}}$ is perpendicular to the film surface, and the spin wave propagation in the film is isotropic. Such spin waves have a dispersion

relation of

$$\omega^2(k) = \omega_0(k)\left(\omega_0(k) + \omega_m 1 - \frac{1 - e^{-kd}}{kd}\right) , \tag{6.5}$$

where

$$\omega_0(k) = \gamma\mu_0\left(H_{\text{eff}} + \frac{2A}{\mu_0}k^2\right) \tag{6.6}$$

$$\omega_m = \gamma\mu_0 M_{\text{s}} \tag{6.7}$$

with the exchange stiffness constant A and the thickness of the magnetic film d [113]. A detailed discussion of the spin wave dispersion relation and alternative excitation geometries can be found in [113]. In this work, we want to look at the dispersion relation in a more conceptual way. We note that the possible k-values, and therefore the possible spin wave wavelengths, in a magnetic film depend on the thickness d of the film, the effective magnetic field H_{eff}, the saturation magnetization M_{s}, and the precession frequency ω. Hence, we must tailor those parameters according to the experimental needs to effectively excite spin waves in a magnetic film.

Spin Wave Excitation

To excite FV spin waves, we need a local oscillating in-plane (IP) magnetic field that initiates the spin to precession around the external out-of-plane (OOP) magnetic field $\boldsymbol{H}_{\text{eff}}$. In our experimental setup, $\boldsymbol{H}_{\text{eff}}$ is dominated by an externally applied OPP magnetic field $\boldsymbol{H}_{\text{ext}}$. Therefore, we can assume $\boldsymbol{H}_{\text{eff}} = \boldsymbol{H}_{\text{ext}}$. It is important to note that spin waves can only be excited if the dispersion relation solves for a possible k-value for the combination of the precession frequency ω and the OOP magnetic field H_{ext}. For the excitation, we use CPWs, as shown in Figure 6.3 as spin wave transducers. The radio frequency (RF) signal fed into the transducer is translated into spin waves in the underlying spin wave host material. The frequency of the RF signal f translates into the precession frequency ω of the spin waves with $\omega = 2\pi f$, which allows us to set ω via the input RF signal. The transducers are contacted in a way that the applied current flows through the middle signal line and back equally through both outer ground lines.

Using the Biot–Savart Law, we can calculate the IP magnetic field induced by the current densities in the transducer, shown in Figure 6.6a. The blue

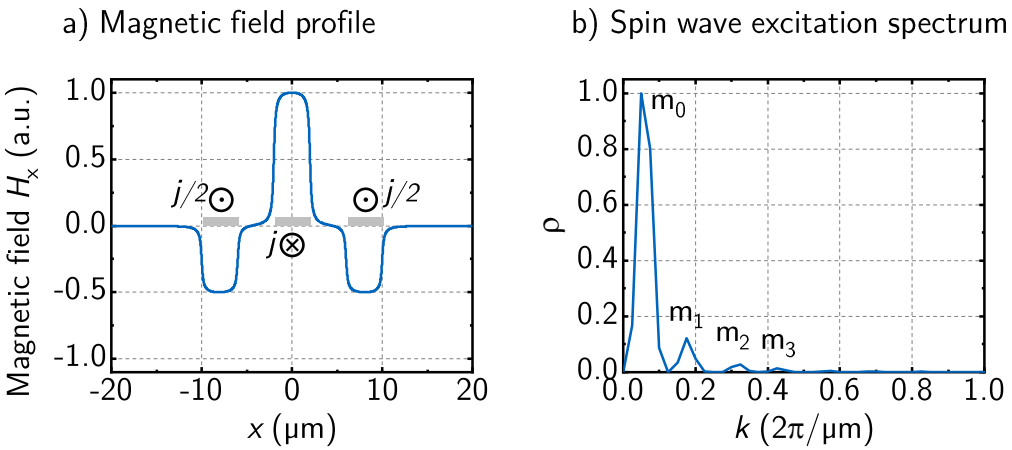

Figure 6.6: a) Calculated and normalized in-plane magnetic field profile of a CPW using the Biot Savart Law. The gray rectangles illustrate the position of the CPW. The applied current density flows through the middle strip and returns equally through both outer strips. b) The corresponding SWES ρ is calculated as the Fourier transform of the field profile in a). Spin wave excitation modes up to m_3 are visible.

line shows the normalized in-plane magnetic field H_x, while the grey rectangles indicate the positions of the signal and ground lines. The magnetic field strength induced by the signal line is twice as high as for the ground lines, and the direction is inverted. The IP magnetic field oscillates according to the RF frequency, and the OOP-oriented spins are forced out of their equilibrium and thus start to precess around $\boldsymbol{H}_{\text{ext}}$. The dipole-dipole interactions between the spins lead to a propagation of the spin wave into the film. The transducer excites a spin wavefront parallel to the CPW on both sides, propagating in opposite directions away from the transducer.

The transducer's magnetic field profile directly determines the transducer's spin wave excitation spectrum (SWES). The SWES gives the k-vectors, where spin wave excitation is possible using a particular transducer geometry. The boundary conditions for the magnetostatic potential define the SWES as the spatial Fourier transform of the magnetic field profile $\mathcal{H}(k)$ [100]. The SWES $\rho(k)$ is typically normalized to its maximum value and calculated

as [114]

$$\rho(k) = \frac{|\mathcal{H}(k)|}{|\mathcal{H}(k)|_{\max}} \ . \tag{6.8}$$

Figure 6.6b shows the SWES calculated from the magnetic field profile in Figure 6.6a. The strong main peak m_0 of the SWES gives the fundamental spin wavelength excited by the transducer. Additionally, we recognize several smaller peaks m_1–m_3, which indicate higher-order spin wave excitations; they resemble the spatial harmonics of the CPW geometry. The transducer cannot excite spin waves with k-vectors lying between the peaks. The shape of the magnetic field profile is almost solely dependent on the lateral dimensions of the transducer. Therefore, a transducer's preferred excited wavelength can be adjusted by changing its lateral dimensions [101].

To efficiently excite spin waves in a film, the applied magnetic field $\boldsymbol{H}_{\text{ext}}$, the excitation RF frequency f, which translates into the precession frequency ω, and the dimensions of the transducer must be coordinated with each other. The $\boldsymbol{H}_{\text{ext}}$ and ω define the wavelength λ_{SW} of the possible spin wave excitation via the dispersion relation, Equation (6.5). At the same time, the dimensions of the transducer define the SWES of the excitation and, thus, the efficiency of spin wave excitation at wavelength λ_{SW}. By changing $\boldsymbol{H}_{\text{ext}}$ or ω, λ_{SW} is matched to the modes m_0–m_3 of the SWES to guarantee spin wave excitation. In that way, if we coordinate the properties of the YIG film, the RF signal f, the external magnetic field $\boldsymbol{H}_{\text{ext}}$, and the transducer geometry, we can create customized spin-wave systems according to the requirements of their application.

6.2.2 Influencing Spin Waves with CoPt Nanomagnets

We introduced what spin waves are, how they can be excited, and what types of spin waves we are dealing with in our experimental setups. Now we want to focus on manipulating spin waves using CoPt nanomagnets. The magnetic field of such nanomagnets locally changes the magnetic landscape in the YIG film, which influences the spin waves' dispersion relation, comparable to a refractive index change for spin waves.

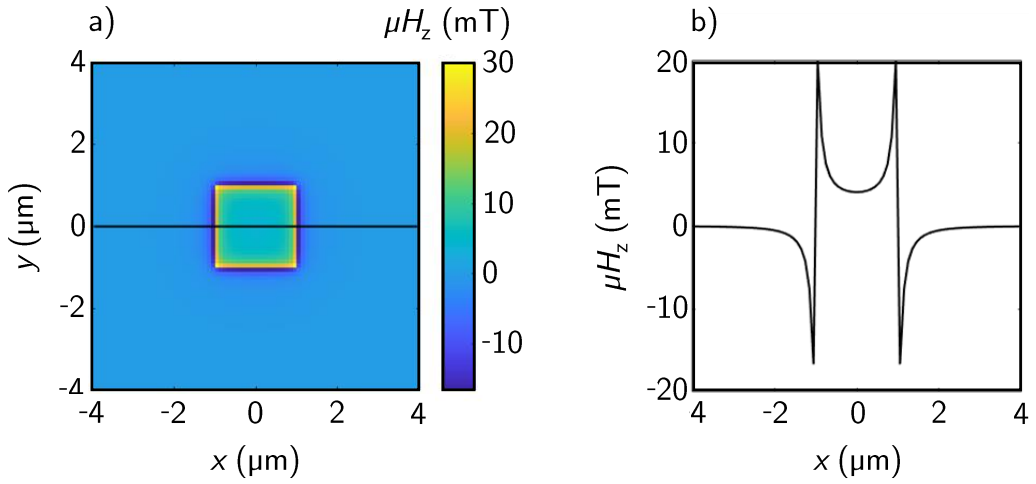

Figure 6.7: Simulated out-of-plane magnetic field profile of a CoPT PMA magnet with side length 2 µm. a) Color plot of the 2D magnetic field profile. The black line indicates the position of the cross-section plotted in b).

Nanomagnets with Perpendicular Magnetic Anisotropy

Besides changing the external magnetic field $\boldsymbol{H}_{\text{ext}}$ globally to change the spin wave dispersion, it is also possible to alter $\boldsymbol{H}_{\text{ext}}$ locally via nanosized permanent magnets. The magnetic field of the nanomagnets $\boldsymbol{H}_{\text{nano}}$ must be parallel to $\boldsymbol{H}_{\text{ext}}$ and perpendicular on the YIG film surface for the FV configuration.

Bulk permanent magnetic films usually have an IP magnetic anisotropy, which leads to a magnetic field parallel to the YIG film [106], [111]. Therefore, we use layered CoPt magnets with perpendicular magnetic anisotropy (PMA). Here, the layered structure of the magnets introduces multiple interfaces between different magnetic materials, which breaks the magnetic anisotropy K [115]. In general, K can be written as

$$K = K_{\text{V}} + \frac{2K_{\text{S}}}{d} \,, \tag{6.9}$$

where K_{V} is the volume anisotropy from the bulk film, K_{S} is the surface anisotropy, and d the thickness of the magnetic stack. The surface anisotropy outweighs the volume anisotropy for CoPt magnetic films because of their

layered structure. Figure 6.7a shows a color plot of the simulated perpendicular magnetic field profile H_z for a CoPt nanomagnet with a side length of 2 µm. Especially the edges of the nanomagnet show strong magnetic fields, which is further emphasized by the cross section plotted in Figure 6.7b.

The OOP H_z allows us to locally change the dispersion of the spin waves propagating in the YIG film beyond the nanomagnets. The spin wave dispersion change is comparable to a refractive index change for electromagnetic waves. Note that the magnonic refractive index is wavelength depended due to the non-linear dispersion relation. We can use magnonic refractive index change to engineer magnonic devices for spin waves comparable to optical devices for electromagnetic waves like spin wave lenses or scatterers [116], [117]. Furthermore, the technique can be used to develop neuromorphic spin wave devices [104].

Test Sample and Experimental Setup

The theory suggests that CoPt PMA nanomagnets influence the dispersion of spin waves in the underlying YIG film due to their OOP magnetic field. Before we think about applying this effect in a magnonic spin wave device, we want to affirm the theory. For that, we designed a test sample to evaluate the influence of CoPT magnets on spin wave propagation in an underlying YIG film. So, we want to confirm Snell's law for spin waves. The magneto-optic Kerr effect (MOKE) is used to visualize spin waves, where the polarization of a laser beam reflected on the YIG is rotated according to the phase of the spin wave [118]. The spin wave propagation is recorded using time-resolved MOKE (tr-MOKE) measurements [116], [117]. The test sample and experimental setup are schematically depicted in Figure 6.8a. The test sample consists of two parallel CPW transducers, which act as spin wave sources, a nanomagnet array between both transducers, and two different test geometries outside the transducers. The first test geometry consists of individual nanomagnets with different distances to the transducer. The second test geometry is a step-like nanomagnet pattern with increasing rows of nanomagnets, starting with a single row. The whole test sample is fabricated on a 100 nm thin YIG film, which is sputtered on a gadolinium gallium garnet (GGG) substrate. The nanomagnets consist of 14 alternating layers of Co and Pt, with a Co layer thickness of 0.4 nm and a Pt layer thickness of 0.8 nm, shown in the zoom of Figure 6.8a. The nanomagnets have a side length and

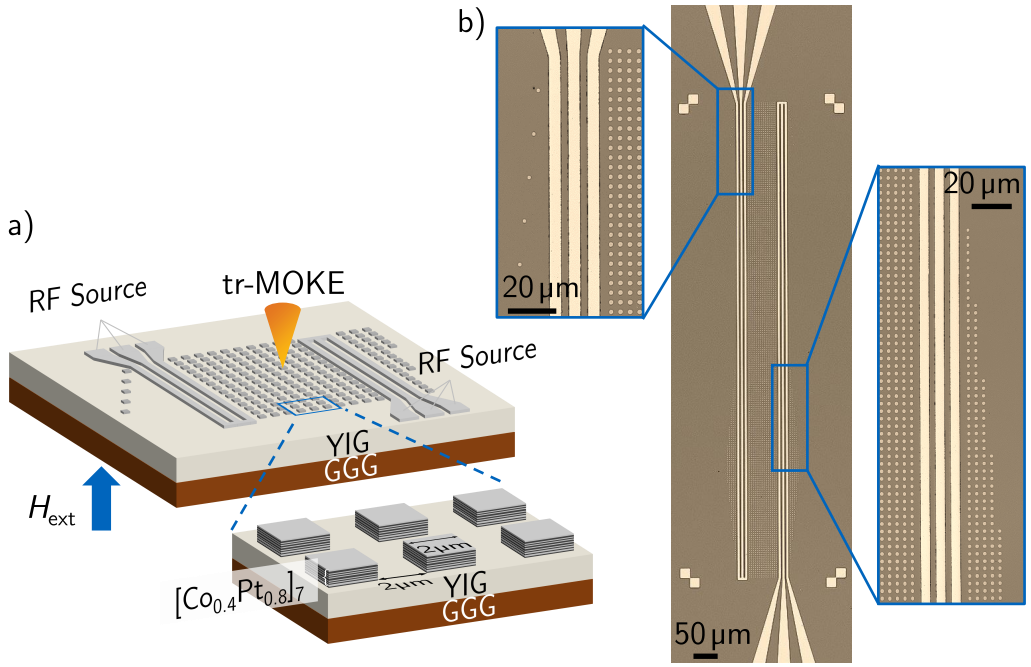

Figure 6.8: a) Schematic depictions of our PMA magnet test sample and the experimental setup for the tr-MOKE measurements. The zoom shows the composition and dimensions of the PMA nanomagnets consisting of a $[Co_{0.4}Pt_{0.8}]_7$ stack with a side length and edge-to-edge distance of 2 µm. b) Optical microscopy images of the test geometry utilizing two parallel transducers with gap and line widths of 4 µm. The zooms show the individual-magnet and step-like test geometries.

an edge-to-edge distance of each 2 µm. Figure 6.8b depicts optical microscopy images of the test sample, where the zoomed-in images show the individual nanomagnets and the step-like geometries. Note that the nanomagnets are not fabricated using a NIL method but via MLA-OL because it is easier to fabricate individual nanomagnets with OL. However, the fabrication method does not influence the properties of the nanomagnets.

Comparison between Experiment and Simulation

Our experiments with the nanomagnet test sample aim to evaluate the influence of the permanent magnets on the spin wave propagation in the YIG

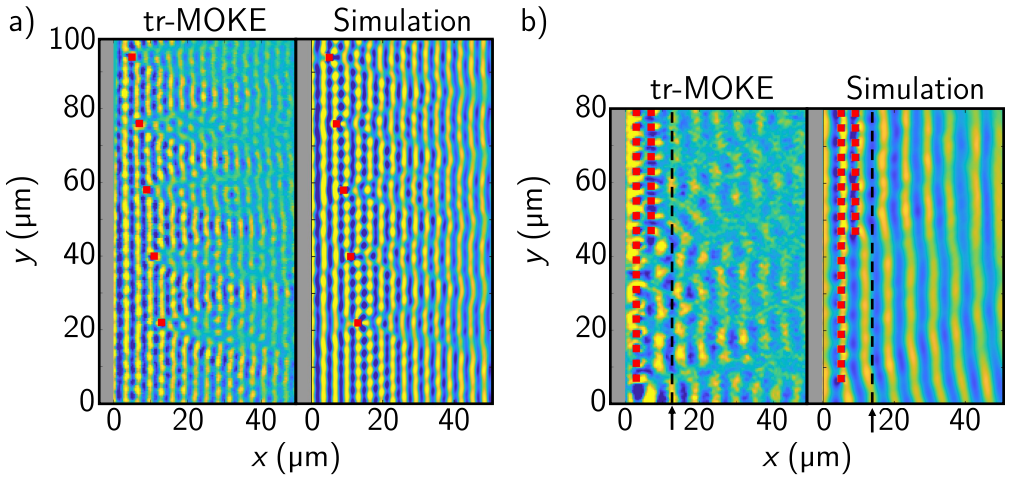

Figure 6.9: Color plots of experimental tr-MOKE data and simulations of a) individual nanomagnets and b) rows of nanomagnets. The red squares indicate the position of the nanomagnets in each plot.

film below. Furthermore, we want to compare the measured spin wave propagation with simulations of the propagation in the test geometries. All simulations are calculated MuMax [119]. A good agreement of the simulated and measured spin wave propagation is vital for designing and fabricating spin wave devices for neuromorphic computing applications [104].

First, we look at the individual nanomagnets on top of the YIG film. Figure 6.9a shows a tr-MOKE measurement of the spin wave propagation compared to the simulation. The measurement shows spin wave interference patterns behind the nanomagnets because the nanomagnets act as local spin wave scatterers. The interference pattern slightly changes from magnet to magnet as the phase of the spin wave at each magnet is different because of the different distances to the transducer. The simulation shows a comparable interference pattern. The main difference is the spin wave amplitude behind the nanomagnets. The higher amplitude in the simulation is likely caused by not perfectly adjusted initial simulation parameters, such as the magnets' actual magnetic field strength, and the fact that the simulation does not account for fabrication imperfections.

Next, we compare the step-like test structure's measured and simulated spin-wave propagation. Figure 6.9b shows the measured and simulated data

for the first two steps with one and two rows of nanomagnets. The dashed line in both plots emphasizes the occurring phase shift of the spin wave. In the tr-MOKE measurement, we recognized a phase shift of the spin wave depending on the number of nanomagnet rows. One nanomagnet row shifts the phase of the spin wave by about π and two rows by about 2π. The nanomagnets create an area of altered spin wave dispersion in the YIG below that alters the wavelength of the spin wave below the nanomagnets. The altered wavelength leads to a practical phase shift of the spin waves behind the nanomagnets compared to the undisturbed spin wave. The phase shift increases linearly with the number of nanomagnet rows.

The simulation also shows a phase shift caused by the nanomagnets. However, the observed phase shift is about half of the phase shift in the experiment. Thus, the measurement and the simulation show the same conceptional effect of the nanomagnet rows on the spin wave propagation. However, the strength of the influence differs. We assume a discrepancy between the actual field strength of the PMA nanomagnets and the assumed field strength in the simulation because the influence on the dispersion largely depends on perpendicular magnetic field strength. Therefore, the nanomagnet's actual field strength must be measured and implemented into the simulation to overcome this discrepancy. The inaccurate magnetic field strength could also explain the different spin wave amplitudes observed in Figure 6.9a.

Overall, the measurements show good agreement with the simulations, and after the adjustment of the initial parameters of the simulations, we expect a reliable agreement between the simulation and experiment. Hence, we showed that manipulating spin wave propagation is feasible using nanomagnetic patterns. However, the preliminary experiments only show the feasibility of spin wave manipulation with PMA magnets. Further steps must be taken to achieve a neuromorphic computing spin wave device. A final spin wave device calls for reconfigurable nanomagnet arrays, where the magnetization of magnets can be switched independently [104]. Reconfigurable nanomagnets can, for example, be achieved by changing the switching field of magnets via FIB irradiation [120]. Furthermore, an all-electrical characterization method must be implemented because the tr-MOKE cannot capture spin waves under the nanomagnet array. Therefore, a deeper understanding of excitation and detection of spin waves using CPW transducers is useful [102]. Last, as mentioned before, the simulations must be fed with precise system parameters to reliably design the spin wave devices. Never-

theless, we showed the first steps towards using PMA nanomagnets for spin wave manipulation, which future researchers can take as a starting point for fully implementing neuromorphic computing devices.

6.3 Patterning of Nanoimprinting Stamps

In the previous section, the nanomagnets for the test structures were fabricated using the MLA-OL process. We needed a specific pattern of nanomagnets, which made applying any NIL process not feasible, as with NIL, we can only produce the array defined by the imprinting stamp. Future devices need large-area nanomagnet arrays making NIL processes desirable again again. However, to ensure undisturbed spin wave excitation and detection, the transducers cannot be placed onto the nanomagnet array like in Figure 6.3. Therefore, we developed a method to macroscopically pattern imprinting stamps by removing pillars from the stamp. The free space in the imprinting stamp translates into free space in the nanomagnet array during imprinting. Later, the transducers can be placed into the free space using the alignment capabilities of the MLA. We refer to the new patterning method as the stamp patterning MLA-OL process.

6.3.1 The Stamp Patterning Optical Lithography Process

We introduce the stamp patterning MLA-OL process exemplarily for the fabrication of free space for spin wave transducers in a nanopillar array. Figure 6.10 schematically depicts the stamp patterning MLA-OL method. We start with a chromium nanoisland array on a SiO_2 substrate fabricated with the standard LO-NIL method described in Section 2.2.1. Before starting the OL process, the sample is cleaned using an ultrasonic bath in each DMSO, acetone, and isopropanol. Figure 6.10a shows the cleaned nanoisland array on top of the SiO_2. Next, we apply a photoactive resist via spin coating depicted in Figure 6.10b. After spin coating, we use the MLA to write the desired pattern into the photoresist. Note that the features of the stamp will be removed from the exposed areas. Figure 6.10c shows the exposed photoresist. Now, we use a suitable developer to wet chemically remove the exposed photoresist and to lay open the underlying chromium nanoislands depicted in Figure 6.10d. The inset of the figure shows the bare nanoislands.

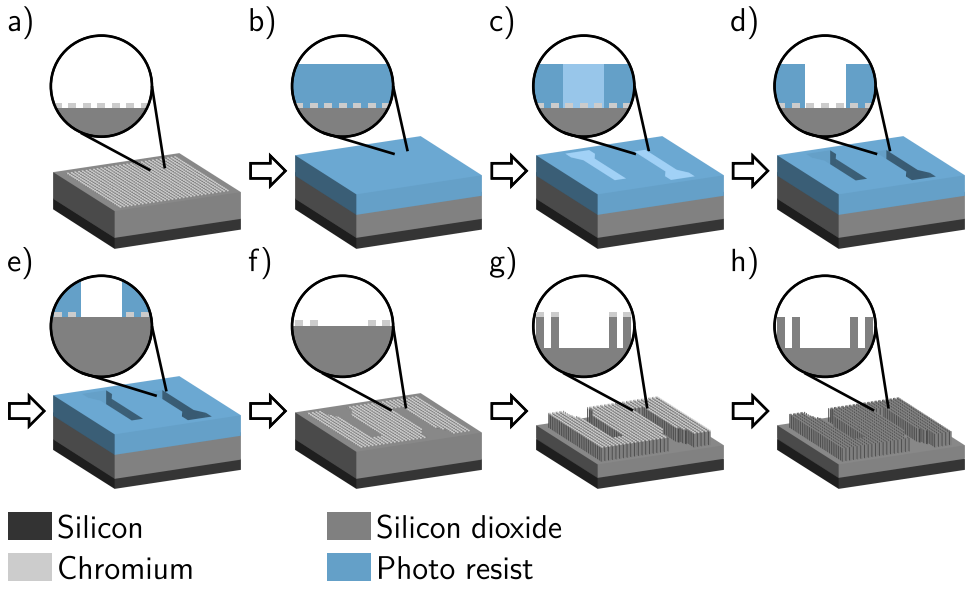

Figure 6.10: Schematic depiction of the stamp patterning MLA-OL process using an optical lithography process and a stamp replication process: a) A chromium nanoisland array is fabricated on a SiO_2 layer using the LO-NIL process. b) On top of the nanoisland array, a positive photoresist is spin coated. c) Using the MLA, the photoresist is exposed according to a predefined pattern. d) The sample is developed to remove the exposed resist. e) Subsequently, a chromium etchant removes the exposed chromium islands. The photoresist protects the remaining chromium islands. f) The remaining photoresist is removed from the sample. g) The pattern of the remaining chromium islands is transferred into the SiO_2 layer via an anisotropic dry etching process. h) Last, the remaining chromium is removed using chromium etchant. The new stamp can now be used as a template for the stamp production process.

To remove the uncovered chromium islands, we use a special chromium etchant that does not etch the photoresist protecting the covered chromium nanoislands from being removed. Figure 6.10e shows the sample after the removal of the uncovered chromium nanoislands, which can be seen in the inset of the figure. Next, the remaining photoresist is removed with a suitable remover, and the sample is cleaned in each acetone and isopropanol using an ultrasonic bath. Figure 6.10f shows the now patterned chromium nanoisland array.

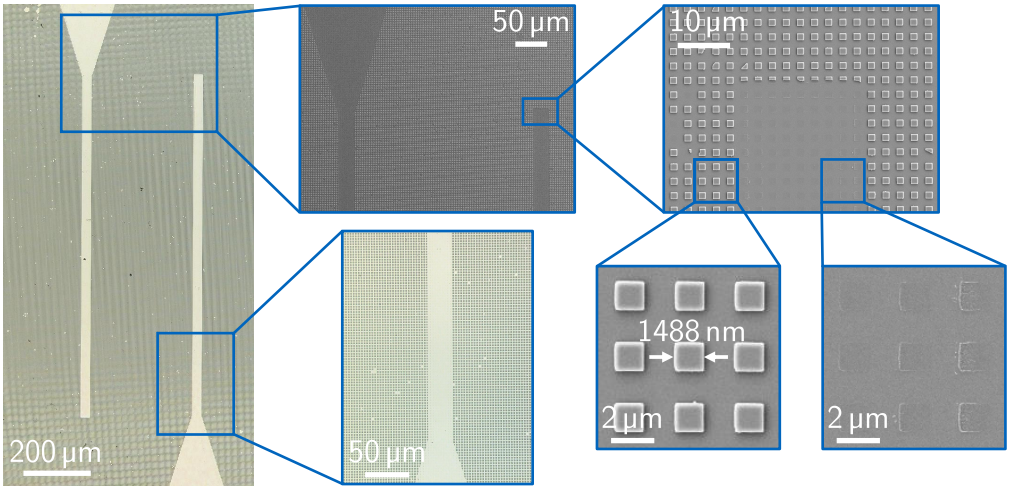

Figure 6.11: Optical microscopy images and SEM images of a SiO_2 stamp patterned with the stamp patterning MLA-OL method to generate space for the integration of spin wave transducers in the nanomagnet array. The SEM images show the alignment of the freed space compared to the stamp pillar array, the remaining nanopillars, and the pillar residuals in the freed space.

The chromium array is used as the mask for a RIE process to transfer the patterned nanoisland array into the SiO_2 substrate. Here, the same dry etching process is used that was used for the reproduction of the imprinting stamps during the chromium HF tuning method seen in Section 5.3. Figure 6.10g shows the sample after the dry etching of the SiO_2. Last, the chromium nanoislands are removed using chromium etchant again. The final stamp depicted in Figure 6.10h can be used in our imprinting processes and will produce a nanoisland array that leaves out the patterns we removed using the stamp patterning MLA-OL process.

Patterned Stamp for Spin Wave Transducers

We fabricated a 1400 nm SiO_2 stamp with free space for CPWs using the stamp patterning MLA-OL process; the process parameters are listed in Appendix A.6. Figure 6.11 shows optical microscopy and SEM images of the stamp. The SEM images were taken with a second electron (SE) detector to emphasize the stamp's topography. The optical overview image shows the imprinting stamp with newly fabricated free space for two parallel CPWs.

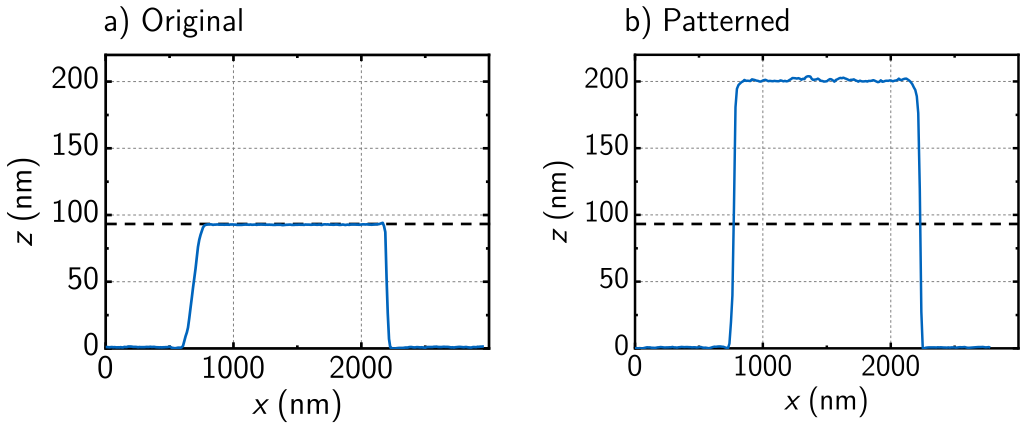

Figure 6.12: AFM height profiles of a nanopillar of a) the original 1400 nm stamp and b) the patterned 1400 nm stamp. The black dashed line indicates the height of the original 1400 nm stamp in each graph.

The zoomed-in optical microscopy image and the SEM image in the second column show the alignment of the transducers to the stamp pillars; the CPWs must run parallel to the cubic lattice of the nanoisland array for future application.

The zoomed-in SEM images at the right allow the analysis of individual structures of the stamp. The top image shows the end of the CPW region, where the last row of nanopillars got split in the middle. The smooth edge of the split nanoislands indicates the precision of the patterning process. In the same SEM image, some nanopillars are missing in the array, which we attribute to an imperfect LO-NIL process while fabricating the initial chromium nanoisland array. We measure a side length of 1488(15) nm for the nanopillars of the patterned stamp, which is more than the 1412(16) nm of the master stamp, which agrees with the behavior of reproduced SiO_2 stamps we fabricated in the previous chapter. The zoom onto the freed space reveals visible residues of the removed nanostructures, which we attribute to residual chromium after the lift-off influencing the dry etching process. However, the residues will not influence the imprinting process using the stamp as their height is insignificant compared to the stamp pillars.

Furthermore, we took AFM images of the stamp pillars to check for a sufficient pillar height of the new stamp for nanoimprinting. Figure 6.12

shows AFM height profiles for the original and patterned stamps. Here, the dashed black line indicates the height of the original stamp of 93 nm, sufficient for the LO-NIL process. The height of 200 nm of the patterned stamp significantly exceeds the original stamp pillar height. Therefore, there are no concerns about the height of the patterned stamp regarding its successful application in imprinting processes.

Overall, the stamp patterning MLA-OL method enables the fabrication of patterned nanoimprinting stamps, which enables the integration of nanoimprinted arrays and microsized structures fabricated with suitable fabrication techniques like MLA-OL. So, we overcome the limitations of NIL in terms of fabricating structures exceeding a few micrometers and further extend the application possibilities of our nanoimprinting processes.

Chapter 7

Conclusion, Key Advances, and Outlook

This work aimed to advance NIL starting from the LO-NIL process previously developed in our group to customize the fabricated nanoimprinted samples to the experimental requirements of our research partners. Every experimental setup has requirements for the examined sample and prerequisites for used materials, geometries, and structures. We adopted our NIL processes to the challenges arising from the application in various research fields, from electrochemistry over photonics and plasmonics to spin wave computing. We have maintained the unique properties of NIL in each of our processes, including large-area nanopatterning, nanometer precision, and cost- and time-effective sample fabrication. It is worth mentioning that the fanciest and most elegant nanoimprinting process has no meaningful impact if not used in an experiment or application. Furthermore, we managed to diversify the portfolio of imprinting techniques, which enabled or accelerated the research of our cooperation partners. In the following, we summarize the key advances of NIL developed in this work and emphasize their impact on the research of our cooperation partners.

Metal Nanoisland Arrays Embedded in an Insulator Passivation Layer to Increase HER Activity

We expanded the LO-NIL process to incorporate the embedment of our nanostructures into an insulator layer added to the substrate. That way, the metal nanoislands are still conducted to the substrate, so the embedment does not influence the electrical properties of the nanoislands. However, the insulator layer passivates the substrate surface against the electrolyte and

introduces a metal/Insulator interface at the edges of the nanoislands. The newly formed interface facilitates a bifunctional effect, which increases the HER activity of the edge region of gold nanoislands. The HER activity of the embedded gold nanoislands can therefore be enhanced by increasing the edge-to-bulk ratio by reducing the size of the gold nanoislands [57].

Directly Patterned Semiconductors for Enhanced Light Harvesting Properties

We developed a NIL process to directly nanopattern the surface of a semiconductor substrate instead of depositing the nanostructures via LO-NIL. Here, we use inverted imprinting stamps to fabricate imprint resist pillars on top of the sample, which are used as an etching mask for patterning the sample surface. In this way, we can pattern materials that are not evaporable and, therefore, cannot be deposited in LO-NIL processes. The direct patterning of GaP allows the fabrication of a metasurface with supreme light-harvesting capabilities over the whole solar spectrum utilizing anapole excitations and lattice resonance to enhance the absorption of the metasurface for light energies below the absorption edge of GaP [78].

Tuning the Feature Sizes of Nanoimprinting Stamps to Increase the Versatility of NIL

We developed an imprinting stamp replication and tuning process to stepless tune the feature sizes of our imprinting stamps. Utilizing nanoimprinting chromium nanoislands as a RIE hard mask, we first reproduce our original imprinting stamps to subsequently tune the feature sizes of the reproduced stamps using isotropic HF etching. The reproduced and tuned stamps can then be used as new originals for all our NIL processes to fabricate nanoislands with the tuned dimensions. Furthermore, the stepless tunability of the nanoisland dimensions allows us to tailor the properties of the nanoisland arrays according to each experiment and application without the need for a new expensive original stamp. Exemplarily, we tuned the plasmonic resonance of our nanoisland arrays to shift the plasmonic response in the visible light regime [55].

Integration of Microstructures into Nanoimprinted Arrays

We developed a method to pattern the nanopillar arrays of our nanoimprinting stamps to leave nanostructure-free space in the nanoimprinted arrays fabricated with these stamps. Microstructures can then be incorporated into the freed space using optical lithography. The integration of micro- and nanostructured features on one sample enables the incorporation of NIL techniques into the fabrication of existing and new devices. We showed proof of concept measurements for manipulating spin waves using PMA nanomagnets. Nanoimprinted arrays of such nanomagnets can build the backbone of neuromorphic computing devices powered by micro-sized spin wave transducers integrated into the imprinted nanomagnet array [104].

The capabilities of NIL are far from exhausted. Future work on nanoimprinting techniques should aim to further spread the technology to more research fields and users. The large-area patterning and low-cost nature of NIL processes make them promising for use wherever reproducible nanostructures are needed to accelerate research and improve devices.

So far, we have focused on fabricating regular arrays of identical nanoislands. In the future, more arbitrary arrangements of nanostructures should be considered for NIL. The advancement of e-beam lithography processes reduces the cost and time expenses of fabrication, thus offering more affordable imprinting stamps. A combination of custom-made imprinting stamps and custom NIL processes then enables further adaption to the experimental needs of each application.

Furthermore, we recently started cooperation with Howe Simpson and Frank Hegmann from the University of Alberta and Natalie Fehn from the Technical University of Munich. In the first cooperation, we provide metal nanoisland arrays to study the ultrafast dynamics of Schottky diodes via terahertz scanning tunneling microscopy (THz STM). For the second cooperation, we provide nanoimprinted samples utilizing the plasmonic resonance of a gold nanoisland array for chemical applications. Both cooperations show promising preliminary results and are an excellent opportunity to enable successful research through nanoimprinted samples. Increasing the awareness of NIL technologies in the scientific community leads to inspiration for further advances in the field of nanoimprinting. Furthermore, it can accelerate research due to the unique benefits of nanoimprint lithography.

Appendix A

Experimental Parameters

A.1 Chemicals

Table A.1: Chemicals used for the processes presented in this work.

Name	Process	Function	Company
OrmoPrime08	Stamp replication	Primer	micro resist
OrmoStamp	Stamp replication	Stamp polymer	micro resist
PMGI SF6	LO-NIL	Lift-off resist	Kayaku AM
T-thinner	LO-NIL	Lift-off thinner	Kayaku AM
mr-I8020R	LO-NIL	Imprint resist	micro resist
ma-T 1050	LO-NIL	Imprint thinner	micro resist
AZ 400K	LO-NIL	Developer	MicroChemicals
m-Rem 700	LO-NIL	Remover	micro resist
BOE 49:1	HF tuning	HF Etchant	Technic
Cr etchant	HF tuning	Cr etchant	Merck
AZ 5214E	MLA-OL	Photoresist	MicroChemicals
AZ 351B	MLA-OL	Developer	MicroChemicals
AZ 100 Rem	MLA-OL	Remover	MicroChemicals
ma-N 1407	MLA-OL CoPt	Photoresist	micro resist
ma-D 533/S	MLA-OL CoPt	Developer	micro resist

A.2 Substrates

Table A.2: Substrates used for the processes presented in this work.

Process	Substrate	Company
Master Stamps	2″ fused silica JGS2 wafer	MicroChemicals
Master Stamps	25 × 25 mm Menzel glass	Gerhard Menzel
Working Stamps	18 mm cover glasses	VWR
LO-NIL	(100) p-doped silicon	MicroChemicals
Embedded LO-NIL	(111) n-doped silicon	Sil'tronix Silicon
Direct etching NIL	Amorphous GaP	Sputtered at LMU
Stamp tuning	(100) silicon + 200 nm SiO_2	Micro Chemicals
Tuned arrays	(100) p-doped silicon	MicroChemicals
Tuned arrays	2″ fused silica JGS2 wafer	MicroChemicals
MLA-OL	GGG	Saint Gobain
MLA-OL	YIG	Sputtered at TUM

A.3 O_2 Plasma Parameters

Table A.3: Process parameters for the plasma asher for cleaning and surface activation.

Process	Power	Time
Silicon cleaning/activation	200 W	2 min
Glass substrate activation	600 W	6 min
OrmoStamp ASL activation	100 W	1 min

A.4 Stamp Replication Parameters

Table A.4: OrmoPrime spin coating parameters.

Chemical	Spin coating (rpm/time)	Post Bake (temp/time)	Thickness
OrmoPrime08	3000/30 s	150 °C/3 min	150 nm

Table A.5: Process parameters for the OrmoStamp replication process.

Stamp	Substrate	OrmoStamp	Exposure
Master 1400	2″ fused silica wafer	80 µL	350 W/2 min
Master 350	2″ fused silica wafer	80 µL	350 W/2 min
Master 200	2″ fused silica wafer	80 µL	350 W/2 min
Master 75	25 × 25 mm glass slide	4 µL	350 W/2 min
Master 45	2″ silica wafer	80 µL	350 W/2 min
Master direct	25 × 25 mm glass slide	4 µL	350 W/2 min
Working 1400	18 mm cover glasses	6 µL	350 W/2 min
Working 350	18 mm cover glasses	6 µL	350 W/2 min
Working 200	18 mm cover glasses	6 µL	350 W/2 min
Working 75	18 mm cover glasses	8 µL	350 W/2 min
Working 45	18 mm cover glasses	6 µL	350 W/2 min
Working direct	18 mm cover glasses	8 µL	350 W/2 min

Table A.6: OmroStamp working stamp hot plate annealing parameters.

Temperature	Time
130 °C	30 min

A.5 Imprinting Parameters

LO-NIL and Embedded LO-NIL

Table A.7: Lift-off resist (PNGI SF6 : T-thinner) spin coating parameters for the LO-NIL and embedded LO-NIL process.

Feature size	Dilution	Spin coating (rpm/time)	Post Bake (temp/time)	Thickness
1400 nm	1:2	4000/45 s	250 °C/3 min	50 nm
350 nm	1:2	4000/45 s	250 °C/3 min	50 nm
200 nm	1:2	4000/45 s	250 °C/3 min	50 nm
75 nm	1:2	6000/45 s	250 °C/3 min	40 nm
45 nm	1:2	6000/45 s	250 °C/3 min	40 nm

Table A.8: Imprint resist (mr-I8020R : ma-T 1050) spin coating parameters for the LO-NIL and embedded LO-NIL process.

Feature size	Dilution	Spin coating (rpm/time)	Post Bake (temp/time)	Thickness
1400 nm	1:1	3600/30 s	100 °C/1 min	70 nm
350 nm	undil.	5500/30 s	100 °C/1 min	150 nm
200 nm	1:1	4000/30 s	100 °C/1 min	70 nm
75 nm	1:1	4000/30 s	100 °C/1 min	70 nm
45 nm	1:1.5	4400/30 s	100 °C/1 min	50 nm

Table A.9: Thermal imprinting process parameters for the LO-NIL and embedded LO-NIL process.

Feature size	Feature shape	Pressure	Temperature	Time
1400 nm	squares	30 bar	165 °C	3 min
350 nm	squares	30 bar	165 °C	3 min
200 nm	squares	30 bar	165 °C	3 min
75 nm	circles	30 bar	165 °C	3 min
45 nm	circles	30 bar	165 °C	3 min

Table A.10: RIE parameters for the residual layer etching.

O_2 flow	C_4F_8 flow	RF power	ICP power	Pressure	dc bias
25 sccm	27 sccm	200 W	–	30 mtorr	520 V

Table A.11: Process parameters for the residual layer etching for the LO-NIL and the embedded LO-NIL process.

Feature size	Etching time	O_2 flash	Etch rate	Etch depth
1400 nm	10 s	5 s	2.0 nm s^{-1}	30 nm
350 nm	10 s	5 s	2.0 nm s^{-1}	30 nm
200 nm	10 s	5 s	2.0 nm s^{-1}	30 nm
75 nm	12 s	5 s	2.0 nm s^{-1}	34 nm
45 nm	12 s	5 s	2.0 nm s^{-1}	34 nm

Table A.12: Process parameters for the lift-off resist underetching for the LO-NIL and the embedded LO-NIL process.

Feature size	Dilution	Etch rate	Duration	Di stop
1400 nm	1:5	0.78 nm s^{-1}	40 s	10 s
350 nm	1:5	0.78 nm s^{-1}	30 s	10 s
200 nm	1:5	0.78 nm s^{-1}	30 s	10 s
75 nm	1:5	0.78 nm s^{-1}	15 s	10 s
45 nm	1:5	0.78 nm s^{-1}	10 s	10 s

Table A.13: RIE parameters for anisotropic SiO_2 etching.

O_2 flow	C_4F_8 flow	RF power	ICP power	Pressure	dc bias
2 sccm	18 sccm	100 W	150 W	13 mtorr	415 V

Table A.14: RIE process parameters for the SiO_2 etching process for the embedded LO-NIL process.

Feature size	Etching time	O_2 flash	Etch rate	Etch depth
1400 nm	15 s	5 s	1.0 nm s^{-1}	15 nm
350 nm	15 s	5 s	1.0 nm s^{-1}	15 nm
200 nm	15 s	5 s	1.0 nm s^{-1}	15 nm
75 nm	15 s	5 s	1.0 nm s^{-1}	15 nm
tun. SiO_2	120 s	5 s	0.8 nm s^{-1}	100 nm

Direct etching NIL

Table A.15: Imprint resist (mr-I8020R : ma-T 1050) spin coating parameters for the direct etching NIL process.

Feature size	Dilution	Spin coating (rpm/time)	Post Bake (temp/time)	Thickness
200 nm (dir.)	1:1	6000/30 s	100 °C/1 min	55 nm

Table A.16: Thermal imprinting process parameters.

Feature size	Feature shape	Pressure	Temperature	Time
200 nm (dir.)	inv. circles	30 bar	165 °C	3 min

Resist Tuning process

Table A.17: Imprint resist (mr-I8020R : ma-T 1050) spin coating parameters for the resist tuning process.

Tuning time	Dilution	Spin coating (rpm/time)	Post Bake (temp/time)	Thickness
60 s	undil.	6000/30 s	100 °C/1 min	151 nm
90 s	undil.	6000/30 s	100 °C/1 min	151 nm
120 s	undil.	3000/30 s	100 °C/1 min	211 nm
150 s	undil.	3000/30 s	100 °C/1 min	211 nm
190 s	undil.	2000/30 s	100 °C/1 min	263 nm
230 s	undil.	1000/30 s	100 °C/1 min	368 nm
270 s	undil.	1000/30 s	100 °C/1 min	368 nm

Table A.18: Thermal imprinting process parameters for the inverse 200 nm stamp for the resist tuning process.

Tuning time	Feature shape	Pressure	Temperature	Time
60 s	inv. squares	30 bar	165 °C	3 min
90 s	inv. squares	30 bar	165 °C	3 min
120 s	inv. squares	30 bar	165 °C	3 min
150 s	inv. squares	30 bar	165 °C	3 min
190 s	inv. squares	30 bar	165 °C	3 min
230 s	inv. squares	30 bar	165 °C	3 min
270 s	inv. squares	30 bar	165 °C	3 min

Table A.19: RIE parameters for the isotropic imprint resist etching.

O_2 flow	C_4F_8 flow	RF power	ICP power	Pressure	dc bias
30 sccm	–	35 W	–	30 mtorr	

Table A.20: RIE process parameters for the tuning process.

Tuning time	Etching time	O_2 flash	Etch rate	Etch depth
60 s	60 s	–	1.2 nm s^{-1}	75 nm
90 s	90 s	–	1.3 nm s^{-1}	101 nm
120 s	120 s	–	1.3 nm s^{-1}	154 nm
150 s	150 s	–	1.3 nm s^{-1}	194 nm
190 s	190 s	–	1.3 nm s^{-1}	242 nm
230 s	230 s	–	1.3 nm s^{-1}	300 nm
270 s	270 s	–	1.3 nm s^{-1}	350 nm

Table A.21: RIE parameters for anisotropic SiO_2 etching.

O_2 flow	C_4F_8 flow	RF power	ICP power	Pressure	dc bias
2 sccm	18 sccm	100 W	150 W	13 mtorr	415 V

Table A.22: RIE process parameters for the SiO_2 etching process.

Tuning time	Etching time	O_2 flash	Etch rate	Etch depth
60 s	170 s	5 s	1.1 nm s^{-1}	187 nm
90 s	158 s	5 s	1.1 nm s^{-1}	175 nm
120 s	158 s	5 s	1.1 nm s^{-1}	175 nm
150 s	120 s	5 s	1.1 nm s^{-1}	128 nm
190 s	120 s	5 s	1.1 nm s^{-1}	128 nm
230 s	158 s	5 s	1.1 nm s^{-1}	175 nm
270 s	158 s	5 s	1.1 nm s^{-1}	175 nm

Resist HF Tuning process

Table A.23: Imprint resist (mr-I8020R : ma-T 1050) spin coating parameters for the resist HF tuning process.

Feature size	Dilution	Spin coating (rpm/time)	Post Bake (temp/time)	Thickness
inv 200 nm	1:1	4000/30 s	100 °C/1 min	73 nm
inv 350 nm	undil.	6000/30 s	100 °C/1 min	182 nm

Table A.24: Thermal imprinting process parameters for the resist HF tuning process.

Feature size	Feature shape	Pressure	Temperature	Time
inv. 200 nm	inv. squares	30 bar	165 °C	3 min
inv. 350 nm	inv. squares	30 bar	165 °C	3 min

Table A.25: RIE parameters for anisotropic SiO_2 etching.

O_2 flow	C_4F_8 flow	RF power	ICP power	Pressure	dc bias
2 sccm	18 sccm	100 W	150 W	13 mtorr	415 V

Table A.26: RIE process parameters for the SiO_2 etching process.

Feature size	Etching time	O_2 flash	Etch rate	Etch depth
inv 200 nm	135 s	5 s	1.1 nm s^{-1}	149 nm
inv 350 nm	305 s	5 s	1.1 nm s^{-1}	335 nm

Table A.27: Process parameters for the SiO_2 HF tuning of the 200 nm stamp.

Tuning time	Di stop	Tuning rate	Tuning difference
20 s	30 s	0.50 nm s^{-1}	20 nm
60 s	30 s	0.37 nm s^{-1}	44 nm
100 s	30 s	0.26 nm s^{-1}	51 nm
230 s	30 s	0.20 nm s^{-1}	91 nm
285 s	30 s	0.18 nm s^{-1}	102 nm
340 s	30 s	0.17 nm s^{-1}	116 nm
400 s	30 s	0.17 nm s^{-1}	139 nm
455 s	30 s	0.15 nm s^{-1}	137 nm

Table A.28: Process parameters for the SiO_2 HF tuning of the 350 nm stamp.

Tuning time	Di stop	Tuning rate	Tuning difference
450 s	30 s	0.19 nm s^{-1}	171 nm
500 s	30 s	0.21 nm s^{-1}	205 nm
550 s	30 s	0.20 nm s^{-1}	216 nm
600 s	30 s	0.19 nm s^{-1}	231 nm

Table A.29: Lift-off resist (PNGI SF6 : T-thinner) spin coating parameters for the fabrication of nanoisland arrays using the tuned 200 nm and 350 nm stamps.

Feature size	Dilution	Spin coating (rpm/time)	Post Bake (temp/time)	Thickness
tun. 200 nm	1:2	6000/45 s	250 °C/3 min	40 nm
tun. 350 nm	1:2	4000/45 s	250 °C/3 min	50 nm

Table A.30: Imprint resist (mr-I8020R : ma-T 1050) spin coating parameters for the fabrication of nanoisland arrays using the tuned 200 nm and 350 nm stamps.

Feature size	Dilution	Spin coating (rpm/time)	Post Bake (temp/time)	Thickness
tun. 200 nm	1:1	6000/30 s	100 °C/1 min	50 nm
tun. 350 nm	1:1	2000/30 s	100 °C/1 min	112 nm

Table A.31: Thermal imprinting process parameters for the fabrication of nanoisland arrays using the tuned 200 nm and 350 nm stamps.

Feature size	Feature shape	Pressure	Temperature	Time
tun. 200 nm	squares	30 bar	165 °C	3 min
tun. 350 nm	squares	30 bar	165 °C	3 min

Table A.32: RIE parameters for the residual layer etching.

O_2 flow	C_4F_8 flow	RF power	ICP power	Pressure	dc bias
25 sccm	27 sccm	200 W	–	30 mtorr	520 V

Table A.33: Process parameters for the residual layer etching for the fabrication of nanoisland arrays using the tuned 200 nm and 350 nm stamps.

Feature size	Etching time	O_2 flash	Etch rate	Etch depth
tun. 200 nm	8 s	5 s	2.0 nm s^{-1}	26 nm
tun. 350 nm	10 s	5 s	2.0 nm s^{-1}	30 nm

Table A.34: Process parameters for the lift-off resist underetching for the fabrication of nanoisland arrays using the tuned 200 nm and 350 nm stamps.

Feature size	Dilution	Etch rate	Duration	Di stop
tun. 200 nm	1:5	0.78 nm s^{-1}	100 s	10 s
tun. 350 nm	1:5	0.78 nm s^{-1}	65 s	10 s

Chromium HF Tuning process

Table A.35: Lift-off resist (PMGI SF6 : T-thinner) spin coating parameters for the LO-NIL of the chromium islands.

Feature size	Dilution	Spin coating (rpm/time)	Post Bake (temp/time)	Thickness
75 nm	1:2	6000/45 s	250 °C/3 min	40 nm

Table A.36: Imprint resist (mr-I8020R : ma-T 1050) spin coating parameters for the LO-NIL of the chromium islands.

Feature size	Dilution	Spin coating (rpm/time)	Post Bake (temp/time)	Thickness
75 nm	1:1	4000/30 s	100 °C/1 min	70 nm

Table A.37: Thermal imprinting process parameters for the LO-NIL of the chromium islands.

Feature size	Feature shape	Pressure	Temperature	Time
75 nm	circles	30 bar	165 °C	3 min

Table A.38: RIE parameters for the residual layer etching.

O_2 flow	C_4F_8 flow	RF power	ICP power	Pressure	dc bias
25 sccm	27 sccm	200 W	–	30 mtorr	520 V

Table A.39: Process parameters for the residual layer etching for the LO-NIL of the chromium islands.

Feature size	Etching time	O_2 flash	Etch rate	Etch depth
75 nm	12 s	5 s	2.0 nm s^{-1}	34 nm

Table A.40: Process parameters for the lift-off resist underetching for the LO-NIL of the chromium islands.

Feature size	Dilution	Etch rate	Duration	Di stop
75 nm	1:5	0.78 nm s^{-1}	15 s	10 s

Table A.41: RIE parameters for anisotropic SiO_2 etching.

O_2 flow	C_4F_8 flow	RF power	ICP power	Pressure	dc bias
2 sccm	18 sccm	100 W	150 W	13 mtorr	415 V

Table A.42: RIE process parameters for the SiO_2 etching process for the stamp reproduction process using the chromium hard mask.

Feature size	Etching time	O_2 flash	Etch rate	Etch depth
75 nm	120 s	5 s	0.8 nm s^{-1}	100 nm

Table A.43: Process parameters for the SiO_2 HF tuning of the 200 nm stamp.

Tuning time	Di stop	Tuning rate	Tuning difference
30 s	30 s	0.18 nm s^{-1}	11 nm
60 s	60 s	0.20 nm s^{-1}	24 nm
90 s	90 s	0.21 nm s^{-1}	37 nm

Table A.44: Lift-off resist (PNGI SF6 : T-thinner) spin coating parameters for the fabrication of nanoisland arrays using the tuned 75 nm stamps.

Feature size	Dilution	Spin coating (rpm/time)	Post Bake (temp/time)	Thickness
ORGarray	1:2	6000/45 s	250 °C/3 min	40 nm
REParray	1:2	6000/45 s	250 °C/3 min	40 nm
30HFarray	1:2	6000/45 s	250 °C/3 min	40 nm
60HFarray	1:2	6000/45 s	250 °C/3 min	40 nm
90HFarray	1:2	6000/45 s	250 °C/3 min	40 nm

Table A.45: Imprint resist (mr-I8020R : ma-T 1050) spin coating parameters for the fabrication of nanoisland arrays using the tuned 75 nm stamps.

Feature size	Dilution	Spin coating (rpm/time)	Post Bake (temp/time)	Thickness
ORGarray	1:2	3400/30 s	100 °C/1 min	71 nm
REParray	1:2	4000/30 s	100 °C/1 min	67 nm
30HFarray	1:2	3700/30 s	100 °C/1 min	69 nm
60HFarray	1:2	3700/30 s	100 °C/1 min	69 nm
90HFarray	1:2	3400/30 s	100 °C/1 min	71 nm

Table A.46: Thermal imprinting process parameters for the fabrication of nanoisland arrays using the tuned 75 nm stamps.

Feature size	Feature shape	Pressure	Temperature	Time
ORGarray	circles	30 bar	165 °C	3 min
REParray	circles	30 bar	165 °C	3 min
30HFarray	circles	30 bar	165 °C	3 min
60HFarray	circles	30 bar	165 °C	3 min
90HFarray	circles	30 bar	165 °C	3 min

Table A.47: RIE parameters for the residual layer etching.

O_2 flow	C_4F_8 flow	RF power	ICP power	Pressure	dc bias
25 sccm	27 sccm	200 W	–	30 mtorr	520 V

Table A.48: Process parameters for the residual layer etching for the fabrication of nanoisland arrays using the tuned 75 nm stamps.

Feature size	Etching time	O_2 flash	Etch rate	Etch depth
ORGarray	12 s	5 s	2.0 nm s^{-1}	34 nm
REParray	12 s	5 s	2.0 nm s^{-1}	34 nm
30HFarray	12 s	5 s	2.0 nm s^{-1}	34 nm
60HFarray	12 s	5 s	2.0 nm s^{-1}	34 nm
90HFarray	12 s	5 s	2.0 nm s^{-1}	34 nm

Table A.49: Process parameters for the lift-off resist underetching for the fabrication of nanoisland arrays using the tuned 75 nm stamps.

Feature size	Dilution	Etch rate	Duration	Di stop
ORGarray	1:5	0.78 nm s^{-1}	12 s	10 s
REParray	1:5	0.78 nm s^{-1}	12 s	10 s
30HFarray	1:5	0.78 nm s^{-1}	12 s	10 s
60HFarray	1:5	0.78 nm s^{-1}	12 s	10 s
90HFarray	1:5	0.78 nm s^{-1}	12 s	10 s

A.6 Optical Lithography

Table A.50: Spin coating parameters for the OL processes.

Process	Resist	Spin coating (rpm/time)	Post Bake (temp/time)	Thickness
MLA-OL	AZ 5214E	5000/40 s	100 °C/3 min	1.25 µm
CoPt-OL	ma-N 1407	4000/60 s	100 °C/1 min	700 nm
Patterning MLA-OL	AZ 5214E	5000/40 s	100 °C/3 min	1.25 µm

Table A.51: MLA parameters for the OL processes

Process	Resist	Substrate	Dose	Defoc
MLA-OL	AZ 5214E	YIG	150 mJ/cm^2	0
MLA-OL	AZ 5214E	Si	140 mJ/cm^2	0
CoPt-OL	AZ 5214E	CoPt	140 mJ/cm^2	-2
CoPt-OL	ma-N 1407	CoPt	140 mJ/cm^2	-6
Patterning MLA-OL	AZ 5214E	Cr on Si	140 mJ/cm^2	-2

Table A.52: Development parameters for the OL processes.

Resist	Developer	Dilution	Duration	Di stop
AZ 5214E	AZ 351B	1:4	18 s	10 s
ma-N 1407	ma-D 533/S	undil.	40 s	60 s

A.7 Metal Deposition

Table A.53: Process parameters for metal deposition.

Process	Material	Deposition rate	Thickness
LO-NIL	Ti/Au	1.2 Å s^{-1}/2.0 Å s^{-1}	3 nm/11 nm
Back contact	Al	3.0 Å s^{-1}	150 nm
emb. LO-NIL	Ti/Au	1.2 Å s^{-1}/2.0 Å s^{-1}	3 nm/12 nm
Tuning mask	Cr	1.2 Å s^{-1}	20 nm
Tuned islands	Ti/Au	1.2 Å s^{-1}/2.0 Å s^{-1}	3 nm/17 nm
Transducer	Al	3.0 Å s^{-1}	300 nm
CoPt mask	Ti	1.2 Å s^{-1}	3 nm

Bibliography

[1] F. Rahman, *Nanostructures in Electronics and Photonics*. New York: Pan Stanford, 2008, ISBN: 9780429066030, DOI: 10.1201/b11137.

[2] C. Gontrand, *Micro-nanoelectronics Devices*. ISTE Press - Elsevier, 2018, ISBN: 9781785482823, URL: https://www.elsevier.com/books/micro-nanoelectronics-devices/gontrand/978-1-78548-282-3.

[3] G. C. Hadjipanayis and G. A. Prinz, Eds., *Science and Technology of Nanostructured Magnetic Materials* (NATO ASI Series). Boston, MA: Springer US, 1991, vol. 259, ISBN: 978-1-4899-2592-3, DOI: 10.1007/978-1-4899-2590-9.

[4] D. Sellmyer and R. Skomski, Eds., *Advanced Magnetic Nanostructures*. Boston, MA: Springer US, 2006, pp. 1–11, ISBN: 978-0-387-23309-3, DOI: 10.1007/b101199.

[5] M. Yoda, J.-L. Garden, O. Bourgeois, *et al.*, "Nanostructures for Photonics", in *Encycl. Nanotechnol.* Dordrecht: Springer Netherlands, 2012, pp. 1813–1828, DOI: 10.1007/978-90-481-9751-4_235.

[6] L. Reyes Pires Kassab and C. Bartolomeu De Araujo, Eds., *Metal Nanostructures for Photonics*. Elsevier, 2018, ISBN: 9780081023785, URL: https://www.elsevier.com/books/metal-nanostructures-for-photonics/pires-kassab/978-0-08-102378-5.

[7] A. Eftekhari, Ed., *Nanostructured Materials in Electrochemistry*. Wiley, 2008, ISBN: 9783527318766, DOI: 10.1002/9783527621507.

[8] E. R. Leite, Ed., *Nanostructured Materials for Electrochemical Energy Production and Storage* (Nanostructure Science and Technology). Boston, MA: Springer US, 2009, ISBN: 978-0-387-49322-0, DOI: 10.1007/978-0-387-49323-7.

[9] "Solar", in *Handb. Energy*, C. J. Cleveland and C. Morris, Eds., Elsevier, 2013, pp. 405–450, DOI: 10.1016/B978-0-08-046405-3.00010-3.

[10] C. Lienau, M. A. Noginov, and M. Lončar, "Light–matter interactions at the nanoscale", *J. Opt.*, vol. 16, no. 11, p. 110 201, 2014, ISSN: 2040-8978, DOI: 10.1088/2040-8978/16/11/110201.

[11] H. Yu, Y. Peng, Y. Yang, and Z.-Y. Li, "Plasmon-enhanced light–matter interactions and applications", *npj Comput. Mater.*, vol. 5, no. 1, p. 45, 2019, ISSN: 2057-3960, DOI: 10.1038/s41524-019-0184-1.

[12] Y. Pan, X. Shen, L. Yao, A. Bentalib, and Z. Peng, "Active Sites in Heterogeneous Catalytic Reaction on Metal and Metal Oxide: Theory and Practice", *Catalysts*, vol. 8, no. 10, p. 478, 2018, ISSN: 2073-4344, DOI: 10.3390/catal8100478.

[13] B. Ni and X. Wang, "Face the Edges: Catalytic Active Sites of Nanomaterials", *Adv. Sci.*, vol. 2, no. 7, p. 1 500 085, 2015, ISSN: 21983844, DOI: 10.1002/advs.201500085.

[14] G. E. Moore, "Cramming more components onto integrated circuits, Reprinted from Electronics, volume 38, number 8, April 19, 1965, pp.114 ff.", *IEEE Solid-State Circuits Soc. Newsl.*, vol. 11, no. 3, pp. 33–35, 2006, ISSN: 1098-4232, DOI: 10.1109/N-SSC.2006.4785860.

[15] S. Y. Chou, "Nanoimprint lithography", *J. Vac. Sci. Technol. B Microelectron. Nanom. Struct.*, vol. 14, no. 1996, p. 4129, 1996, ISSN: 0734211X, DOI: 10.1116/1.588605.

[16] P. Krauss and S. Chou, "Sub-10 nm imprint lithography and applications", in *1997 55th Annu. Device Res. Conf. Dig.*, vol. 2897, IEEE, 1997, pp. 90–91, ISBN: 0-7803-3911-8,
DOI: 10.1109/DRC.1997.612486.

[17] L. J. Guo, "Nanoimprint lithography: Methods and material requirements", *Adv. Mater.*, vol. 19, no. 4, pp. 495–513, 2007, ISSN: 09359648,
DOI: 10.1002/adma.200600882.

[18] H. Schift, "Nanoimprint lithography: An old story in modern times? A review", *J. Vac. Sci. Technol. B Microelectron. Nanom. Struct.*, vol. 26, no. 2, p. 458, 2008, ISSN: 10711023,
DOI: 10.1116/1.2890972.

[19] M. C. Traub, W. Longsine, and V. N. Truskett, "Advances in Nanoimprint Lithography", *Annu. Rev. Chem. Biomol. Eng.*, vol. 7, no. 1, pp. 583–604, 2016, ISSN: 19475438,
DOI: 10.1146/annurev-chembioeng-080615-034635.

[20] L. M. Cox, A. M. Martinez, A. K. Blevins, N. Sowan, Y. Ding, and C. N. Bowman, "Nanoimprint lithography: Emergent materials and methods of actuation", *Nano Today*, vol. 31, p. 100 838, 2020, ISSN: 17480132,
DOI: 10.1016/j.nantod.2019.100838.

[21] R. Glass, M. M ller, and J. P. Spatz, "Block copolymer micelle nanolithography", *Nanotechnology*, vol. 14, no. 10, pp. 1153–1160, 2003, ISSN: 0957-4484,
DOI: 10.1088/0957-4484/14/10/314.

[22] D. Bera, S. C. Kuiry, and S. Seal, "Synthesis of Nanostructured Materials Using Template-Assisted Electrodeposition", *Jom*, vol. 56, no. 1, pp. 49–53, 2004, ISSN: 10474838,
DOI: 10.1007/s11837-004-0273-5.

[23] C. L. Haynes and R. P. Van Duyne, "Nanosphere Lithography: A Versatile Nanofabrication Tool for Studies of Size-Dependent Nanoparticle Optics", *J. Phys. Chem. B*, vol. 105, no. 24, pp. 5599–5611, 2001, ISSN: 1520-6106,
DOI: 10.1021/jp010657m.

[24] S. H. Ahn and L. J. Guo, "Large-area roll-to-roll and roll-to-plate nanoimprint lithography: a step toward high-throughput application of continuous nanoimprinting.", *ACS Nano*, vol. 3, no. 8, pp. 2304–10, 2009, ISSN: 1936-086X,
DOI: 10.1021/nn9003633.

[25] B. Heidari, I. Maximov, and L. Montelius, "Nanoimprint lithography at the 6 in. wafer scale", *J. Vac. Sci. Technol. B Microelectron. Nanom. Struct.*, vol. 18, no. 6, p. 3557, 2000, ISSN: 0734211X,
DOI: 10.1116/1.1326923.

[26] S. Y. Chou, P. R. Krauss, and P. J. Renstrom, "Imprint of sub-25 nm vias and trenches in polymers", *Appl. Phys. Lett.*, vol. 67, no. 21, pp. 3114–3116, 1995, ISSN: 0003-6951,
DOI: 10.1063/1.114851.

[27] B. D. Lucas, J.-S. Kim, C. Chin, and L. J. Guo, "Nanoimprint Lithography Based Approach for the Fabrication of Large-Area, Uniformly-Oriented Plasmonic Arrays", *Adv. Mater.*, vol. 20, no. 6, pp. 1129–1134, 2008, ISSN: 09359648,
DOI: 10.1002/adma.200700225.

[28] R. D. Nagel, S. Filser, T. Zhang, A. Manzi, K. Schönleber, J. Lindsly, J. Zimmermann, T. L. Maier, G. Scarpa, K. Krischer, and P. Lugli, "Nanoimprint methods for the fabrication of macroscopic plasmonically active metal nanostructures", *J. Appl. Phys.*, vol. 121, no. 8, p. 084 305, 2017, ISSN: 0021-8979,
DOI: 10.1063/1.4976860.

[29] S. Filser, T. L. Maier, R. D. Nagel, W. Schindler, P. Lugli, M. Becherer, and K. Krischer, "Photoelectrochemical reactivity of well-defined mesoscale gold arrays on SiO2/Si substrates in CO2-saturated aqueous electrolyte", *Electrochim. Acta*, vol. 268, pp. 546–553, 2018, ISSN: 0013-4686,
DOI: 10.1016/j.electacta.2018.02.018.

[30] T. L. Maier, M. Golibrzuch, S. Mendisch, W. Schindler, M. Becherer, and K. Krischer, "Lateral silicon oxide/gold interfaces enhance the rate of electrochemical hydrogen evolution reaction in alkaline media", *J. Chem. Phys.*, vol. 152, no. 15, p. 154 705, 2020, ISSN: 0021-9606,
DOI: 10.1063/5.0003295.

[31] M.-S. Kim, J.-S. Kim, J. C. Cho, M. Shtein, L. J. Guo, and J. Kim, "Flexible conjugated polymer photovoltaic cells with controlled heterojunctions fabricated using nanoimprint lithography", *Appl. Phys. Lett.*, vol. 90, no. 12, p. 123 113, 2007, ISSN: 0003-6951, DOI: 10.1063/1.2715036.

[32] M. G. Kang, M. S. Kim, J. Kim, and L. J. Guo, "Organic solar cells using nanoimprinted transparent metal electrodes", *Adv. Mater.*, vol. 20, no. 23, pp. 4408–4413, 2008, ISSN: 09359648, DOI: 10.1002/adma.200800750.

[33] R. D. Nagel, "Nanoimprint technologies for energy conversion applications", Dissertation, Technische Universität München, 2020, p. 180, URL: https://mediatum.ub.tum.de/604993?query=nanoimprint%7B%5C&%7Dshow%7B%5C_%7Did=1537772%7B%5C&%7Dsrcnodeid=604993.

[34] R. D. Nagel, T. Haeberle, M. Schmidt, P. Lugli, and G. Scarpa, "Large Area Nano-transfer Printing of Sub-50-nm Metal Nanostructures Using Low-cost Semi-flexible Hybrid Templates", *Nanoscale Res. Lett.*, vol. 11, no. 1, p. 143, 2016, ISSN: 1931-7573, DOI: 10.1186/s11671-016-1346-4.

[35] M. Colburn, S. C. Johnson, M. D. Stewart, S. Damle, T. C. Bailey, B. Choi, M. Wedlake, T. B. Michaelson, S. V. Sreenivasan, J. G. Ekerdt, and C. G. Willson, "Step and flash imprint lithography: a new approach to high-resolution patterning", *Emerg. Lithogr. Technol. III*, vol. 3676, no. March, p. 379, 1999, ISSN: 0277786X, DOI: 10.1117/12.351155.

[36] L. J. Guo, "Recent progress in nanoimprint technology and its applications", *J. Phys. D. Appl. Phys.*, vol. 37, no. 11, R123–R141, 2004, ISSN: 0022-3727, DOI: 10.1088/0022-3727/37/11/R01.

[37] Z. Yu, W. Wu, L. Chen, and S. Y. Chou, "Fabrication of large area 100 nm pitch grating by spatial frequency doubling and nanoimprint lithography for subwavelength optical applications", *J. Vac. Sci. Technol. B Microelectron. Nanom. Struct.*, vol. 19, no. 6, p. 2816, 2001, ISSN: 0734211X, DOI: 10.1116/1.1409384.

[38] Z. Yu and S. Y. Chou, "Triangular Profile Imprint Molds in Nanograting Fabrication", *Nano Lett.*, vol. 4, no. 2, pp. 341–344, 2004, ISSN: 15306984,
DOI: 10.1021/nl0349471.

[39] Y. Yao, Y. Wang, H. Liu, Y. Li, B. Song, and W. Wu, "Line width tuning and smoothening for periodical grating fabrication in nanoimprint lithography", *Appl. Phys. A Mater. Sci. Process.*, vol. 121, no. 2, pp. 399–403, 2015, ISSN: 14320630,
DOI: 10.1007/s00339-015-9278-x.

[40] H. J. Park, M. G. Kang, and L. J. Guo, "Large area high density sub-20 nm SiO2 nanostructures fabricated by block copolymer template for nanoimprint lithography", *ACS Nano*, vol. 3, no. 9, pp. 2601–2608, 2009, ISSN: 19360851,
DOI: 10.1021/nn900701p.

[41] S. Xiao, X. Yang, J. J. Hwu, K. Y. Lee, and D. Kuo, "A facile route to regular and nonregular dot arrays by integrating nanoimprint lithography with sphere-forming block copolymer directed self-assembly", *J. Polym. Sci. Part B Polym. Phys.*, vol. 52, no. 5, pp. 361–367, 2014, ISSN: 10990488,
DOI: 10.1002/polb.23433.

[42] M. Mühlberger, I. Bergmair, A. Klukowska, A. Kolander, H. Leichtfried, E. Platzgummer, H. Loeschner, C. Ebm, G. Grützner, and R. Schöftner, "UV-NIL with working stamps made from Ormostamp", *Microelectron. Eng.*, vol. 86, no. 4-6, pp. 691–693, 2009, ISSN: 0167-9317,
DOI: 10.1016/j.mee.2008.11.020.

[43] Miroresist Technology, "Processing Guidelines OrmoStamp", MicroResist Technology, Tech. Rep., 2012, pp. 1–6,
URL: https://wiki.nanotech.ucsb.edu/w/images/1/19/OrmoStamp-NIL-Lithography-UV-Soft-RevA.pdf.

[44] M. Tyona, "A theoritical study on spin coating technique", *Adv. Mater. Res.*, vol. 2, no. 4, pp. 195–208, 2013, ISSN: 2234-0912,
DOI: 10.12989/amr.2013.2.4.195.

[45] D. E. Bornside, C. W. Macosko, and L. E. Scriven, "Spin coating: One-dimensional model", *J. Appl. Phys.*, vol. 66, no. 11, pp. 5185–5193, 1989, ISSN: 00218979,
DOI: 10.1063/1.343754.

[46] D. B. Hall, P. Underhill, and J. M. Torkelson, "Spin coating of thin and ultrathin polymer films", *Polym. Eng. Sci.*, vol. 38, no. 12, pp. 2039–2045, 1998, ISSN: 0032-3888,
DOI: 10.1002/pen.10373.

[47] H. Schift and A. Kristensen, "Nanoimprint Lithography – Patterning of Resists Using Molding", in *Springer Handb. Nanotechnol.* B. Bhushan, Ed., 3rd, Berlin, Heidelberg: Springer Berlin Heidelberg, 2010, pp. 271–312, ISBN: 978-3-642-02525-9,
DOI: 10.1007/978-3-642-02525-9_9.

[48] G. Łukaszewicz and P. Kalita, *Navier–Stokes Equations* (Advances in Mechanics and Mathematics). Cham: Springer International Publishing, 2016, ISBN: 978-3-319-27758-5,
DOI: 10.1007/978-3-319-27760-8.

[49] M. Stefan, "Parallel Platten Rheometer", *Akad. Wiss. Math.-Naturwiss. Vienna*, vol. 2, no. 69, pp. 713–735, 1874.

[50] A. U. Alam, M. M. R. Howlader, and M. J. Deen, "Oxygen Plasma and Humidity Dependent Surface Analysis of Silicon, Silicon Dioxide and Glass for Direct Wafer Bonding", *ECS J. Solid State Sci. Technol.*, vol. 2, no. 12, P515–P523, 2013, ISSN: 2162-8769,
DOI: 10.1149/2.007312jss.

[51] S. Kaya, P. Rajan, H. Dasari, D. C. Ingram, W. Jadwisienczak, and F. Rahman, "A Systematic Study of Plasma Activation of Silicon Surfaces for Self Assembly", *ACS Appl. Mater. Interfaces*, vol. 7, no. 45, pp. 25 024–25 031, 2015, ISSN: 19448252,
DOI: 10.1021/acsami.5b08358.

[52] P. Verdonck, P. B. Calíope, E. D. M. Hernandez, and A. N. R. da Silva, "Plasma etching of electrospun polymeric nanofibres", *Thin Solid Films*, vol. 515, no. 2 SPEC. ISS. Pp. 831–834, 2006, ISSN: 00406090,
DOI: 10.1016/j.tsf.2005.12.196.

[53] F. Karouta, "A practical approach to reactive ion etching", *J. Phys. D. Appl. Phys.*, vol. 47, no. 23, p. 233 501, 2014, ISSN: 0022-3727, DOI: 10.1088/0022-3727/47/23/233501.

[54] F. Laermer, A. Schilp, and Robert Bosch GmbH, *Method of anisotropically etching silicon*, 1993, URL: https://patents.google.com/patent/US5501893A/en.

[55] M. Golibrzuch, T. L. Maier, M. J. Feil, K. Krischer, and M. Becherer, "Tuning the feature size of nanoimprinting stamps: A method to enhance the flexibility of nanoimprint lithography", *J. Appl. Phys.*, vol. 131, no. 12, 2022, ISSN: 10897550, DOI: 10.1063/5.0079282.

[56] Y. J. Chabal, G. S. Higashi, K. Raghavachari, and V. A. Burrows, "Infrared spectroscopy of Si(111) and Si(100) surfaces after HF treatment: Hydrogen termination and surface morphology", *J. Vac. Sci. Technol. A Vacuum, Surfaces, Film.*, vol. 7, no. 3, pp. 2104–2109, 1989, ISSN: 0734-2101, DOI: 10.1116/1.575980.

[57] T. L. Maier, "Enhancing the Hydrogen Evolution Reaction on Nanostructured Metal-Silicon Electrodes by a Bifunctional Mechanism", Dissertation, Technische Universität München, 2023.

[58] K. Krischer and E. R. Savinova, "Fundamentals of Electrocatalysis", in *Handb. Heterog. Catal.* Vol. 3-5, Weinheim, Germany: Wiley-VCH Verlag GmbH & Co. KGaA, 2008, pp. 1873–1905, ISBN: 3-527-29212-8, DOI: 10.1002/9783527610044.hetcat0101.

[59] S. Trasatti, "The concept of absolute electrode potential an attempt at a calculation", *J. Electroanal. Chem.*, vol. 52, no. 3, pp. 313–329, 1974, ISSN: 00220728, DOI: 10.1016/S0022-0728(74)80446-8.

[60] A. J. Bard and L. R. Faulkner, *Electrochemical methods. Fundamentals and applications*. Wiley, 2000, ISBN: 978-0-471-04372-0, URL: https://www.wiley.com/en-kr/Electrochemical+Methods:+Fundamentals+and+Applications,+2nd+Edition-p-9780471043720.

[61] C. H. Hamann, A. Hamnett, and W. Vielstich, *Electrochemistry*. Wiley-VCH, 2007, ISBN: 978-3-527-31069-2,
URL: https://www.wiley-vch.de/de/fachgebiete/naturwissenschaften/electrochemistry-978-3-527-31069-2.

[62] W. Vielstich, A. Lamm, and H. A. Gasteiger, *Handbook of Fuel Cells: Fundamentals, Technology, Applications, 4 Volume Set*. Wiley, 2003, ISBN: 978-0-471-49926-8,
URL: https://www.wiley.com/en-us/Handbook+of+Fuel+Cells%7B%5C%%7D3A+Fundamentals%7B%5C%%7D2C+Technology%7B%5C%%7D2C+Applications%7B%5C%%7D2C+4+Volume+Set-p-9780471499268.

[63] J. O. Bockris, A. K. Reddy, and M. Gamboa-Aldeco, *Modern Electrochemistry 2A*. Boston, MA: Springer US, 2002, pp. 771–1534, ISBN: 0-306-46166-8,
DOI: 10.1007/b113922.

[64] J. Tafel, "Über die Polarisation bei kathodischer Wasserstoffentwicklung", *Zeitschrift für Phys. Chemie*, vol. 50U, no. 1, pp. 641–712, 1905, ISSN: 2196-7156,
DOI: 10.1515/zpch-1905-5043.

[65] S. Trasatti, "Work function, electronegativity, and electrochemical behaviour of metals. III. Electrolytic hydrogen evolution in acid solutions", *J. Electroanal. Chem.*, vol. 39, no. 1, pp. 163–184, 1972, ISSN: 00220728,
DOI: 10.1016/S0022-0728(72)80485-6.

[66] B. Hammer and J. K. Norskov, *Why gold is the noblest of all the metals*, 1995,
DOI: 10.1038/376238a0.

[67] E. Santos, A. Lundin, K. Pötting, P. Quaino, and W. Schmickler, "Model for the electrocatalysis of hydrogen evolution", *Phys. Rev. B - Condens. Matter Mater. Phys.*, vol. 79, no. 23, pp. 1–10, 2009, ISSN: 10980121,
DOI: 10.1103/PhysRevB.79.235436.

[68] P. Quaino, F. Juarez, E. Santos, and W. Schmickler, "Volcano plots in hydrogen electrocatalysis-uses and abuses", *Beilstein J. Nanotechnol.*, vol. 5, no. 1, pp. 846–854, 2014, ISSN: 21904286, DOI: 10.3762/bjnano.5.96.

[69] T. Ohmori and M. Enyo, "Hydrogen evolution reaction on gold electrode in alkaline solutions", *Electrochim. Acta*, vol. 37, no. 11, pp. 2021–2028, 1992, ISSN: 00134686, DOI: 10.1016/0013-4686(92)87118-J.

[70] A. Goyal and M. T. Koper, "The Interrelated Effect of Cations and Electrolyte pH on the Hydrogen Evolution Reaction on Gold Electrodes in Alkaline Media", *Angew. Chemie - Int. Ed.*, vol. 60, no. 24, pp. 13 452–13 462, 2021, ISSN: 15213773, DOI: 10.1002/anie.202102803.

[71] P. J. Rheinländer, J. Herranz, J. Durst, and H. A. Gasteiger, "Kinetics of the Hydrogen Oxidation/Evolution Reaction on Polycrystalline Platinum in Alkaline Electrolyte Reaction Order with Respect to Hydrogen Pressure", *J. Electrochem. Soc.*, vol. 161, no. 14, F1448–F1457, 2014, ISSN: 0013-4651, DOI: 10.1149/2.0501414jes.

[72] I. Ledezma-Yanez, W. D. Z. Wallace, P. Sebastián-Pascual, V. Climent, J. M. Feliu, and M. T. Koper, "Interfacial water reorganization as a pH-dependent descriptor of the hydrogen evolution rate on platinum electrodes", *Nat. Energy*, vol. 2, no. 4, pp. 1–7, 2017, ISSN: 20587546, DOI: 10.1038/nenergy.2017.31.

[73] Y. Zheng, Y. Jiao, A. Vasileff, and S. Z. Qiao, "The Hydrogen Evolution Reaction in Alkaline Solution: From Theory, Single Crystal Models, to Practical Electrocatalysts", *Angew. Chemie - Int. Ed.*, vol. 57, no. 26, pp. 7568–7579, 2018, ISSN: 15213773, DOI: 10.1002/anie.201710556.

[74] R. Subbaraman, D. Tripkovic, D. Strmcnik, K. C. Chang, M. Uchimura, A. P. Paulikas, V. Stamenkovic, and N. M. Markovic, "Enhancing hydrogen evolution activity in water splitting by tailoring Li+-Ni(OH)2-Pt interfaces", *Science (80-.).*, vol. 334, no. 6060,

pp. 1256–1260, 2011, ISSN: 10959203,
DOI: 10.1126/science.1211934.

[75] S. Xue, B. Garlyyev, S. Watzele, Y. Liang, J. Fichtner, M. D. Pohl, and A. S. Bandarenka, "Influence of Alkali Metal Cations on the Hydrogen Evolution Reaction Activity of Pt, Ir, Au, and Ag Electrodes in Alkaline Electrolytes", *ChemElectroChem*, vol. 5, no. 17, pp. 2326–2329, 2018, ISSN: 21960216,
DOI: 10.1002/celc.201800690.

[76] H. Kirsch, *Semiconductor Photocatalysis*, H. Kisch, Ed. Weinheim, Germany: Wiley-VCH, 2014, ISBN: 9783527673315,
DOI: 10.1002/9783527673315.

[77] L. Hüttenhofer, M. Golibrzuch, O. Bienek, F. J. Wendisch, R. Lin, M. Becherer, I. D. Sharp, S. A. Maier, and E. Cortés, "Metasurface Photoelectrodes for Enhanced Solar Fuel Generation", *Adv. Energy Mater.*, vol. 11, no. 46, 2021, ISSN: 16146840,
DOI: 10.1002/aenm.202102877.

[78] L. Hüttenhofer, "Enhanced Solar Energy Harvesting by Metasurface Photoelectrodes", Dissertation, Ludwig Maximilian Universität München, 2022,
URL: https://edoc.ub.uni-muenchen.de/29331/1/Huettenhofer%7B%5C_%7DLudwig.pdf.

[79] M. G. Walter, E. L. Warren, J. R. McKone, S. W. Boettcher, Q. Mi, E. A. Santori, and N. S. Lewis, "Solar water splitting cells", *Chem. Rev.*, vol. 110, no. 11, pp. 6446–6473, 2010, ISSN: 00092665,
DOI: 10.1021/cr1002326.

[80] A. Tittl, M. G. Harats, R. Walter, X. Yin, M. Schäferling, N. Liu, R. Rapaport, and H. Giessen, "Quantitative angle-resolved small-spot reflectance measurements on plasmonic perfect absorbers: Impedance matching and disorder effects", *ACS Nano*, vol. 8, no. 10, pp. 10 885–10 892, 2014, ISSN: 1936086X,
DOI: 10.1021/nn504708t.

[81] A. E. Miroshnichenko, A. B. Evlyukhin, Y. F. Yu, R. M. Bakker, A. Chipouline, A. I. Kuznetsov, B. Luk'yanchuk, B. N. Chichkov, and Y. S. Kivshar, "Nonradiating anapole modes in dielectric nanoparti-

cles", *Nat. Commun.*, vol. 6, no. 1, p. 8069, 2015, ISSN: 2041-1723, DOI: 10.1038/ncomms9069.

[82] G. Mie, "Beiträge zur Optik trüber Medien, speziell kolloidaler Metallösungen", *Ann. Phys.*, vol. 330, no. 3, pp. 377–445, 1908, ISSN: 00033804, DOI: 10.1002/andp.19083300302.

[83] C. F. Bohren and D. R. Huffman, *Absorption and Scattering of Light by Small Particles*. Wiley, 1983, ISBN: 9780471293408, DOI: 10.1002/9783527618156.

[84] S. Hu, M. R. Shaner, J. A. Beardslee, M. Lichterman, B. S. Brunschwig, and N. S. Lewis, "Amorphous TiO2 coatings stabilize Si, GaAs, and GaP photoanodes for efficient water oxidation", *Science (80-.).*, vol. 344, no. 6187, pp. 1005–1009, 2014, ISSN: 10959203, DOI: 10.1126/science.1251428.

[85] F. Opoku, K. K. Govender, C. G. C. E. van Sittert, and P. P. Govender, "Recent Progress in the Development of Semiconductor-Based Photocatalyst Materials for Applications in Photocatalytic Water Splitting and Degradation of Pollutants", *Adv. Sustain. Syst.*, vol. 1, no. 7, pp. 1–24, 2017, ISSN: 23667486, DOI: 10.1002/adsu.201700006.

[86] C. Gao, Z. C. Xu, S. R. Deng, J. Wan, Y. Chen, R. Liu, E. Huq, and X. P. Qu, "Silicon nanowires by combined nanoimprint and angle deposition for gas sensing applications", *Microelectron. Eng.*, vol. 88, no. 8, pp. 2100–2104, 2011, ISSN: 01679317, DOI: 10.1016/j.mee.2011.02.044.

[87] C. Pina-Hernandez, P. F. Fu, and L. J. Guo, "Ultrasmall structure fabrication via a facile size modification of nanoimprinted functional silsesquioxane features", *ACS Nano*, vol. 5, no. 2, pp. 923–931, 2011, ISSN: 19360851, DOI: 10.1021/nn102127z.

[88] Q. Xia and S. Y. Chou, "Fabrication of sub-25 nm diameter pillar nanoimprint molds with smooth sidewalls using self-perfection by liquefaction and reactive ion etching", *Nanotechnology*, vol. 19, no. 45, pp. 4–7, 2008, ISSN: 09574484, DOI: 10.1088/0957-4484/19/45/455301.

[89] C. Wang, Q. Zhang, Y. Song, and S. Y. Chou, "Plasmonic bar-coupled dots-on-pillar cavity antenna with dual resonances for infrared absorption and sensing: Performance and nanoimprint fabrication", *ACS Nano*, vol. 8, no. 3, pp. 2618–2624, 2014, ISSN: 1936086X, DOI: 10.1021/nn406281u.

[90] K. S. Lee and M. A. El-Sayed, "Gold and silver nanoparticles in sensing and imaging: Sensitivity of plasmon response to size, shape, and metal composition", *J. Phys. Chem. B*, vol. 110, no. 39, pp. 19 220–19 225, 2006, ISSN: 15206106, DOI: 10.1021/jp062536y.

[91] I. Zorić, M. Zäch, B. Kasemo, and C. Langhammer, "Gold, Platinum, and Aluminum Nanodisk Plasmons: Material Independence, Subradiance, and Damping Mechanisms", *ACS Nano*, vol. 5, no. 4, pp. 2535–2546, 2011, ISSN: 1936-0851, DOI: 10.1021/nn102166t.

[92] S. A. Maier, *Plasmonics: Fundamentals and Applications*. New York, NY: Springer US, 2007, ISBN: 978-0-387-33150-8, DOI: 10.1007/0-387-37825-1.

[93] P. Drude, "Zur Elektronentheorie der Metalle", *Ann. Phys.*, vol. 306, no. 3, pp. 566–613, 1900, ISSN: 00033804, DOI: 10.1002/andp.19003060312.

[94] C. Kittel, *Introduction to Solid State Physics*. New York: Wiley, 2004, ISBN: 978-0-471-41526-8, URL: https://www.wiley.com/en-us/Introduction+to+Solid+State+Physics%7B%5C%%7D2C+8th+Edition-p-9780471415268.

[95] P. B. Johnson and R. W. Christy, "Optical Constants of the Noble Metals", *Phys. Rev. B*, vol. 6, no. 12, pp. 4370–4379, 1972, ISSN: 0556-2805, DOI: 10.1103/PhysRevB.6.4370.

[96] U. Kreibig and M. Vollmer, *Optical Properties of Metal Clusters* (Springer Series in Materials Science). Berlin, Heidelberg: Springer Berlin Heidelberg, 1995, vol. 25, ISBN: 978-3-642-08191-0, DOI: 10.1007/978-3-662-09109-8.

[97] M. Meier and A. Wokaun, "Enhanced fields on large metal particles: dynamic depolarization", *Opt. Lett.*, vol. 8, no. 11, p. 581, 1983, ISSN: 0146-9592,
DOI: 10.1364/OL.8.000581.

[98] A. Wokaun, J. P. Gordon, and P. F. Liao, "Radiation damping in surface-enhanced Raman scattering", *Phys. Rev. Lett.*, vol. 48, no. 14, pp. 957–960, 1982, ISSN: 00319007,
DOI: 10.1103/PhysRevLett.48.957.

[99] S. A. Maier, M. L. Brongersma, P. G. Kik, and H. A. Atwater, "Observation of near-field coupling in metal nanoparticle chains using far-field polarization spectroscopy", *Phys. Rev. B - Condens. Matter Mater. Phys.*, vol. 65, no. 19, pp. 1–4, 2002, ISSN: 1550235X,
DOI: 10.1103/PhysRevB.65.193408.

[100] P. R. Emtage, "Interaction of magnetostatic waves with a current", *J. Appl. Phys.*, vol. 49, no. 8, pp. 4475–4484, 1978, ISSN: 00218979,
DOI: 10.1063/1.325452.

[101] V. Vlaminck and M. Bailleul, "Spin-wave transduction at the submicrometer scale: Experiment and modeling", *Phys. Rev. B - Condens. Matter Mater. Phys.*, vol. 81, no. 1, pp. 1–13, 2010, ISSN: 10980121,
DOI: 10.1103/PhysRevB.81.014425.

[102] J. Greil, M. Golibrzuch, M. Kiechle, Á. Papp, V. Ahrens, G. Csaba, and M. Becherer, "Secondary Excitation of Spin-Waves: How Electromagnetic Cross-Talk Impacts on Magnonic Devices", *arXiv*, 2023,
DOI: 10.48550/arXiv.2303.11303.

[103] R. Leuschner and G. Pawlowski, "Photolithography", in *Handb. Semicond. Technol.* Weinheim, Germany: Wiley-VCH Verlag GmbH, 2000, pp. 177–263,
DOI: 10.1002/9783527621828.ch4.

[104] Á. Papp, W. Porod, and G. Csaba, "Nanoscale neural network using non-linear spin-wave interference", *Nat. Commun.*, vol. 12, no. 1, p. 6422, 2021, ISSN: 2041-1723,
DOI: 10.1038/s41467-021-26711-z.

[105] A. Mahmoud, F. Ciubotaru, F. Vanderveken, A. V. Chumak, S. Hamdioui, C. Adelmann, and S. Cotofana, "Introduction to spin wave computing", *J. Appl. Phys.*, vol. 128, no. 16, p. 161 101, 2020, ISSN: 0021-8979,
DOI: 10.1063/5.0019328.

[106] F. Brailsford, *Physical principles of magnetism*. London; New York: Van Nostrand, 1966,
URL: https://openlibrary.org/works/OL7285285W/Physical%7B%5C_%7Dprinciples%7B%5C_%7Dof%7B%5C_%7Dmagnetism.

[107] L. Landau and E. Lifshitz, "On the theory of the dispersion of magnetic permeability in ferromagnetic bodies", *Phys. Zeitschrift der Sowjetunion*, vol. 2, no. Part 2, p. 153, 1935,
DOI: 10.1016/B978-0-08-036364-6.50008-9.

[108] T. Gilbert, "Classics in Magnetics A Phenomenological Theory of Damping in Ferromagnetic Materials", *IEEE Trans. Magn.*, vol. 40, no. 6, pp. 3443–3449, 2004, ISSN: 0018-9464,
DOI: 10.1109/TMAG.2004.836740.

[109] J. Greil, "Modeling and Evaluation of Transducer Designs for Electrical Spin Wave Spectroscopy", Master thesis, Technische Universität München, 2022.

[110] D. D. Stancil and A. Prabhaker, *Spin Waves*. Boston, MA: Springer US, 2009, ISBN: 978-0-387-77864-8,
DOI: 10.1007/978-0-387-77865-5.

[111] A. Gurevich and G. Melkov, *Magnetization Oscillations and Waves*. London: CRC Press, 1996, ISBN: 9780138748487,
DOI: 10.1201/9780138748487.

[112] S. Chikazumi, *Physics of Ferromagnetism*. Oxford, New York: Oxford University Press, 1997, ISBN: 9780199564811,
URL: https://global.oup.com/academic/product/physics-of-ferromagnetism-2e-9780199564811?cc=de%7B%5C&%7Dlang=en%7B%5C&%7D.

[113] B. A. Kalinikos and A. N. Slavin, "Theory of dipole-exchange spin wave spectrum for ferromagnetic films with mixed exchange boundary conditions", *J. Phys. C Solid State Phys.*, vol. 19, no. 35, pp. 7013–7033, 1986, ISSN: 0022-3719,
DOI: 10.1088/0022-3719/19/35/014.

[114] P. M. A. Pirro, "Lineare und nichtlineare Spinwelleninteraktionen in magnetischen Mikrostrukturen", Dissertation, Technische Universität Kaiserslautern, 2014,
URL: https://d-nb.info/1063292980/04.

[115] M. T. Johnson, P. J. Bloemen, F. J. Den Broeder, and J. J. De Vries, "Magnetic anisotropy in metallic multilayers", *Reports Prog. Phys.*, vol. 59, no. 11, pp. 1409–1458, 1996, ISSN: 00344885,
DOI: 10.1088/0034-4885/59/11/002.

[116] M. Kiechle, A. Papp, S. Mendisch, V. Ahrens, M. Golibrzuch, G. H. Bernstein, W. Porod, G. Csaba, and M. Becherer, "Spin-Wave Optics in YIG Realized by Ion-Beam Irradiation", *Small*, p. 2 207 293, 2023, ISSN: 1613-6810,
DOI: 10.1002/smll.202207293.

[117] M. Kiechle, L. Maucha, V. Ahrens, C. Dubs, W. Porod, G. Csaba, M. Becherer, and A. Papp, "Experimental Demonstration of a Spin-Wave Lens Designed With Machine Learning", *IEEE Magn. Lett.*, vol. 13, pp. 1–5, 2022, ISSN: 1949-307X,
DOI: 10.1109/LMAG.2022.3209647.

[118] M. Mansuripur, "The magneto-optical Kerr effect", in *Class. Opt. its Appl.* Cambridge University Press, 2009, pp. 166–181,
DOI: 10.1017/CBO9780511803796.016.

[119] A. Vansteenkiste, J. Leliaert, M. Dvornik, M. Helsen, F. Garcia-Sanchez, and B. Van Waeyenberge, "The design and verification of MuMax3", *AIP Adv.*, vol. 4, no. 10, p. 107 133, 2014, ISSN: 2158-3226,
DOI: 10.1063/1.4899186.

[120] S. Mendisch, "Perpendicular Nanomagnets: The Building Blocks of Field-Coupled Logic Devices", Dissertation, Technische Universität München, 2022, p. 172,

URL: https://mediatum.ub.tum.de/604993?query=mendisch%7B%5C&%7Dshow%7B%5C_%7Did=1655090%7B%5C&%7Dsrcnodeid=604993.

Acknowledgments

Dear reader, thank you for your interest in my work. This work would not have been possible without the support of many people. Therefore, it is now time to say thank you.

Foremost, I want to thank PD Markus Becherer for the opportunity to do my doctorate in his group. Thank you for all the support and trust you put into my work at the Garching outpost and the freedom you gave me to roam around and spread the technology to new cooperation partners. Although the topic was not always related to the magnetic core business of the group, I always felt well-advised, appreciated, and part of the team.

Next, I would like to thank the whole Nanomagnetic Devices group. Special thanks to Josef Mock, the second part of the Garching outpost, who kept the Garching labs up and running and was always there for professional and emotional support. Furthermore, thank you to the magnetic people of the group, Simon Mendisch, Martina Kiechle, Valentin Ahrens, and Johannes Greil. Magnetics was never my favorite research topic in the world. Still, it became almost fascinating with such fantastic colleagues, and I had the opportunity to contribute to excellent research in the field. I enjoyed the discussions about work and life with all of you, opening up new perspectives inside and outside of work. Moreover, I want to thank Robin Nagel, my predecessor regarding nanoimprinting, who always had advice when needed.

Special thanks to the ZEITlab staff Rosemarie Mittermeier, Annika Kwiat-kowski, and Rainer Emling, for the help, assistance, and guidance regarding all safety, processing, and equipment issues in the lab. I always could count on you, making life so much easier. Also, thank you, Susanne Maier, for taking care of most of the administrative overhead and allowing me to focus on my research.

Every fabrication technology is not worth a lot without an application that uses it. Therefore, I want to thank all my cooperation partners who accompanied my journey over the last few years.

Thank you to Prof. Katharina Krischer's group for the close and successful cooperation within our IGSSE project at TUM. Special thanks are due to Thomas Maier, who was my partner in crime for almost five years regarding the electrochemical applications of NIL. We formed a formidable tandem and pushed the field forward together. Additionally, I want to thank Prof. Katharina Krischer, Simon Filser, Moritz Feil, and Tina Angerer for the close collaboration, the fruitful discussions, and the opportunity to impact your work.

Furthermore, I want to thank Ludwig Hüttenhofer from LMU for the excellent cooperation on semiconductor metasurfaces and their application for solar light harvesting. I really enjoyed the uncomplicated collaboration and the fantastic results.

I was lucky I had the opportunity to go on a research exchange to Canada for three months. Thank you, Prof. Frank Hegmann, Howe Simpson, and the whole Hegmann group, for making the three months such an amazing experience inside and outside the lab. I will miss the incredible THz STM and the karaoke nights.

Ultimately, every experimentalist's success depends on the facilities and equipment at hand. Besides the ZEITlab, I had the great pleasure of working in the ZNN at TUM, where most of the work for my doctorate was done. Therefore, I want to thank Prof. Alexander Holleitner for generously providing space and equipment in the ZNNs facilities for my work. Special thanks to Peter Weiser and Claudia Paulus for keeping watch over the ZNN clean room and enabling excellent research. I also want to thank all the technicians and fellow doctoral candidates who keep all the machines and equipment up and running. I could not have done it without you.

Last, I want to thank my family and friends for all their support and interest over the last few years. Also, thank you for listening to the numerous outrages about machines and equipment not working and the often lengthy attempts to describe my work in simple terms.